PROPOSAL FOR THE AEGIS EXPERIMENT AT THE CERN ANTIPROTON DECELERATOR

(**A**ntimatter **E**xperiment: **G**ravity, **I**nterferometry, **S**pectroscopy)

June 8, 2007

G. Drobychev, P. Nedelec, D. Sillou
LAPP - 9 Chemin De Bellevue BP110 F-74941 Annecy, CEDEX France

G. Gribakin, H. Walters
Queen's University, University Road, Belfast, United kingdom

G. Ferrari, M. Prevedelli, G.M. Tino
Istituto Nazionale di Fisica Nucleare, Department of Physics and LENS Via Sansone 1, 50019 Firenze, Italy

M. Doser
PH Department, CERN, CH-1211 Geneva 23, Switzerland

C. Canali, C. Carraro, V. Lagomarsino, G. Manuzio, G. Testera, S. Zavatarelli
Istituto Nazionale di Fisica Nucleare and Department of Physics Via Dodecanneso 33, 1646 Genova, Italy

M. Amoretti, A. Kellerbauer, J. Meier, U. Warring
Max Planck Institute for Nuclear Physics, P.O. Box 103980, 69029 Heidelberg, Germany

M. K. Oberthaler
Kirchhoff Institute of Physics, University of Heidelberg, Im Neuenheimer Feld 227, 69120 Heidelberg, Germany

I. Boscolo, F. Castelli, S. Cialdi, L. Formaro, A. Gervasini, G. Giammarchi, A. Vairo
Istituto Nazionale di Fisica Nucleare and Department of Physics Via Celoria, Milano Italy

G. Consolati, A. Dupasquier, F. Quasso
Politecnico di Milano, P. L. Da Vinci 32, Milano Italy

H. H. Stroke
New York University (Department of Physics), New York, USA

A.S. Belov, S.N. Gninenko, V.A. Matveev
Institute for Nuclear Research of the Russian Academy of Sciences, Moscow 117312, Russia

V.M. Byakov, S.V. Stepanov, D.S. Zvezhinskij
Institute for Theoretical and Experimental Physics (ITEP), Moscow 117218, Russia.

M. de Combarieu, P. Forget, P. Pari
Laboratoire de basse temprature du SPEC/DRECAM/DSM, CEA Saclay, France

L. Cabaret, D. Comparat
Laboratoire Aimé Cotton, CNRS II Campus d'Orsay, 91405 Orsay Cedex, France

G. Bonomi, A. Rotondi
Istituto Nazionale di Fisica Nucleare, Department of Physics, Via Bassi 6, 27100 Pavia, Italy

N. Djourelov
Institute for Nuclear Research and Nuclear Energy BAS, 72 Tzarigradsko Shoosse, 1784 Sofia, Bulgaria

M. Jacquey, M. Büchner, G. Trénec, J. Vigué

Laboratoire Collisions Agrégats Réactivité-IRSAMC Université Paul Sabatier and CNRS UMR 5589
118, Route de Narbonne; 31062 Toulouse Cedex, France

R. S. Brusa, S. Mariazzi
University of Trento and Department of Physics, Via Sommarive 14 Povo, Trento, Italy

S. Hogan, F. Merkt
Laboratorium für Physikalische Chemie, ETH Zürich, Switzerland

The following group has expressed interest in this experiment:

A. Badertscher, P. Crivelli, U. Gendotti, A. Rubbia
Institute For Particle Physics, Schafmattstr. 20 ETH Honggerberg Zürich

Contents

Chapter 1

Introduction

The primary scientific goal of the AEGIS experiment is the direct measurement of the Earth's gravitational acceleration g on antihydrogen. In the first phase of the experiment, a gravity measurement with 1% precision will be carried out by sending an antihydrogen beam through a classical Moiré deflectometer coupled to a position sensitive detector. In spite of the modest precision, this result is scientifically relevant, as it represents the first direct measurement of a gravitational effect on an antimatter system. Additional physics results concerning Rydberg spectroscopy can be obtained with the proposed AEGIS apparatus.

In a second phase of the experiment higher precision gravity measurements will become feasible. CPT spectroscopy is also of great interest for AEGIS and it is included in the long term scientific goal, even if the design of the apparatus and the technical choices are focused on the gravity measurement.

The AEGIS collaboration is asking for approval and beam time at the AD to perform the 1% gravity measurement. This approval will allow us to obtain a fundamental physics result with antihydrogen at the AD and the realization and in-situ commissioning of the core of the AEGIS apparatus. This core will be then completed with the equipment necessary for higher precision gravity measurements and spectroscopy in a second phase. Approval and beam time for this second phase of the experiment will be requested at the appropriate time.

The essential steps leading to the production of antihydrogen and the measurement of its gravitational interaction in AEGIS are the following:

- The production of antihydrogen is based on the charge exchange reaction between Rydberg positronium and cold antiprotons.
- We take advantage of the sensitivity of the Rydberg atoms to electric field gradients to form a beam of antihydrogen: an appropriate electric field is applied to sectors of the trap electrodes (Stark accelerator) immediately after the formation process to give a velocity boost of the order of a few hundred m/s in the horizontal direction to the antihydrogen atoms.
- The Moiré deflectometer is mounted downstream of the bore of the magnet and outside of the magnetic field. The beam is directed towards the gratings of the Moiré deflectometer for the gravity measurement. The vertical position and the arrival time of each antihydrogen atom are measured.

In order to carry out the proposed measurement, the following steps are required:

- Antiprotons delivered by the AD are trapped in a Malmberg-Penning trap mounted in a cryostat inside the bore of a 3 Tesla magnetic field and cooled by electron cooling down to sub eV energies. The antiprotons are then transferred into a second trap inside a lower magnetic field where they are cooled to 100 mK.
- A bunch (with a duration of tens of ns and few mm size) of more than about 10^8 positrons, accumulated in a Surko-type device in about 200 sec, is transferred from the accumulator into a trap mounted inside the same magnetic field as the antiproton trap. Here the bunch, compressed

in space and time with standard non-neutral plasma techniques, is sent on an appropriate porous target material where positronium in the fundamental state is produced with high efficiency.

- The positronium cloud emerging from the target is excited by two laser pulses into a specific Rydberg state (with quantum number n between 20 and 30).
- The trap containing the cold antiproton cloud is mounted very close to the positronium production target. Cold (100 mK) antihydrogen atoms with a predictable population of excited states are produced during the time in which the positronium traverses the antiproton cloud. While the preparation of the antiprotons and positronium cloud requires a few hundreds of seconds, the production of the antihydrogen atoms in AEGIS will be pulsed and it will happen within a short, experimentally known, time interval less than $\simeq 1$ μsec.
- Antiprotons that have not recombined can be quickly transfered back toward the catching region before applying the Stark accelerating electric field.
- The Rydberg atoms should decay toward the fundamental state (or the 2S state) during their flight from the end of the Stark accelerator to the first Moiré deflectometer grating. If needed, the decay rate can be accelerated by appropriate laser fields.
- Radial cooling of the beam can be implemented using quasi-CW Lyman-α laser at the exit of the magnet.

The AEGIS design is based on the experience of the ATHENA and ATRAP experiments at the AD, on a series of tests and developments performed by AEGIS members on matter systems and on simulations of several critical processes (charge exchange production of antihydrogen, antihydrogen acceleration process and propagation through the Moiré deflectometer, resolution of the position sensitive detector located at the end of the Moiré deflectometer). The proposed gravity measurement with the Moiré deflectometer is made feasible by merging in a single experimental apparatus technologies already demonstrated and including some reasonable additional development. Magnetic trapping of the antiatoms is not necessary to perform the gravity measurement in the first phase of the experiment.

As will be shown in this document, the precision of the gravity measurement is mainly limited by the antihydrogen temperature: obtaining samples of antiatoms far colder than 100 mK is essential to perform both much higher precision gravity measurements than in the first stage as well as competitive CPT tests through spectroscopy. Overcoming the experimental difficulties in reaching these ambitious goals will still require a number of experimental developments. The AEGIS collaboration is actively involved in this research and development with already funded projects, which will be described in the following sections.

The design of the AEGIS apparatus is modular and it allows, in a future second stage, the insertion of a magnetic trap for antihydrogen which will be spatially separated from the Malmberg-Penning trap where the antihydrogen atoms are produced. This spatial separation between the two traps differs significantly from the approach chosen by the experiments AD2 [2] and AD5 [3], which plan to trap antihydrogen atoms in the production region, requiring a trap that simultaneously combines the trapping properties of charged and neutral particles. The experience that will be gained in the first phase of AEGIS with the formation of the antihydrogen beam will be used to optimize the design of the antihydrogen trapping system. In this second phase, we intend to transport the antihydrogen atoms in the form of a beam from the production trap toward the magnetic trapping region, and to decellerate them once they have entered the trap region, through the use of Stark forces on Rydberg states to manipulate their velocity. Trapped antihydrogen can be cooled by laser cooling down to a temperature of about $\simeq mK$. Lower temperatures are needed for very high precision gravity measurements and the way to reach them is under study; CPT tests with a sensitivity competitive with current limits on CPT violations are however already feasible with trapped antihydrogen at $\simeq mK$.

Chapter 2

Physics motivation

2.1 Antihydrogen and the equivalence principle

It is widely expected that the gravitational interaction of matter and of antimatter should be identical, and there are a number of theoretical arguments that strengthen this expectation. On the other hand, the same is true of a number of other areas (weak equivalence principle, identity of charges, quantum mechanical nature of semi-macroscopic objects, ...) that are the object of careful experimental investigation. An experiment designed to measure for the first time the gravitational interaction of antimatter would be reasonable on these grounds, but there are also a number of theoretical arguments that at least allow the possibility of a difference between matter and antimatter with respect to gravity.

Gravity is described by general relativity, a classical theory that does not imply the existence of antimatter. The equivalence principle is a foundation of the theory and considerable experimental efforts have been spent and are in progress to verify its validity to high accuracy [4]. In spite of this, there has not been a single direct measurement of the gravitational acceleration of antimatter. Measurements with charged antiparticles are very difficult because the gravitational force is much weaker than the Coulomb force. Neutral antihydrogen is a unique system with which the weak equivalence principle (WEP) can be directly tested for the first time with antimatter in a completely model independent way.

Modern theories of gravity that attempt to unify gravity with the other forces of nature predict that, in principle, antimatter can fall differently from normal matter in the Earth's gravitational field. As pointed out by Scherk [5], N=2,...,8 theories of supergravity lead to the possibility of antigravity through the presence of (massive, and thus finite range) Kaluza-Klein graviscalar and gravivector components to the gravitational interaction. A graviscalar interaction will produce only an attractive interaction, while the the effect of the graviphoton is repulsive. Consequently, antimatter could experience a greater gravitational acceleration towards the Earth than normal matter [6]. Simplifying the classical potential between two point masses m_1 and m_2, the static potential in the case of one vector and one scalar partners of the graviton takes the form :

$$V = -Gm_1m_2(1 \mp ae^{-r/v} + be^{-r/s})/r \tag{2.1}$$

where a and b represent the products of the vector and scalar charges of the two particles, i.e. the coupling strengths relative to G, and v and s the ranges.

Experiments on interactions between matter and matter will be sensitive to the difference of the two terms in a and b, i.e. to $|a - b|$. Limits on this difference will not necessarily be applicable to antimatter-matter experiments, for which the sign of a changes, and which are thus sensitive to $|a + b|$. Specific (proof-of-principle) models have been constructed in which a precise cancellation takes place for matter-matter interactions [7], while leaving matter-antimatter interactions unconstrained.

Using data from Eötvos-like experiments, as well as data from experiments searching for a fifth force, limits on the range of the scalar and vector fields have been obtained [17], but without closing the door completely on differential gravitational interactions between matter and antimatter. Furthermore, these limits do not necessarily extend to couplings of e.g. a Brans-Dicke scalar in various other models [7]. More recently, models have also investigated the possibility of different baryonic and fermionic contributions

to the gravitational field [8] [9], which would again imply a differential interaction between matter and antimatter. And finally, scalar and vector couplings also appear in the context of relativistic theories of gravity based on modified Newtonian gravity [10] [11] which attempt to provide an alternative to dark matter, while new scalar fields coupling to matter with gravitational strength appear in the context of chameleon field theories [12].

These putative differences between matter and antimatter would of course violate the weak equivalence principle (WEP), a cornerstone of General Relativity, but are consistent with CPT conservation. As such, searches for such a violation of the WEP must be seen in the context of numerous recent such searches, albeit mostly with macroscopic probes [4]. Given the classical nature of General Relativity, the weak equivalence principle is expected to be violated at some level, when passing from a classical theory to a quantum theory of gravity [13]. Furthermore, as a result of earlier work by Hawking, Page and Wald, the possibility of CPT violation associated with quantum-gravity effects has recently attracted growing interest [14]. Although it is difficult to estimate the order of magnitude of any possible CPT-violating effect, which may well lie beyond experimental reach, this line of research demonstrates that quantized spacetime may result in observable CPT-violating effects. It is thus natural to also consider the possibility of searching for CPT violations in an experiment geared to probing the gravitational interaction between matter and antimatter.

It must be pointed out here that obtaining meaningful limits from experiments is rendered difficult by the uncertainty in the nature of such gravitational extensions to the standard model. Nieto and Goldman [7] underline that any new forces can be weak (i.e. have escaped detection via matter-matter interaction) either because they are intrinsically weak (small coupling strengths) or because they are the consequence of a broken symmetry with precise cancellation of parameters (in which case results from matter-matter interactions are only partly relevant): matter experiments can only lead to the conclusion that either there are no new effects, or that they cancel as if enforced by a symmetry.

Nevertheless, results from experiments with matter have been used in this context to derive upper limits on possible differences in the gravitational interaction between matter and matter, and that between matter and antimatter [15, 16, 17], but where extrapolation to antimatter is subject to the caveats underlined in [7]. For a direct investigation of antimatter, experimentally, the situation is characterized by an almost complete absence of data. Previous attempts [18, 19] on charged antiparticles were overwhelmed by systematic error sources [20], and only two experiments have been carried out on neutral antimatter: the search for gravitationally caused decoherence in the (mixed matter-antimatter) $K^0\bar{K^0}$ system [21], and the measurement of arrival time differences for (anti)neutrinos produced in SN1987a. Any conclusion on the absence of differences between neutrinos and antineutrinos relies on a single detected event containing an electron neutrino (identified at 90 % CL). Furthermore, this experiment puts no constraints on "non-Newtonian" gravitational forces with ranges much smaller than 1pc. It must be pointed out here that the ranges allowed by Eötvos-like experiments for graviscalar and gravivector interactions are far lower, astrophysical scales having been excluded [17].

Indirect arguments, originally developed by Schiff [22], often used to strongly constrain the amount of possible WEP violation for antimatter are based on the presence in any atom of virtual pairs of electrons and positrons produced in the Coulomb field of the nucleous. The hypothesis that they could react in a different way in a gravitational field would lead to violation of WEP for ordinary materials. A comparison with experimental limits suggests that violation of WEP for antimatter cannot be, if any, higher than 10^{-6} [4]. Many authors strongly criticized the calculations and the hypothesis leading to this conclusion observing that Schiff's calculation involves a gravitational coupling that is not consistent with the tensor nature of the gravitational field nor with any field theory that respects Lorentz invariance [7] [23] [24].

Limits on the validity of WEP can be obtained from frequency measurements because the weak equivalence principle links the frequency ω of any clock to the gravitational potential U. This argument can be applied to any clock with frequency ω and to the corresponding anticlock with frequency $\overline{\omega}$ but it requires the validity of CPT. If it is assumed that $\omega = \overline{\omega}$ by CPT in absence of gravitation (that is at infinity where $U \to 0$) then in a space-time point where the gravitational potential is U, a violation of WEP for the anticlock would lead to a frequency difference $\Delta\Omega = \alpha U/c^2$. From astronomical observations, an estimate of $U/c^2 \simeq 3{\cdot}10^{-5}$ can be obtained. α here is a parameter whose departure from zero describes WEP violation. This argument has been used for instance to constrain WEP violation for antiprotons to 10^{-6}, using the cyclotron frequency measurement for protons and antiproton in the same magnetic field [25].

Partly triggered by recent advances in producing relatively cold antihydrogen [1, 2], a number of concepts have thus been put forward in recent years [26], [27],[28], [29] [30] for experiments that would explicitly be sensitive to potential differences between matter and antimatter, but some of these concepts require significant further developments in technology before becoming feasible. The measurement detailed in the current proposal will thus be the first direct measurement in a laboratory to test the gravitational interaction of antimatter and matter, in a manner completely free of any assumptions, and independent on any test of CPT.

2.2 Antihydrogen and CPT

Although the main scientific goal of the AEGIS collaboration is the measurement of the gravitational interaction of antihydrogen, spectroscopy of antihydrogen, and tests of CPT invariance in particular, are of equal importance and interest. A number of technical developments planned for the second phase of the AEGIS experiment (and described in chapter 14) with the goal of very high precision gravity measurements will allow high precision antihydrogen spectroscopy as well.

Antihydrogen spectroscopy allows tests of CPT invariance which is embedded in any modern quantum field theory. It was proved in the 1950's [31] that this important symmetry in a flat space time can be deduced assuming only locality, Lorentz invariance and unitarity. The standard model for electroweak and strong interactions, together with proposed extensions, are described by a quantum field theory based on these concepts. Testing the experimental consequences of CPT is not only a test of the Standard Model or of some extension of it, but it has a more fundamental meaning: it is a test of the basic axioms of any quantum field theory. Experimental consequences of CPT regard the properties of particles and antiparticles. In particular the theorem states that every particle has an antiparticle with the opposite electric charge, the opposite internal quantum numbers, the opposite magnetic moment, the same lifetime and the same inertial mass. In addition the transition frequencies for bound states of matter and those of the corresponding states of antimatter must be the same. Although P, C, CP and T violations have been demonstrated, CPT has been verified in every experiment ever done. Since CPT is so fundamental it is important to test it with the highest possible accuracy using all types of particles: baryons, mesons and leptons. For a lepton system the most accurate test to date is the comparison of the dimensionless magnetic moments, or g values, for electrons and positrons, to a precision of $2 \cdot 10^{-12}$ [32]; in the baryon sector the charge to mass ratio of protons and antiprotons has been found equal to within 10^{-10} [25]. The meson sector offers the greatest sensitivity through the relative difference of less than 10^{-18} [33] between kaon and antikaon masses. The frequency of the 1S-2S transition in hydrogen has a relative natural linewidth of 10^{-15} and it has been measured with a precision of $1.5 \cdot 10^{-14}$ by using a very cold hydrogen beam [34]. A comparison of the 1S-2S frequency for hydrogen and antihydrogen with a precision of 10^{-15} or higher will be the most accurate CPT tests for baryons regardless of any theoretical model.

Lorentz violating extensions of the standard model have been considered and parametrized in terms of spacetime operators [35]. Some of the possible terms cause CPT violations and these can be constrained by high accuracy comparisons of hydrogen and antihydrogen. In addition it has to be noted that eleventh digit precision in determining the hydrogen and antihydrogen 1S-2S energies yields new information on the equality of the proton and antiproton charge distribution [37]. In fact the theoretical uncertainty in the calculation of the transition energy for the hydrogen atom is in the eleventh digit and is due to uncertainty in the experimental knowledge of the proton radius.

Chapter 3

The gravity measurement with a classical Moiré deflectometer and a position sensitive detector

Extremely accurate gravity measurements on cold atoms have been carried out by using atom interferometry: a sensitivity to the Earth's gravitational acceleration g of $10^{-10}g$ after two days of integration time has been reported with an atomic interferometer based on cold Cs atoms [36]. A similar experiment could be designed with antihydrogen atoms but presently such a high sensitivity is not reachable, mostly because the experimental procedures able to achieve for antihydrogen atoms the very low temperatures (μK or below) routinely obtained with matter atoms have not yet been developed. Additional, and somewhat related, strong difficulties are linked to the lack of suitable ultraviolet laser sources to be used to excite the antihydrogen following a scheme similar to the one used for Cs in the above-mentioned experiment. While the high sensitivity offered by atom interferometry remains a long term scientific goal for AEGIS and work is already in progress in the collaboration to address some of the experimental issues, we propose here a measurement of g based on the use of a classical Moiré deflectometer which is feasible with available state-of-the-art antihydrogen manipulation techniques. Before describing the proposed experiment we briefly recall the inertial sensitivity of atom interferometers, the achieved results and we set the experimental requirements for long term higher precision experiments.

3.1 General description of atom interferometers and their inertial sensitivity

The prototype of atom interferometers is the Mach-Zehnder interferometer, as represented in figure 3.1. In atom interferometers, the beam-splitters and the mirrors of optical interferometers are replaced by diffraction gratings. More precisely, in the simplest case, the incident atomic beam is split in two beams, corresponding to the diffractions order 0 and p by the first grating G_1. These two beams are reflected by grating G_2, using its diffraction orders p and $-p$ and these two beams are finally recombined by grating G_3, each incident beam being diffracted in the same two orders 0 and p. The interferometer produces two exit beams with complementary interference signals. The fringe signal measured on one of the exit beams can be written :

$$I = I_0 \left(1 + \mathcal{V} \cos(\phi)\right) \tag{3.1}$$

where I_0 is the mean intensity and $\mathcal{V}$ the fringe visibility, ϕ is a phase depending on time or space coordinates (according to the way in which diffraction is realized) and it describes the modulation of the intensity due to the interference. As discussed below, diffraction can be done with material structures made of very small wires [38], by periodical light fields (laser standing waves) [39] or by several other laser processes [40]. An interesting approach is to generate atom interference of internal states. In this class of interferometers the spatial separation of atoms is accomplished by the momentum recoil

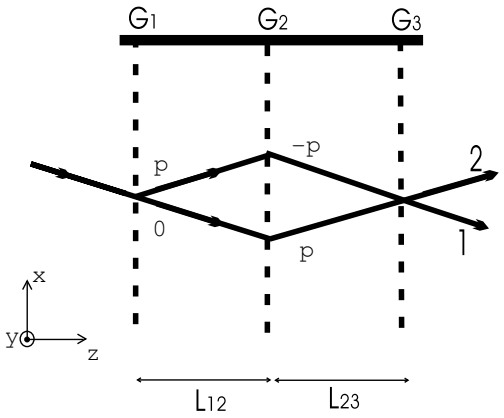

Figure 3.1: Schematic drawing of a three grating Mach-Zehnder atom interferometer, in the Bragg diffraction geometry. A collimated atomic beam is successively diffracted by three gratings G_1, G_2 and G_3. The diffraction orders corresponding to grating G_1 and G_2 are indicated on the two atomic beams. Two exit beams, labeled 1 and 2, carry complementary signals. If the gratings are material structures the sensitivity to g is obtained with slits perpendicular to the gravity force direction (g is directed along x).

induced by the electromagnetic field used to drive the atoms from one internal state to another. Raman processes are commonly used in cold atom experiments. The change of the internal state makes it very easy to distinguish the final states after a diffraction event. Atom interferometry with change of internal states is the scheme used in the mentioned atomic fountain experiments leading to high precision gravity measurements.

In all cases, a momentum equal to $p\hbar\mathbf{k}_{eff}$ is transferred to the atom by a diffraction event of order p, where $\mathbf{k}_{eff}$ is the grating wave vector. For a material grating, this vector is perpendicular to the grating lines and its magnitude is equal to

$$k_{eff} = 2\pi/a \tag{3.2}$$

where a is the grating period. In the case of laser diffraction, $\mathbf{k}_{eff}$ is the sum of the wave vectors of the photons exchanged by the atom, with a plus or minus sign depending on whether the photon is absorbed or emitted by stimulated emission.

The inertial sensitivity of matter wave interferometers was first established using a neutron interferometer in 1975 by Colella et al. [41]. Several theoretical analyses of the inertial sensitivity of matter wave interferometers have been made, [42, 40] [43, 44, 46] and all give the same result and predict a phase shift $\Delta\phi_g$ due to the acceleration of gravity $\mathbf{g}$ equal to:

$$\Delta\phi_g = \mathbf{k}_{eff} \cdot \mathbf{g}T^2 \tag{3.3}$$

where T is the time spent by the atom between consecutive diffraction gratings. It is interesting to remark that this result does not contain $\hbar$ and that the same formula holds for classical atoms transmitted by gratings without any wavelike character.

3.2 High precision gravity measurements using atom interferometers

The first high precision gravity measurement of $\mathbf{g}$ by atom interferometry was performed in 1991 by M. Kasevich and S. Chu [47, 48], using Raman diffraction induced by light pulses and laser-cooled sodium atoms launched from a magneto-optical trap (atomic fountain). S. Chu and co-workers [49, 36] have obtained a relative uncertainty $\Delta g/g = 2 \times 10^{-8}$ for a single measurement of total duration 1.3 s and later $\Delta g/g = 1 \times 10^{-10}$ after two days of integration time.

Several other experiments have demonstrated the ability to measure gravity effects by atom interferometry and related techniques: P.R. Berman and co-workers [55] made a preliminary measurement

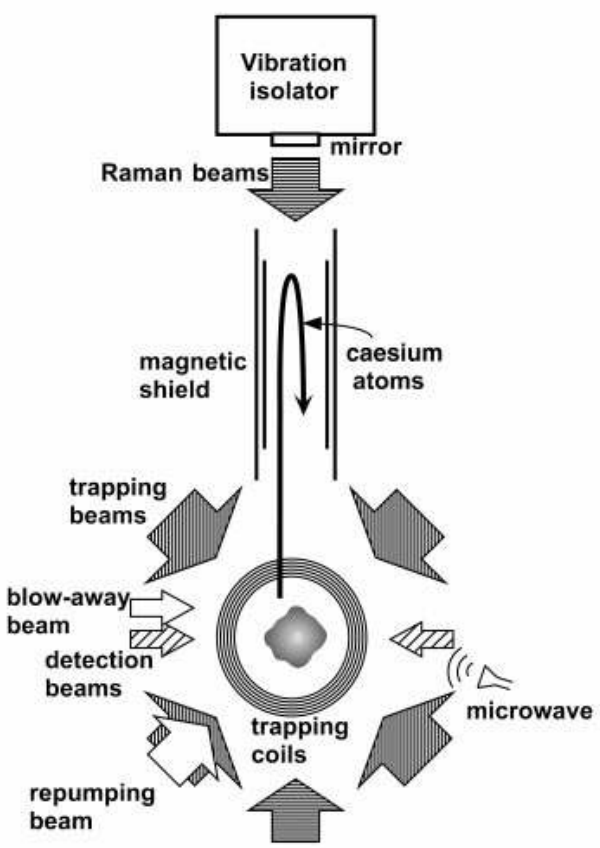

Figure 3.2: Overview of the experimental setup of [36]

of g with their echo interferometer; M. Inguscio and co-workers [57] have measured the period of Bloch oscillations of atoms in a laser standing wave in the vertical direction and this period is directly related to g; using amplitude gratings made of laser standing waves, Hänsch and co-workers [56] have built an atom interferometer sensitive to the acceleration of gravity and they have used it to test the equivalence principle with a 10^{-7} sensitivity; using also Bloch oscillations of rubidium atoms, F. Biraben and co-workers [58] have made a preliminary measurement of g with a precision of 10^{-6} ; still with Bloch oscillations, but using a strontium isotope ^{8}Sr, G. Tino and co-workers [59] (members of AEGIS) have made a preliminary measurement of g with a 5×10^{-6} accuracy.

A gravity gradiometer made of two identical atom interferometers located at different levels has been built by the research group of M. Kasevich [51, 52], with an achieved sensitivity on the gravity gradient dg/dz equal to 4×10^{-9} s^{-2}. Gravity gradiometers can be applied to the measurement of the gravitation constant G and first measurements of G have been recently carried out by the research groups of G. Tino [53] (member of AEGIS) and of M. Kasevich [54].

In the high sensitivity experiments with atomic fountains like the one of [36], and schematically shown in figure 3.2, a cloud of N cold atoms, prepared in a well–defined quantum state $|1\rangle$, moves in the vertical direction while a sequence of three light pulses with frequency ω_{eff} at times 0, T and $2T$ couple the initial state $|1\rangle$ with a state $|2\rangle$. The intensities and timing of the three pulses are adjusted so that the transition probabilities between the two states are 1/2, 1 and 1/2 respectively i.e. a $\pi/2 - \pi - \pi/2$ pulse sequence. The atoms are accelerated or decelerated by the gravitational field and this leads to a variation of the transition frequency between the two states due to the first order Doppler effect. To maintain the

resonance, the excitation frequency ω_{eff} is changed linearly with time $\omega_{eff}(t) = \omega_{eff}(0) - \gamma_\omega t$, exactly following the identical behavior with time of the atom's velocity.

A state selective detection measures the numbers N_1 and N_2 of atoms in states $|1\rangle$ and $|2\rangle$. After the last pulse the probability to find the atoms in state $|1\rangle$ is

$$P_1 = N_1/(N_1 + N_2) = 1 + cos(\gamma_\omega - k_{eff}T^2 - \Delta\Phi) \tag{3.4}$$

P_1 contains the phase shift due to gravity of eq. 3.3 and a contribution $\Delta\Phi$ related to the laser field phase that can be experimentally controlled. Measuring the number of atoms in the two states at the end of the 3 pulse sequence versus γ_ω or versus T the g value is obtained.

The high sensitivity comes from the fact that the phase shift induced by the gravity is very high ($\Delta\phi_g \simeq 10^6$) thanks to two factors. One is the possibility of using a very long flight time $T \simeq 100$ ms because the Cs atoms have been cooled down to 1.5 μK. The second one is the high value of $k_{eff} \simeq 1.6 \cdot 10^7 m^{-1}$. The excitation scheme uses Raman transitions with counter-propagating beams and the effective k_{eff} equal to about twice the optical k enters in the formula of the phase shift due to gravity.

For typical Cs or Rb experiments the number of atoms contributing to the detected signal is about $N = 10^5$ so that the phase of the signal (mod 2π) can be measured with a relative error of the order of $1/\sqrt{N} \simeq 3 \cdot 10^{-3}$. If the number of integer cycles of the phase is known then the relative error on g in these conditions is about $2 \cdot 10^{-8}$.

The interferometer signal is obtained by detecting the number of atoms in one or the other hyperfine sub-level at the exit of the interferometer: the detection scheme with alkali atoms is based on optical pumping and detection of the resulting fluorescence photons. Due to the presence of a closed transition that forces each atom to scatter a few hundred photons, the detection efficiency of alkali atoms in the ground state can easily approach unity. Quantum projection noise limited (i. e. $\Delta N/N = 1/\sqrt{N}$) detection of Cs atoms with N as low as 1000 has been demonstrated in an atomic interferometer [45].

In addition, it has to be recalled that the vertical velocity of the atoms has to be well defined. The initial quantum state of the atoms in the trap is prepared by a proper sequence of laser pulses and microwave excitations that leave in the trap a sample of atoms with a very small spread in the vertical velocity: a value of 10 nK as effective temperature of the axial motion is reported in [36]. This initial state preparation reduces the number of atoms in the trap from about $5 \cdot 10^8$ to about $5 \cdot 10^6$. This selected sample then flies in the vertical direction where the sequence of Raman pulses is applied.

The realization of a similar experiment with antihydrogen requires a cold antihydrogen source. Laser cooling of antihydrogen atoms trapped in a magnetic trap is one of the most promising methods to cool the formed antihydrogen. The minimum temperature achievable is limited by the Doppler limit and it is 2.4 mK, much higher than the values reachable by laser cooling on alkali atoms. Cooling the antihydrogen below this value requires the development of new procedures [70].

If we assume to launch antihydrogen atoms with a temperature of $\simeq mK$, after about 10 ms the antihydrogen cloud reaches a few cm. The need to limit the dimension of the cloud in the horizontal plane constrains T to few ms. If we assume to induce Raman transitions using Lyman-α radiation then k_{eff} for antihydrogen is about 10 times the corresponding value for Cs. If 100 antihydrogen atoms are detected at the end of the interferometer, then the precision of the gravity measurement will be in the 10^{-4} range. The precision scales linearly with the temperature and with the square root of the number of detected atoms. If large numbers of trapped antiatoms are available and a large flux reduction can be tolerated, then it is possible to collimate the antiatoms at the exit of the trap and use in the fountain only those with small horizontal velocity. This allows to increase T and the sensitivity to g.

The detection efficiency is not the major issue because the scheme based on trapped states used for alkali atoms can be used with antihydrogen too. Some concerns regard the reduction of scattered photons due to the high momentum diffusion related to both atom mass and photon momentum. On the other hand photon counting is much more efficient. Assuming a detection efficiency close to unity is then probably reasonable.

The excitation scheme with Raman transition requires phase controlled Lyman-α radiation and this is presently a big experimental challenge. Interferometer schemes that could avoid the use of intense CW phase–controlled Lyman–α sources can be considered. So far atom interferometry has been demonstrated in a beam of 7 K hydrogen atoms in the metastable $2S$ state using as state $|2\rangle$ the $15P$ state with T=200 ns limited by the lifetime of $|2\rangle$ [50].

A high precision gravity measurement is the long term scientific goal of this collaboration and an atom interferometer with light pulses is the device offering the highest sensitivity to g. Before proposing an experiment of this type however, we believe that several developments are still necessary: they can be summarized by saying that antihydrogen with sub mK temperature is needed and a powerful CW Lyman-α laser source is an essential tool to manipulate these atoms. Some of these developments are already in progress inside this collaboration (see chapter 13) and members of AEGIS of Florence and Toulouse have direct experience with the described types of atom interferometers, which are currently in operation in their laboratories.

The experiment we are proposing to carry out in the first phase of AEGIS is a gravity measurement based on the horizontal deflection of an antihydrogen beam through a Moiré deflectometer, and does not require antihydrogen trapping. Given the higher temperature of the antihydrogen beam in this first experiment, the expected precision will of course be reduced.

3.3 The AEGIS antihydrogen beam

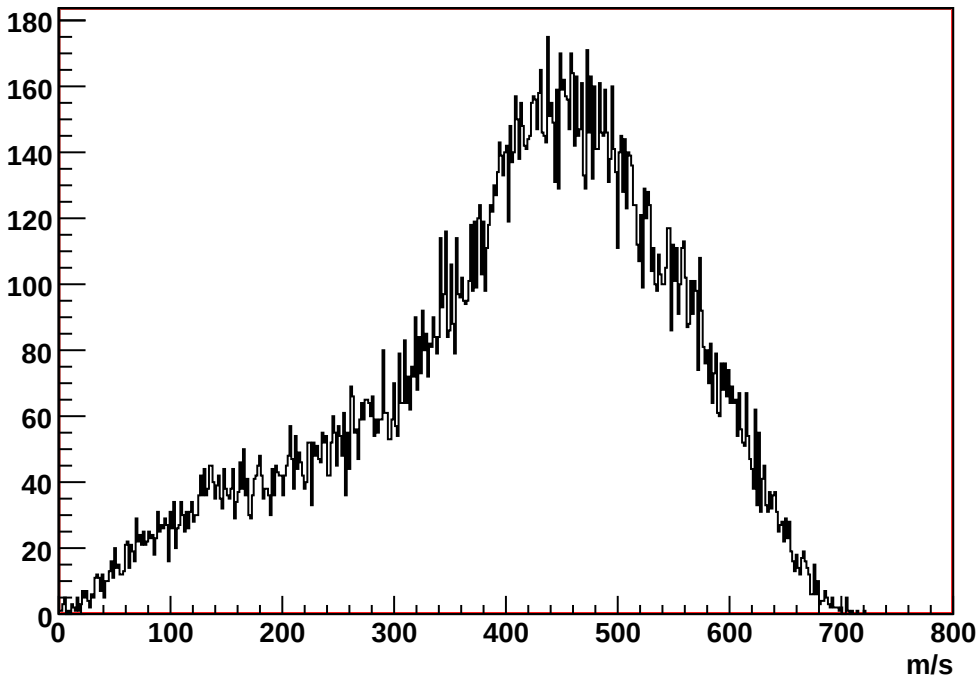

Figure 3.3: Example of the horizontal velocity distribution of an antihydrogen beam obtained by accelerating Rydberg states with n distributed following a Gaussian shape with mean value n=30 and rms =4.

In the AEGIS apparatus a beam of antihydrogen will be produced through the horizontal acceleration of Rydberg antihydrogen in an inhomogeneous electric field. The basic design of the AEGIS experiment allows the production of a beam with a horizontal velocity v_h in the range of few hundreds m/s and a transverse velocity v_t of the order of few tens m/s. An example of the velocity distribution (obtained with a simulation) is shown in Fig. 3.3. This simulation refers to antihydrogen accelerated from an initial Maxwell distribution at 100 mK and having initial positions uniformly distributed in a region 8 mm long in the axial (horizontal) direction and within a radius of 1.5 mm.

The range of the axial velocity and the shape of the velocity distribution are determined by parameters

that are under experimental control: these are the antihydrogen internal state distribution and the space time behavior of the applied accelerating electric field. That means that the shape of the velocity distribution reported in Fig. 3.3 should only be taken as an example.

The antihydrogen beam is obtained by applying an appropriate electric field for a time interval $\Delta T_E \simeq 70\ \mu sec$ and the velocity distribution shown in Fig. 3.3 represents the velocity of the antihydrogen atoms at the time t_0 (experimentally known) when the electric field is switched off. The distribution of the axial position z_s of the antihydrogen atoms at the time t_0 is shown in figure 3.4.

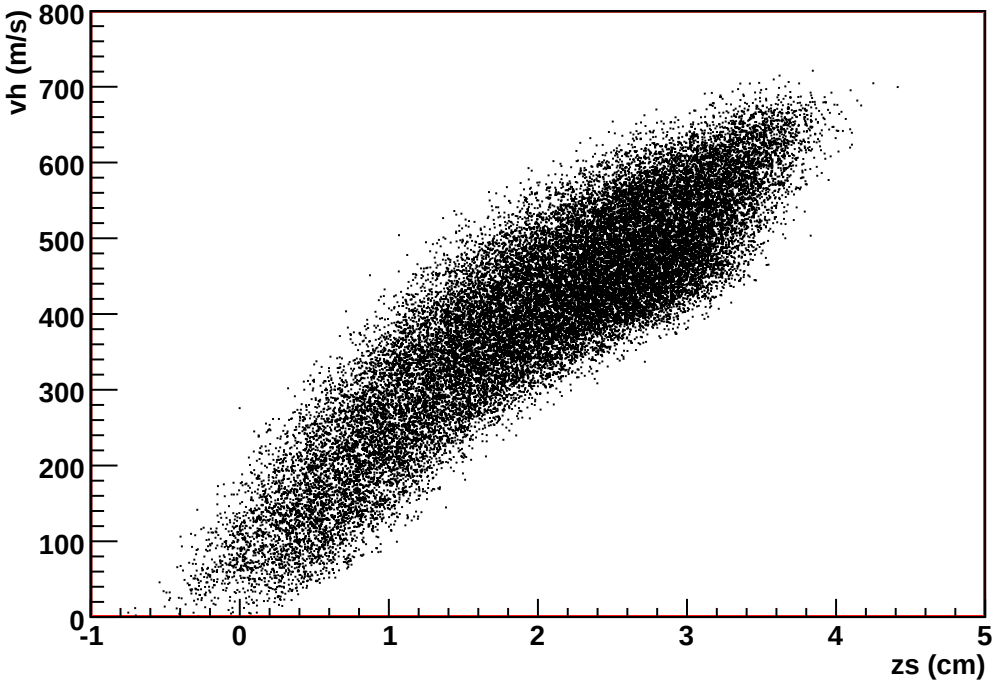

Figure 3.4: Scatter plot of the horizontal antihydrogen velocity v_h versus the axial position z_s at the time t_0 for the same antiatoms as in Fig. 3.3

The results shown in that figure are conservative values achievable with a basic design of AEGIS that does not include the possibility of radially cooling the beam and accelerating all the produced antihydrogen without manipulating first their internal states.

Radial cooling of the antihydrogen beam can be performed with state-of-the-art technologies (pulsed Lyman-α light) and it will be implemented in AEGIS. In this case the beam divergence can be greatly reduced. In principle the minimum radial velocity is a few m/s (corresponding to the Doppler limit). A proper manipulation of the antihydrogen internal states before the acceleration (antihydrogen decay and re-excitation to a well defined quantum state) will allow the production of a beam with a narrower v_h spread.

The antihydrogen flux will be a few antiatoms/second and the consequence is that, regardless of the measurement scheme, the g value will be obtained by accumulating the signal of individual atoms over several days or weeks.

3.4 Current difficulties in diffracting an antihydrogen beam though material gratings

Diffraction by material gratings could be used to build an atom interferometer having a beam as source. The typical setup is that of a Mach-Zender interferometer of figure 3.1 where the gratings are material

gratings with period a and the force due to gravity acts in the x direction. Matter wave interference can be observed if the grating period a and the de Broglie wavelength $\lambda_{dB} = \frac{h}{mv}$ of the atoms satisfy

$$a \ll \sqrt{\lambda_{dB} L} \tag{3.5}$$

If this relation is not fulfilled then quantum effects can be neglected and the passage of the atoms through the gratings follows classical trajectories. The grating system working in the classical regime is called Moiré deflectometer. If $v_h = 10^3$ m/s then $\lambda_{dB} = 4 \times 10^{-10}$ m and the grating device works as atom interferometer if $a \ll 20\ \mu m$.

Diffraction of an atom by material gratings is usually assumed to be always possible. However, with anti-hydrogen, this idea must be discussed as a function of the internal state, especially because we are interested in a coherent diffraction process:

- if anti-hydrogen is in its $n = 1$ ground state, diffraction should be feasible without any particular difficulty.

- if anti-hydrogen is in its $n = 2\ ^2S$ metastable state, the grating must not create an important electric field which would quench the metastability of this state. In particular, a non negligible electric field may exist in the slits if some electrical charges are deposited on the grating surface and gratings made of a metal should be preferable to dielectric gratings. However, the time passed by the atom near the grating is very brief (this time is of the order or 3×10^{-10} second for a 300 nm thick grating crossed at a mean velocity $v_h = 1000$ m/s) and metastability quenching may occur with a low probability (this probability could be measured with an experiment using hydrogen atoms in the same state). The other effects of a grating are discussed in the case of Rydberg states.

- if anti-hydrogen is in a Rydberg state, many difficulties can be foreseen due to their sensitivity to electric and magnetic field gradients. The van der Waals atom-grating interaction is very large and this interaction is state-dependent. The accumulated phase [66] while crossing the grating may be large and this phase, which is velocity dependent (a simple perturbation calculation shows that it is proportional to $1/v$) will reduce the coherence of the diffraction process.

  Moreover, a transition from one sub-level to another one of the same Rydberg multiplicity corresponding to a given value of the principal quantum number n is also possible. This transition will destroy the coherence of the diffraction process for the following reason: the modification of the internal energy of the atom will come from the translation energy of the atom and, even if the energy exchanged is very small, the propagation phase will be modified: to give an example, if a transition occurs between two states with an energy splitting $h\nu$ with $\nu = 1$ MHz, this energy change will take only 1 microsecond to induce a phase shift of the atomic wave equal to 2π. As a consequence, we think that a coherent propagation of a manifold of Rydberg states is possible only if carefully controlled electric and magnetic fields are present and that no Majorana transitions from one state of the manifold to another one can occur.

Atomic diffraction by material gratings has been mostly studied by D. Pritchard and co-workers [38, 46] and by J. P. Toennies and co-workers [60]. Typical gratings used for atom interferometers have a period a in the 100-200 nm range with an open fraction β near 50% and the surface of such gratings is about 1 mm^2 [61, 62]. Gratings with larger periods are easier to produce but small periods are necessary to separate the various diffraction orders and the interferometer exit beams. The gravitational phase shift $\Delta\phi_{grav}$ is given by eq. 3.3 where $T = L/v$ is the time spent by an atom to go from one grating to the next (distance between gratings equal to L). For a grating period $a = 100$ nm, a distance between consecutive gratings $L = 1$ m, we get $\Delta\phi_g = 630$ radians if $v_h = 1000$ m/s.

Other types of material grating interferometers work in the so called Talbot-Lau regime. The theory of Talbot-Lau matter wave interferometer has been developed by J. F. Clauser and Shifang Li [68] and by B. Dubetsky and P. R. Berman [69]. It seems very similar to a three grating Mach-Zehnder atom interferometer but the gratings operate in the near-field or Fresnel diffraction regime while the Mach-Zehnder interferometer is in the far-field or Fraunhofer diffraction regime. Practically, this means that to observe fringes with a good visibility, the distance L between consecutive gratings must be equal to the Talbot length L_T given by:

$$L_T = \frac{a^2}{\lambda_{dB}} \tag{3.6}$$

This condition gives the grating period value once the wavelength and the dimension of the apparatus are defined. For instance, if we choose $L = 0.2$ m, with $\lambda_{dB} = 4 \times 10^{-10}$ m, the period a must be $a = 9 \times 10^{-6}$ m, and the phase-shift due gravity is equal to:

$$\Delta\phi_g = \frac{2\pi}{a} g \left(\frac{L}{u}\right)^2 = 0.28 \text{ rad} \tag{3.7}$$

This phase shift, which scales like $(L/v)^{3/2}$, could be made larger either by increasing L or by choosing a lower value for the velocity for which the fringes have the best visibility.

In every case the interference pattern is measured by scanning the position of the third grating along the direction of the gravity force and counting the total number of atoms transmitted as a function of the position of the third grating.

This diffraction process by material gratings does not modify the internal state of the atoms. The exit beams of the interferometer can be distinguished only by their direction of propagation. The associated difficulty is that the incident atomic beam must be highly collimated to allow the separation of the output beam from the direct one. For a grating period a, the first order diffraction angle θ is given by:

$$\theta = \frac{\lambda}{a} \tag{3.8}$$

For a velocity $v_h = 10^3$ m/s corresponding to $\lambda_{dB} = 4 \times 10^{-10}$ m, a grating with a period $a = 100$ nm gives a first order diffraction angle $\theta = 4$ milliradians: this angle will fix the needed collimation of the atomic beam and the necessary ratio between the horizontal and vertical antihydrogen velocity. For v_h =1000 m/s a transverse velocity of $v_t = 4$m/s is needed corresponding to a kinetic energy of 0.9 mK. A more relaxed requirement is obtained in the case of a Talbot-Lau interferometer. Laser cooling by pulsed Lyman-α laser will be implemented in AEGIS and it is a powerful method to radially cool the antihydrogen beam. The resulting limit on the energy is in the right range but the efficiency will depend on the radial cross section of the beam. So, even if the technologies that we are developing are promising, it is hard to establish now that an interferometric measurement with material gratings is feasible.

Additional difficulties come from the need for a large flux of atoms due to the fact that the transmission of an atom interferometer made of three material gratings is considerably less than 1. There are two effects, one of fundamental nature due to the diffraction efficiency and one of technical origin due to support bars.

Neglecting atom-surface interaction [67, 66], the diffraction efficiency of an ideal grating is given by:

$$\alpha(p) = \frac{\sin(p\pi\beta)}{p\pi} \tag{3.9}$$

where p is the diffraction order and β the open fraction of the grating period. With typical β values close to $\beta = 0.5$, assuming diffraction orders $p = 0, \pm 1$, we calculate a mean transmission T_{mean} (average of the constructive and destructive interference cases) equal to:

$$T_{mean} = 2\left|\alpha(0)\alpha(1)\alpha(-1)\right|^2 = 2/\pi^2 \approx 0.02 \tag{3.10}$$

The effect due to the support bars [38] may be estimated: there are ≈ 1 μm wide support bars every 4 μm, these bars being perpendicular to the grating lines. The associated transmission is about 3/4. There are also bigger bars (about 35 μm wide) parallel to the grating lines every 150 μm. In both directions, the transmission is about 3/4 leading to a total transmission equal to $9/16 = 0.56$ for one grating and for three gratings, we expect $(9/16)^3 = 0.18$.

Diffraction of antihydrogen by laser standing waves has also been considered by us and can at present be ruled out.

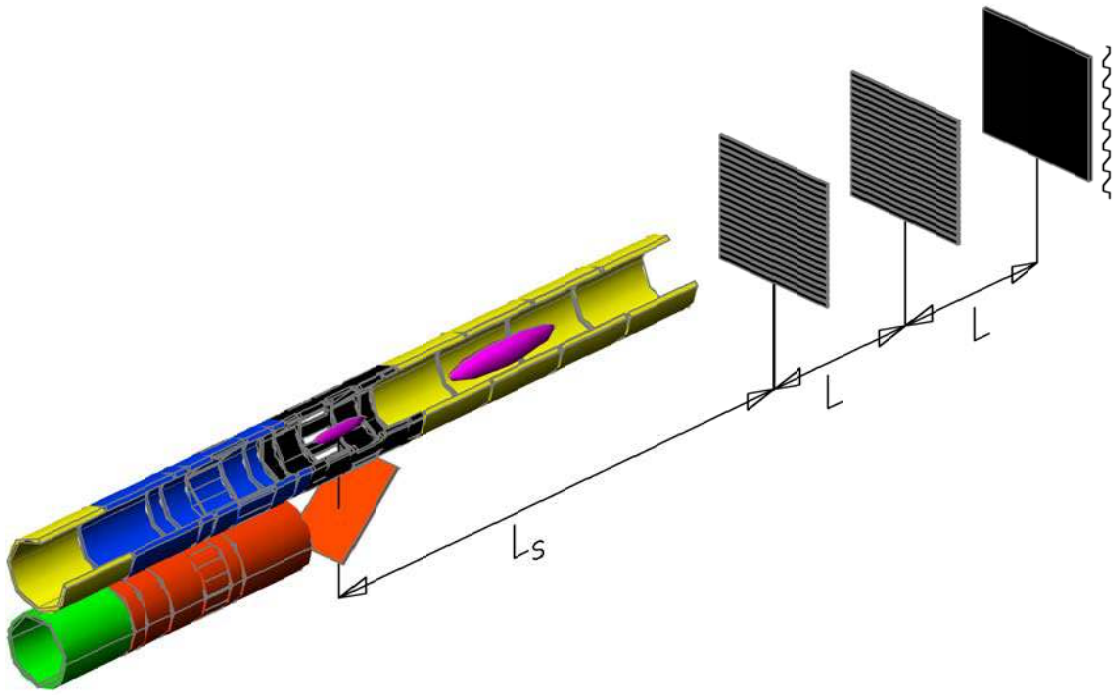

Figure 3.5: Schematic view of the AEGIS Moiré deflectometer (not to scale). The cylinders represent the electrodes of the trap for charged particles in which the antihydrogen will be produced. The first cloud represents the antihydrogen before the acceleration and the second one the cloud at the time t_0 when the accelerating electric field is switched off. The two gratings and the detector are shown.

3.5 The first AEGIS gravity measurement: a classical Moiré deflectometer coupled to a position sensitive detector

The first experiment planned in AEGIS to probe the validity of the weak equivalence principle for antihydrogen is the g measurement with a classical Moiré deflectometer. Such an apparatus was built and operated by M. K. Oberthaler et al., in 1996 [64] and we are proposing an upgraded design of it (M. K. Oberthaler is member of AEGIS).

A classical deflectometer is usually made of three gratings, but the slit widths are sufficiently large that diffraction can be neglected. Referring to relation 3.5 for $L = 0.1$ m, $a = 40$ μm and for $L = 1$ m, $a = 120$ μm. As already anticipated, the motion of the atoms in the Moiré deflectometer is purely classical. The presence of the first two gratings at distance L produces a periodical structure in the number of the atoms $N(x)$ arriving at distance L from the second grating. Here x is the coordinate in the direction of the gravity force. In the experiment described in [64] the atomic density modulation was detected, as in the case of the interferometer experiments, by using the third grating as filter: the third grating is moved in the vertical direction by a fraction Δ_x of the grating period and the total number of atoms passing through is detected vs Δ_x.
The number of atoms $N(\Delta_x)$ is a periodical function of Δ_x with period $k_{eff} = 2\pi/a$.
The comparison of $N(\Delta_x)$ with and without including the gravity force shows that the fall of the atoms

due to gravity induces a shift in $N(\Delta_x)$ exactly given by eq. 3.3 as in the atom interferometer. The effect here is purely classical. The Moiré deflectometer allows to enhance the sensitivity in the measurement of the gravity induced vertical deflection of the antihydrogen beam traveling in the horizontal direction through the gratings. Assuming a path length of about 1 meter and a horizontal velocity of 500 m/s, the deflection is only $19.6\mu m$. This deflection would be impossible to determine with a beam with a final radial diameter of the order of ten cm. The gravity induced phase shift however can be seen as the atom beam's deflection during the flight between the two gratings, measured in units of the grating vector.

The ultimate sensitivity of the classical deflectometer is inferior to that of an atom interferometer because the grating wave-vector is smaller, but its significant advantage is that a collimated beam is not required.

The upgraded design that we are proposing is based on the use of a position sensitive detector in place of the third grating. This innovative design of the Moiré deflectometer allows the use of antiatoms in an efficient way and thus reduces the measurement time. This solution cannot be adopted in the case of the atom interferometer because the required position resolution is too high. This scheme was already envisaged in our letter of Intent [65].

3.5.1 Sensitivity to the antihydrogen beam initial conditions

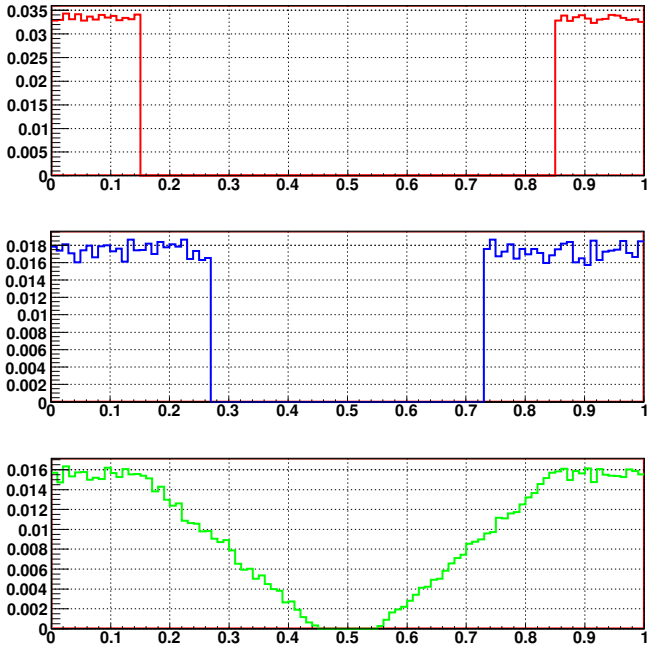

Figure 3.6: Number of atoms detected at distance L from the second grating versus x/a. The force due to gravity is not included. The 3 plots refer to different initial conditions for the source. From top to bottom the plots are obtained with an extended source with $v_t = 0$; with a point-like source where v_t taken from a 100 mK Maxwell distribution; with an extended source and 100 mK radial temperature.

We show here the results of simulations of the behavior of the Moiré deflectometer coupled to a position sensitive detector.

The fraction f_N of atoms arriving on a surface of radius w at a distance l from the source is

$$f_N = \frac{w^2}{l^2}\frac{v_h^2}{v_t^2} \tag{3.11}$$

where v_h is the horizontal velocity and v_t is the transverse velocity. Assuming $l \simeq 1$ m, $v_h \simeq 500$ m/s $v_r = 50$ m/s we easily see that a grating radius and a detector size $w \simeq 10$ cm are needed to detect all the atoms.

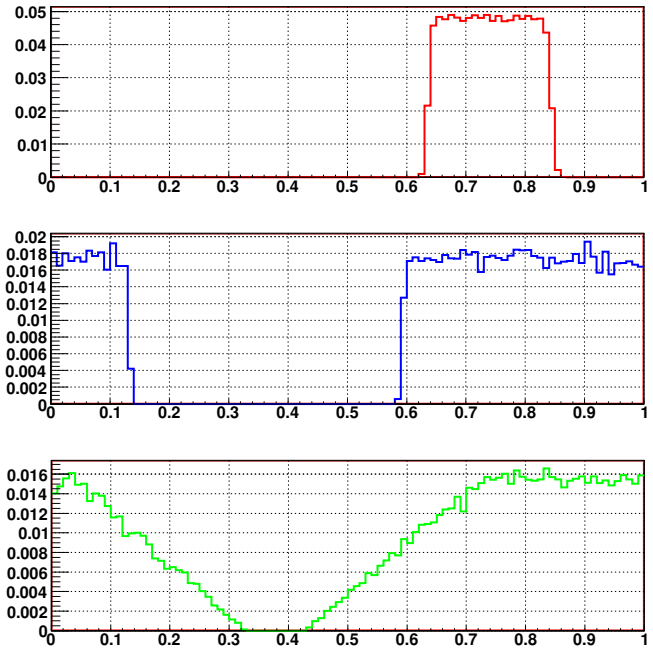

Figure 3.7: As in fig 3.6 but including the force due to gravity.

The simulation results shown below refer to $L = 40$ cm (grating-grating distance and detector-second grating distance), a grating period a of 80 μm and an opening fraction $f = 0.3$. The value of the opening fraction was already optimized in [64]. We also assume that the distance between the first grating and the center of the antihydrogen cloud before the acceleration is $L_s = 30$ cm. Typically we consider a radial velocity corresponding to 100 mK and a radial beam extension of 1 cm radius. Figure 3.5 shows a schematic of the setup.
The grating size and the detector size are large enough (20 cm radius) to ensure that the antihydrogen losses are mainly due to the grating transparency: the fraction of transmitted atoms is 9%. We assume that the antihydrogen velocity during the flight changes only due to the effect of the gravitational field. Figures 3.6 and 3.7 show that the Moiré deflectometer does not require a collimated beam. Figure 3.6 shows the number of atoms arriving at the position of the detector (here we assume infinite position resolution) in three extreme cases without including the force due to gravity. The plot is obtained by counting in the same bin the antiatoms whose x differs by an integer multiple of the grating period and thus extends over only one period. The first plot is obtained launching $5 \cdot 10^5$ antiatoms with $v_t = 0$ and $v_h = 400$ m/s from an extended (3 cm radius) source. The obvious shadow effect due to the 30% opening fraction of the gratings is clearly visible.

The second plot is obtained assuming that the antiatoms have a transverse temperature of 100 mK and that they originate from a point-like source. The last plot is the result obtained launching antiatoms with 100 mK from an extended (3 cm radius) source. In figure 3.7 the gravity force is included. The gravity induced shift of the $N(x)$ function is evident in all three cases.

The value of x/a in Figs. 3.6 and 3.7, corresponding to the minimum in the number of detected counts (the " absolute phase Φ_0" of those curves), depends on the alignment between the two gratings, and on the alignment between them and the center of the antihydrogen cloud. We have verified with the simulations that Φ_0 is insensitive to the radial antihydrogen velocity and to the radial antihydrogen beam radial section within the range of parameters of our interest. Of course the radial velocity influences the number of atoms arriving on the detector and so it must be kept as low as possible. The following simulations always assume a Maxwell radial velocity distribution with 100 mK temperature. The phase shift induced by gravity is independent of Φ_0.

3.5.2 Required position resolution

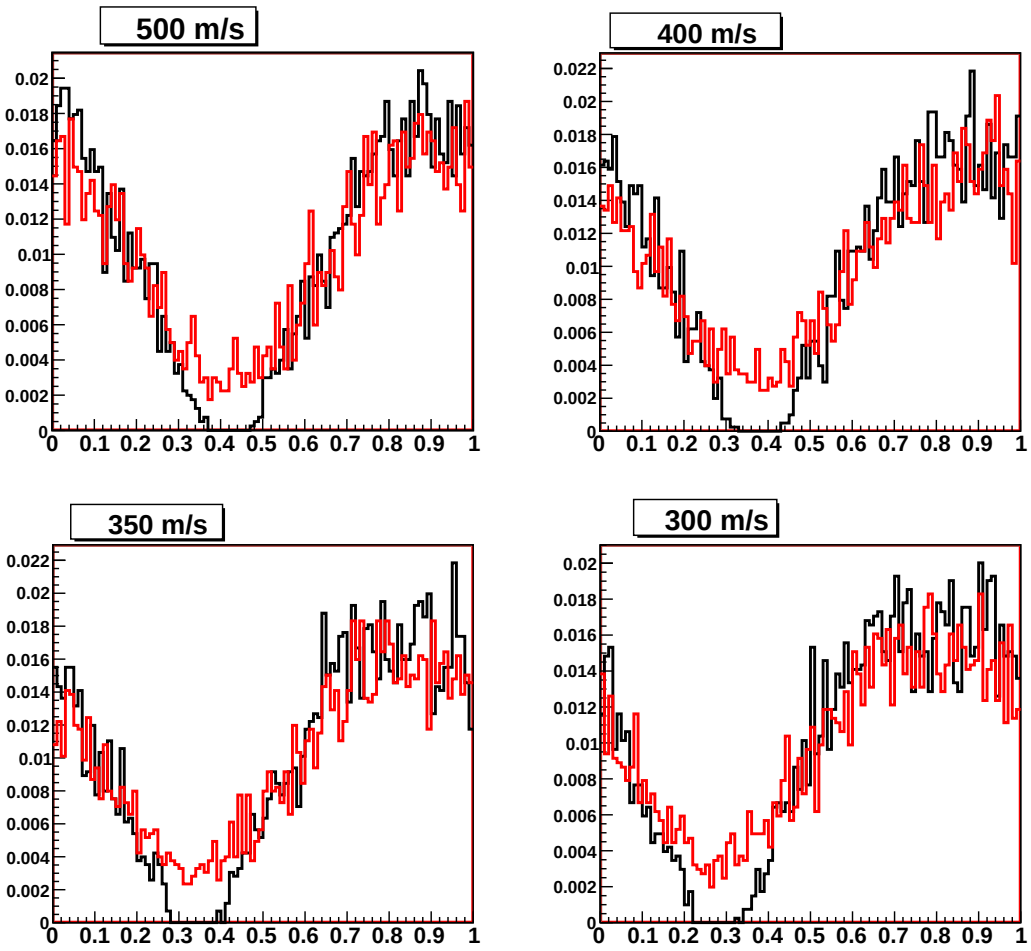

Figure 3.8: Fraction of atoms detected as a function of the x coordinate (grating units) The total number of counts is $4 \cdot 10^3$ for every axial velocity. The black plot is obtained with infinite position resolution ($\sigma_{det} = 0$) while the red one is the result with $\sigma_{det} = 10\mu m$.

A detector able to measure the antihydrogen arrival time t_{det} and its position with a resolution σ_{det} is simulated by assigning to each antiatom arriving at a distance L from the second grating a position x randomly sampled from a Gaussian distribution centered on the true antiatom x and with a σ equal to that of the detector. Figure 3.8 shows the number of counts N(x) obtained with antihydrogen with four different axial velocity values ($4 \cdot 10^3$ antiatoms are detected for every velocity). The velocity spread is negligible in these plots; its effect will be discussed later. The optimal procedure to extract the phase shift from these plots is under study. The results shown here are obtained multiplying $N(x)$ by a mask function $m(x, \Delta_x)$ and then studying the integral $N(\Delta_x) = \int N(x)m(x, \Delta_x)dx$ versus Δ_x. $m(x, \Delta_x)$ numerically represents the response function of a third grating (identical to the first two) and shifted vertically by Δ_x.
Figure 3.9 compares $N(\Delta_x)$ obtained from the data of Fig. 3.8 with $\sigma_{det} = 0$ and $\sigma_{det} = 10\mu m$. Figure 3.10 refers to $\sigma_{det} = 17.5\mu m$.
$N(\Delta_x)$ shows a behavior like a cosine function plus a constant offset. Its exact shape in general is not a cosine. Fitting this function with $A + Bcos(\frac{2\pi\Delta_x}{a} + \Phi_g)$ in a restricted interval, we obtain the Φ_g phase shift due to gravity. Here $\Phi_0 = 0$. The effect of the finite detector resolution is the reduction of the amplitude of the oscillation (contrast) and a "flattening effect " of the function around its maximum

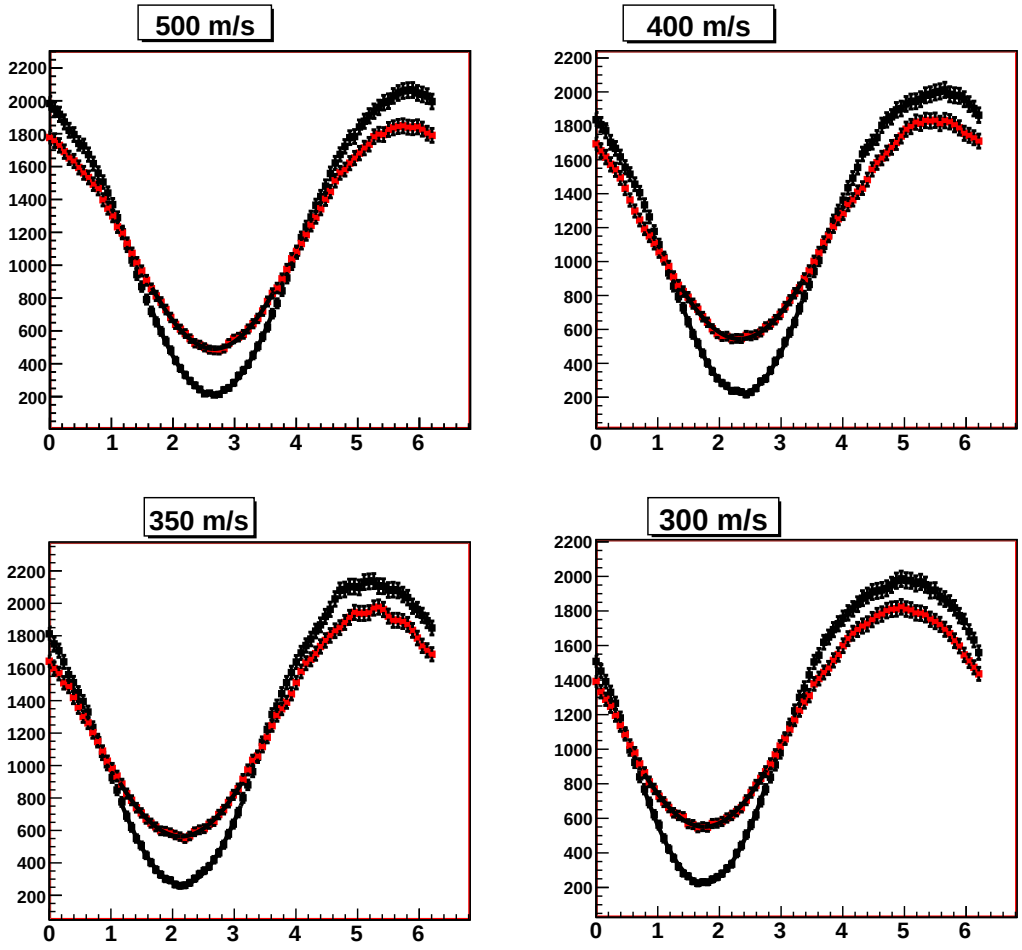

Figure 3.9: Fraction of atoms $N(\Delta_x)$ detected as a function of the shift Δ_x (grating units multiplied by 2π). The total number of counts is $4 \cdot 10^3$ for every axial velocity. The black plot is obtained with infinite position resolution ($\sigma_{det} = 0$) while the red one is the result with $\sigma_{det} = 10\mu m$. The position of the minimum in these plots is π in absence of gravity.

or minimum. The precision in the determination of the phase σ_{Φ_g} with $\sigma_{det} = 0$ resulting from the simulations is

$$\sigma_{\Phi_g} = \frac{0.4}{\sqrt{N}} rad \tag{3.12}$$

Here N is the number of detected antiatoms. Using the same fitting function when the detector resolution is included the phase value is correctly reproduced but an increase of σ_{Φ_g} is obtained. This corresponds to a factor (2-2.5-3-4) respectively with $\sigma_{det} = 10, 12.5, 15, 17.5\ \mu m$ and $N \simeq 10^3 - 10^5$. For higher values of σ_{det} systematic errors influencing the phase value become important. A detector vertex resolution not worse than 10-13 μm is required.

3.5.3 The required precision on the time-of-flight

To recover g from the measured Φ_g value it is necessary to know the time of flight T of the antiatoms between the two gratings. If all have the same velocity then $T = L/v_h$. If antiatoms having different axial velocities are grouped together to build plots of the type shown in Fig. 3.9 then each one of them contributes to the signal with its phase shift. The result is still a function similar to that of Fig. 3.9 but an effective value T^2_{eff} has to be used instead of $T^2 = L^2/v_h^2$. Under general conditions T^2_{eff} depends on the

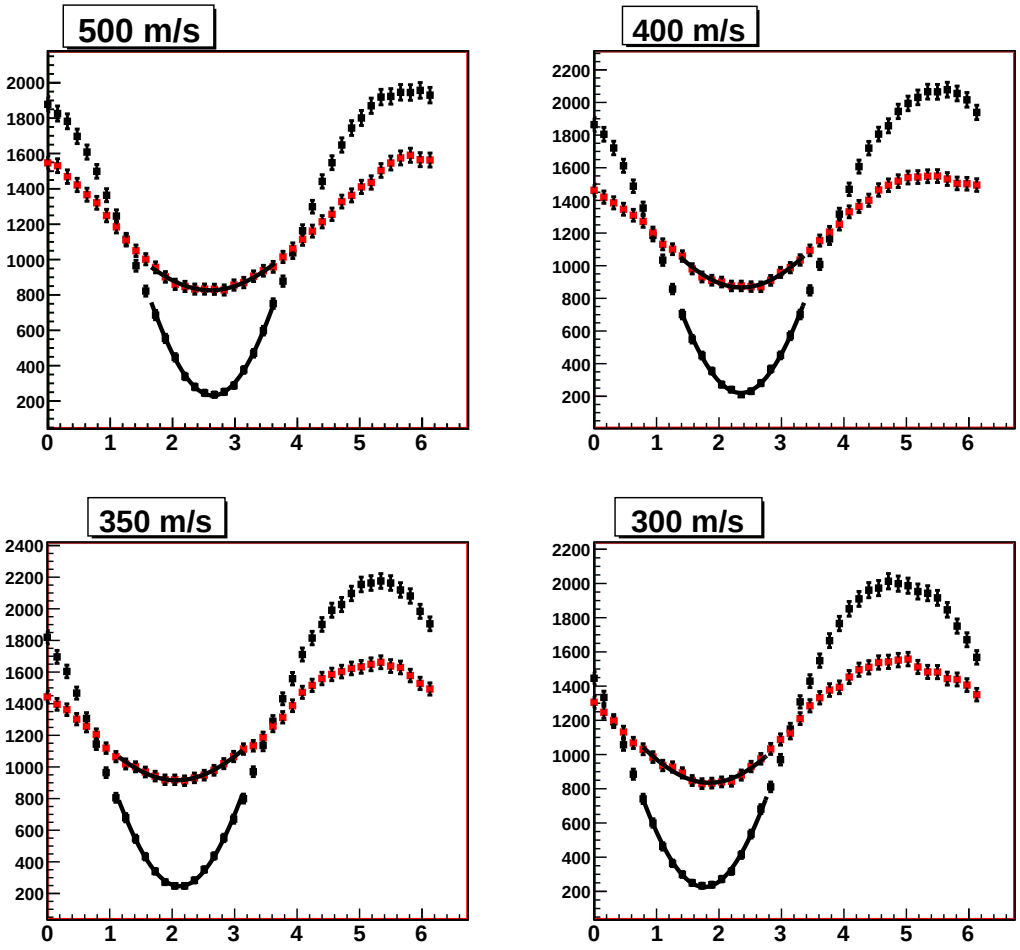

Figure 3.10: As figure 3.9 but $\sigma_{det} = 17.5\mu m$.

shape of the time of flight distribution (that is, on the shape of the horizontal velocity distribution) and the data analysis is based on a comparison between the data and a Monte Carlo simulation. This grouping of the antiatoms is necessary in our conditions due to the large velocity spread of the produced antiatoms. In the simple, but experimentally easy to achieve, case in which antiatoms with different velocity, but having a distribution of T^2 symmetric around its mean value, are grouped together, the phase shift is independent of the shape of the distribution of T^2 and $T^2_{eff} =< T^2 >$. $< T^2 >$ is the mean value of the measured distribution of T^2. We have verified this fact in the simulation by building symmetric T^2 distributions with variable rms σ_{T^2} and fitting the corresponding $N(\Delta_x)$ simulated signals: the result is that the phase shift is unchanged, within its error bar, if the signal $N(\Delta_x)$ is built with antiatoms having σ_{T^2}/T^2 ranging from zero to values as high as several tens of %. Note that the error of $< T^2 >$ is the rms of the measured distribution divided by the square root of the number of antiatoms used to build the signal and so it is quite easy to achieve values below 1%, which are thus negligible in our conditions.

As a practical example we consider the signal obtained by sending the beam with the v_h distribution of Fig. 3.3 through the deflectometer. The initial axial position z_0 of each antiatom at the time t_0 is taken from Fig. 3.4.

The flight time T between the two gratings is reconstructed from the knowledge of t_0 (the time when the accelerating electric field is switched off) and the arrival time t_{det} on the position sensitive detector through

$$T = \frac{L}{2L + Ls - z_s} \tag{3.13}$$

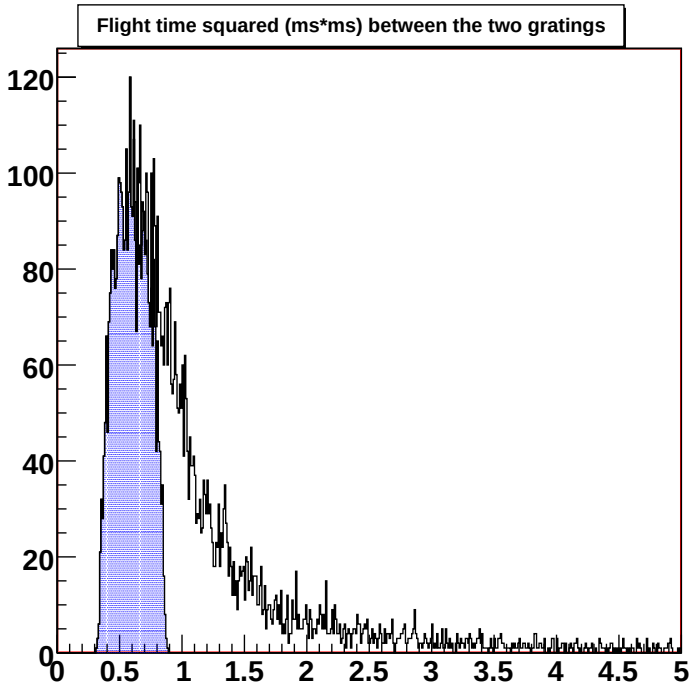

Figure 3.11: Squared time-of-flight ($(ms)^2$) of the detected antiatoms after the flight through the deflectometer and having their horizontal velocity distributed according to Fig. 3.3. The shaded area corresponds to the shaded area in Fig. 3.13

The main source of uncertainty here is due to the impossibility of knowing z_s, the initial position before acceleration, for every detected antiatom. However, the mean value of z_s is of course known, and - since the accelerating field is spatially limited - variations in z_s are small with respect to $2L + L_s$. Fig. 3.11 shows the distribution of T^2: the black plot refers to all the antiatoms while the blue one is built selecting only the antiatoms with a distribution of T^2 centered on 0.6 ms^2 and symmetric (within the statistical fluctuations).

Figure 3.12 shows the corresponding $N(\Delta_x)$ signals.
The phase obtained with the blue plot gives, within the errors, the correct g value using $T^2_{eff} =< T^2 >$ while the phase of the black plot furnishes the right g value using T^2_{eff} lower than $< T^2 >$. Figure 3.13 shows the velocity distribution of the detected antiatoms: the blue histogram refers to the selected antiatoms with the symmetric T^2 distribution.

These results show that by a proper grouping of the detected antiatoms, all the antihydrogen in the beam can be used to build the signal. Higher statistics in the low velocity region are obtained by reducing the accelerating field.

3.5.4 Required number of antiatoms for a 1% precision on the gravity measurement

The strength of the coupling constant to gravity, g, is obtained by measuring the phase shift for antiatoms with several $< T^2 >$ and then fitting a parabola (eq. 3.3) through the points. Fig. 3.14 shows the phase as a function of $\sqrt{< T^2 >}$ between the two gratings and the fitted value of g obtained with nine velocity binnings of antiatoms. The mean velocity in each bin is $600 - 550 - 500 - 450 - 400 - 350 - 300 - 250 - 200$ m/s. The number of antiatoms detected in each velocity bin is 10^3 and the radial temperature is $100mK$ as in the whole simulation. The total number of antiatoms used is $1.3 \cdot 10^5$.

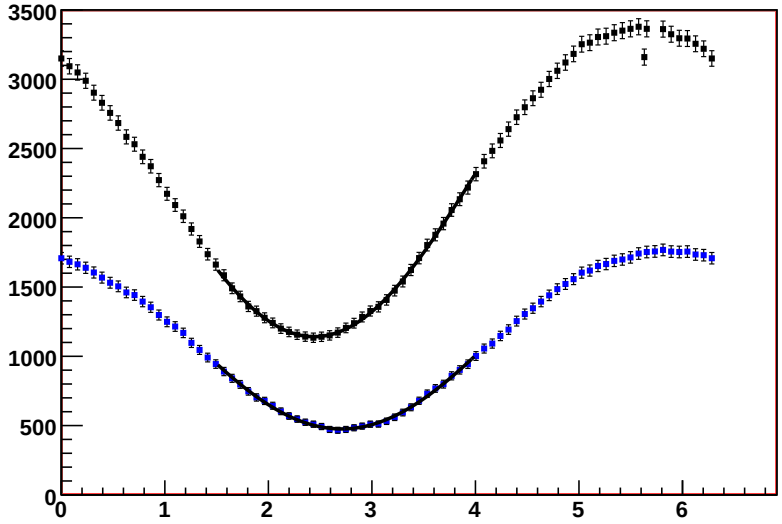

Figure 3.12: $N(\Delta_x)$ (grating units multiplied by 2 π) signal obtained using all the antiatoms of the distribution of Fig. 3.3 (black plot) and the corresponding signal obtained by selecting only the antiatoms whose measured time-of-flight squared is distributed symmetrically around 0.6 ms^2 (blue plot).

The fit result obtained with 10 μm detector resolution is 9.8 ± 0.13. The corresponding value obtained with infinite detector resolution is 9.8 ± 0.1. Assuming a production rate of useful antihydrogen of 1 Hz and access to antiprotons for 25 % of a day, the measurement would require of the order of two weeks of beam time. Here antihydrogen atoms are considered useful if their horizontal velocity can be determined as described and their radial velocity follows a thermal distribution with a temperature not higher than 100 mK. Note that the assumption on the radial velocity is conservative because we have not included here the possibility (discussed in chapter 13) of performing radial cooling of the beam. In addition, during the axial acceleration procedure detailed in chapter 11, some radial cooling is expected to take place but it is not included in these simulations. A substantial radial cooling of the beam will allow to increase the distance between the gratings and/or to use atoms with very low horizontal velocity. All these factors increase the gravity induced phase shift and thus the sensitivity to g. If systematic errors can be controlled, then the precision of the measurement could be higher than 1% value obtained here.

3.5.5 Sources of errors and requirements on the apparatus

These results show the feasibility of a measurement of g with a precision of 1% and set the requirements on the apparatus

- the antihydrogen production and beam formation mechanisms must provide a beam with at minimum one useful antihydrogen atom per second;
- The beam radial velocity sets the requirement on the grating and detector size and limits the distance between the gratings. A reduction of the radial velocity allows an increase in the precision of the measurement by increasing L and/or allowing the use of slower antiatoms.
- the antiatoms should not decay during their travel through the gratings, otherwise the velocity recoil following the photon emission masks the effect of gravity; the ideal situation would be to have them in the fundamental state once they have entered the deflectometer.
- A position sensitive detector with a resolution of 10-13 μm is needed.

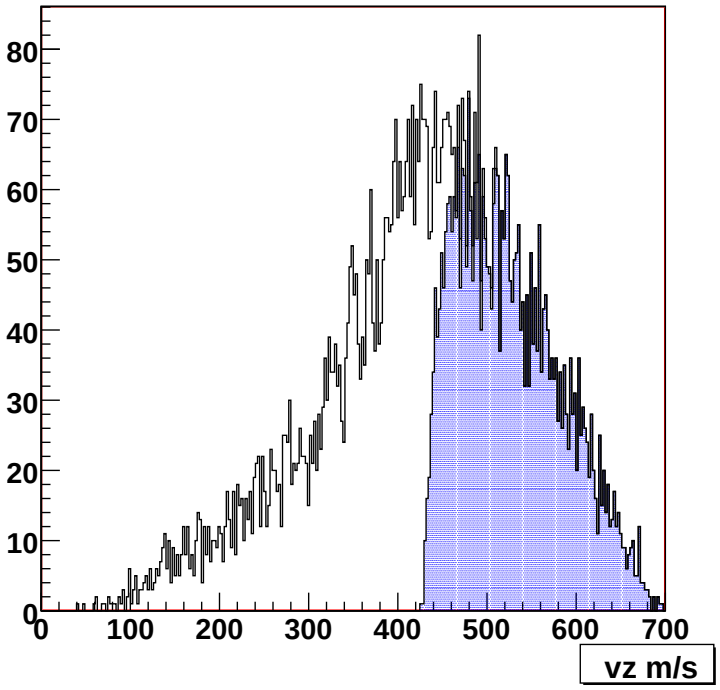

Figure 3.13: The black plot shows the distribution of the horizontal velocity of the antihydrogen atoms reaching the detector. The atoms are launched with horizontal velocity distributed as Fig. 3.3 and a radial velocity corresponding to a Maxwell distribution at 100 mK. Some of the slowest atoms do not reach the detector whose radius is 20 cm. The shaded region is the horizontal velocity (m/s) distribution of the antiatoms having a time-of-flight corresponding to the shaded area of Fig. 3.11. These atoms have a distribution of the squared flight time between the gratings which is symmetric around its mean value and they can be grouped together to obtain the phase shift.

- The gratings must be aligned with a precision of the order of a fraction of the grating period. This alignment must be maintained for a long time (several days or weeks). We are planning to use a laser light to continuously check the grating alignment and if needed correct for misalignments.
- Gravity must be the only force acting on the antiatoms during their flight. Magnetic field gradients are particularly dangerous. If μ_z is the z component of the magnetic moment, the force due to a magnetic field gradient assumed to be along the z-direction is:

$$F_z = -\mu_z \frac{dB_z}{dz} \tag{3.14}$$

Using $\mu_z = \mu_0(m_l + 2m_s)$ where $\mu_0 = 0.927 \times 10^{-23}$ J/T, we can calculate the magnetic field gradient necessary to create a force F_z equal to the antihydrogen weight $mg = 1.64 \times 10^{-26}$ N:

$$\frac{dB_z}{dz} = \frac{mg}{\mu_0(m_l + 2m_s)} = \frac{1.77 \times 10^{-3}}{(m_l + 2m_s)} \text{ T/m} \tag{3.15}$$

If we aim to make a measurement of g with an accuracy of 1%, we must reduce the magnetic field gradients to

$$\frac{dB_z}{dz} < 1.77 \times 10^{-1} \frac{1}{(m_l + 2m_s)} \text{ Gauss/m} \tag{3.16}$$

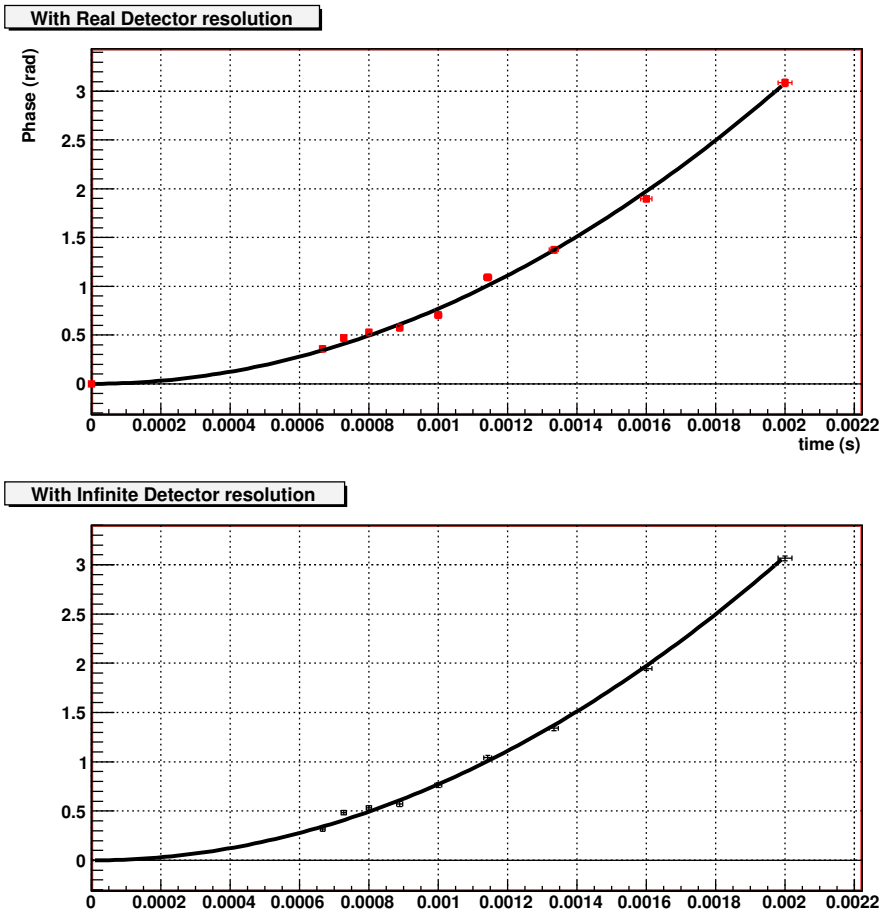

Figure 3.14: Phase shift as a function of the time-of-flight $\sqrt{< T^2 >}(sec)$ between the two gratings of the Moiré interferometer. Top plot: assuming a $10\mu m$ detector resolution; Bottom plot: assuming perfect detector resolution.

A proper magnetic shielding has to be designed around the grating system. Again, atoms in the fundamental state are preferred over Rydberg states with high m.

- Systematic errors can be controlled by comparison of the gravity induced shift with that obtained when taking data with the gratings rotated by 90^0 degrees. In this case the effect of gravity is canceled.
- The design of the deflectometer can still be optimized: it is possible that having the same opening fraction in the two gratings is not the optimum solution.
- to cross-check our results, we are evaluating the possibility of carrying out the charge symmetric experiment (producing hydrogen atoms, rather than antihydrogen atoms, by using protons, rather than antiprotons), but this requires enhancing the position sensitive detector with a scheme that can ionize ground state Hydrogen atoms.

3.6 Additional measurements with the antihydrogen beam

The availability of a beam of antihydrogen offers the possibility to perform additional measurements aiming to study antihydrogen properties. We simply mention here the possibility to perform Rydberg

spectroscopy. A flux of antihydrogen Rydberg atoms is created at the output of the Stark transport scheme. One possibility is just to wait for the decay of the Rydberg atoms and to perform the $2s \rightarrow nd$ spectroscopy using field ionization detection techniques. With Rydberg levels $n \sim 30$ the two photon Doppler free excitation $2s \rightarrow nd$ can be achieved using a stabilized powerful Ti:Sa laser. The accuracy of the laser frequencies at the required wavelengths (two photons at 720nm) can easily reach the 10 KHz level (Syrah laser), leading to a contribution to the relative error of $\Delta\nu/\nu \sim 10^{-12}$. The main contribution to the accuracy will come from the presence of stray electric fields $\simeq 10$ mV/cm that may lower the accuracy by a few orders of magnitude. Without any particular care in compensating stray electric fields we estimate that an accuracy of the order of 10^{-7} could be reached.

A rough evaluation of the measurement time is performed, assuming an antihydrogen beam with a few atoms/sec and a diameter of the order of 1 cm. Due to the mechanism of acceleration of the antihydrogen atoms, more than one antiatom will not be present in the laser interaction region at the same time. In order to address all the atoms with a laser we need to use a CW laser. The laser needs to cross the whole atomic flux. Consequently we will have to focus the laser on the 1 cm beam diameter; the interaction time is 20 μs (corresponding to a beam velocity of 500 m/s). For a 1 Watt laser, a Rabi oscillation frequency slightly smaller than 1 MHz is possible for pure nd states, leading to a one percent transfer of a given n state. Using the field ionization technique it is possible to ionize the atom states selectively and the detection of the resulting charged antiparticles is very efficient.

A time of the order of several days might be enough to reach the $\Delta\nu/\nu \approx 10^{-7}$ region. However using frequency comb techniques, a careful control of the stray electromagnetic fields and detailed analysis of the line-shape, might lead to spectroscopic measurements within the $\Delta\nu/\nu \approx 10^{-9} - 10^{-10}$ region but a longer measurement time will certainly be necessary. Note that it is possible to drive transitions insensitive (to the first order in perturbation theory) to electric fields (k=0 states).

Chapter 4

Antihydrogen production by charge exchange

The production of antihydrogen in AEGIS is based on the charge exchange reaction between antiprotons and Rydberg positronium

$$Ps^* + \overline{p} \rightarrow \overline{H}^* + e^- \tag{4.1}$$

The use of this reaction was proposed some time ago [150] and recently demonstrated by the ATRAP collaboration [91]. The method by which the antihydrogen production will be implemented in AEGIS however significantly differs from that of ATRAP.

Charge exchange reactions between Rydberg atoms and ions are largely studied in atomic physics: we only recall here the main physical features of this process.

The main reasons that make this reaction interesting for the AEGIS design are

- the large cross section which is of the order of $a_0 n^4$ where $a_0 = 0.05$ nm is the Bohr radius and n is the principal quantum number of the Ps;
- the expected distribution of the quantum states of the produced antihydrogen. The antiatoms are produced in Rydberg states with a predictable state population strictly related to that of the incoming positronium. The range of final quantum states is reasonably narrow. Thanks to the sensitivity to electric field gradients of these Rydberg atoms a beam can be formed by accelerating the atoms with a time dependent inhomogeneous electric field.
- the possibility to experimentally implement the reaction in such a way that very cold antihydrogen can be produced. To maximize the efficiency in the use of the antihydrogen and the quality of the beam it is in fact important that the transverse velocity be as low as possible.

In order to best understand the formation process under the experimental conditions of AEGIS, and in order to optimize the production rate of useful antihydrogen atoms, we have implemented a complete calculation of the charge exchange process using a classical trajectories Monte Carlo (section 4.2).

4.1 Kinematics

The conservation of energy and momentum in the charge exchange reaction sets the constraints on the minimum energy of the resulting antihydrogen. Figure 4.1 defines the coordinate system: we call $x_{\overline{p}}$ the direction of the antiproton velocity before the recombination; θ_{Ps} the angle between the positronium and antiproton velocity and θ_H the angle formed by the emerging antihydrogen velocity and the $x_{\overline{p}}$ axis. After some calculations it is straightforward to find that the antihydrogen velocity v_H^2 in the laboratory reference satisfies

$$v_{\overline{H}}^2 + v_{\overline{p}}^2 + 2\left(\frac{m_{e+}}{m_{\overline{p}}}\right)^2 v_{Ps}^2 - 4\frac{m_{e+}}{m_{\overline{p}}} v_{\overline{H}} v_{Ps} cos(\theta_{\overline{H}} - \theta_{Ps}) - 2v_{\overline{p}} v_{Ps} cos(\theta_{Ps}) - 2\frac{m_{e+}}{m_{\overline{p}}}\frac{Q}{m_{\overline{p}}} = 0 \tag{4.2}$$

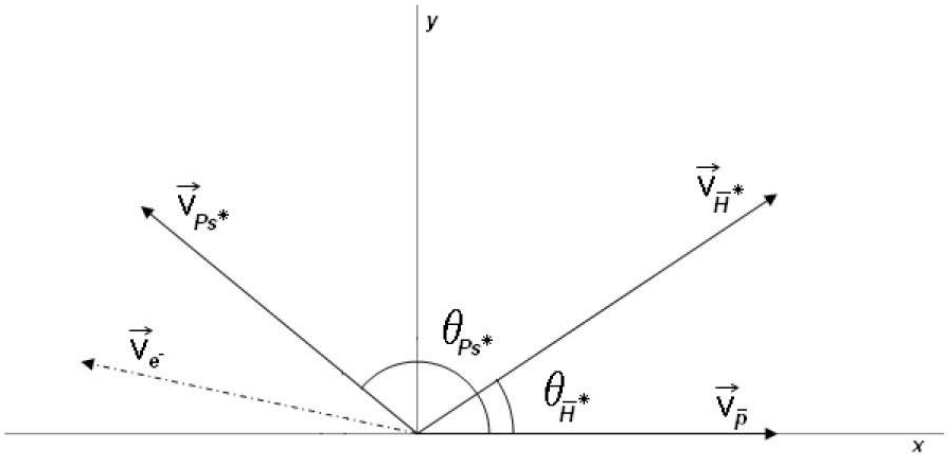

Figure 4.1: Kinematic variables in the charge exchange process

where Q is the difference between the binding energy of the antihydrogen and that of Ps^*

$$Q = R\left(\frac{1}{2n^2_{\overline{H}^*}} - \frac{1}{4n^2_{Ps^*}}\right) \tag{4.3}$$

$R = 27.2\ eV$ is the Rydberg constant. It follows that even assuming that both the antiproton and the positron recombine at rest the resulting antihydrogen velocity is zero only if $n^*_{\overline{H}} = \sqrt{2}n^*_{Ps}$. We will see in the following that this is the most probable value of the quantum number of the antihydrogen but states having n values differing from this by some units are also populated with high probability. In that case the contribution to the antihydrogen velocity is about $15-20$ m/s if $n^*_{Ps} = 20$ and a few m/s if $n^*_{Ps} = 30$. For low n positronium this contribution is not completely negligible.

An additional contribution of the order $v_{\overline{H}} \simeq \sqrt{2}\frac{m_{e+}}{m_{\overline{p}}}v_{Ps}$ comes from the Ps^* velocity. The next section shows that in our experimental conditions the maximum of the cross section is obtained with a velocity of positronium of the order of some 10^4 m/s, resulting in a contribution to the antihydrogen velocity of the order of $15 - 20$ m/s.

The main contribution comes of course from the initial antiproton velocity. AEGIS is designed to prepare antiprotons with a thermal distribution of 100 mK (that is with a mean velocity of 41 m/s) and, by combining all the previous factors, the resulting antihydrogen atoms should then be produced with a velocity of a few tens of m/s.

4.2 CTMC modeling of the charge exchange reaction

A quantum calculation is necessary to obtain the cross section when the positronium is in a low-n state [71], while for an high-n state of positronium, a CTMC approach (Classical Trajectories Monte Carlo) can be used. Following [72] [73] we have implemented a CTMC modeling of the charge exchange that gives important results about the cross sections and the final state distributions. The range of quantum

state of interest to us does not completely match that used in [72], [73]. Similar results are reported in [77], [74]. The interaction between Rydberg positronium and an anti-proton can be described (in absence of any magnetic field) by a simple three-body Hamiltonian:

$$H = \frac{1}{2}(\vec{p}_1)^2 + \frac{1}{2}(\vec{p}_2)^2 + \frac{1}{2m_3}(\vec{p}_3)^2 - \frac{1}{\|\vec{r}_1 - \vec{r}_2\|} + \frac{1}{\|\vec{r}_1 - \vec{r}_3\|} - \frac{1}{\|\vec{r}_2 - \vec{r}_3\|} \tag{4.4}$$

$\vec{p}_i$ and $\vec{r}_i$ are the momenta and coordinates of particles; the index 1 and 2 referring to e^- and e^+, and index 3 referreingto the antiproton.

Once the proper initial conditions are established, the motion of the particles can be calculated using the 18 coupled Newton classical equations of motion:

$$\frac{dp_i}{dt} = -\frac{\partial H}{\partial r_i} \tag{4.5}$$

$$\frac{dr_i}{dt} = \frac{\partial H}{\partial p_i} \tag{4.6}$$

where p_i and r_i are the momenta and the Cartesian coordinates of the particles. For each initial condition a Runge-Kutta method is applied to calculate the trajectories of the electron and positron. Energy is conserved within a part in 10^3 or better.

The initial conditions correspond to Rydberg positronium far away from the antiproton. The choice of the classical initial conditions of the positronium that correctly mimic the quantum state population is the most delicate point of this approach. Following the well established literature [75] [76] the positronium motion is separated into center of mass motion and relative motion. The internal motion is the classical Kepler motion in which a particle with the reduced mass μ describes elliptical paths. The semi-axis parameters of the ellipse are related to the quantum numbers n, l, m.

$$L_c = \sqrt{l(l+1)} \tag{4.7}$$

$$a = \frac{n^2}{\mu} \tag{4.8}$$

$$b = \frac{n \cdot L_c}{\mu} \tag{4.9}$$

where we have introduced the major semi-axis of the ellipse a, the minor semi-axis b and the classical angular momentum L_c. During the simulation a random point in the ellipse is chosen; the plane of the ellipse is randomly oriented in space using Euler's angles and a center of mass speed v_{Ps} is attributed to the positronium. The $\overline{p}$ is placed far along the z-axis with an impact parameter b_p. b_p is randomly distributed between 0 and a value b_{max} chosen in such a way that for $b_p = b_{max}$, the $\overline{H}$ production probability is negligible.

If $\overline{H}$ is produced, the quantum numbers n_H and l_H of the antihydrogen atom are evaluated in a semi-classical way, analyzing the elliptic orbit of e^+ around the $\overline{p}$, with a method completely analogous to that used for determining the Ps initial state.

The cross section for the charge exchange process is evaluated by

$$\sigma_{CE}(n) = \frac{N(\overline{H})}{N_{tot}} \cdot b_{max}^2 \cdot \pi \tag{4.10}$$

where $N(\overline{H})$ is the number of $\overline{H}$ produced, N_{tot} is the total number of simulated interactions.

4.2.1 Cross sections and final state distributions

As expected [77] [78], our calculation reproduce the effect known as velocity matching: the cross section is high when the relative velocity v_r between antiproton and positronium matches the velocity of the Rydberg positronium internal motion v_{orb}. We define k_v

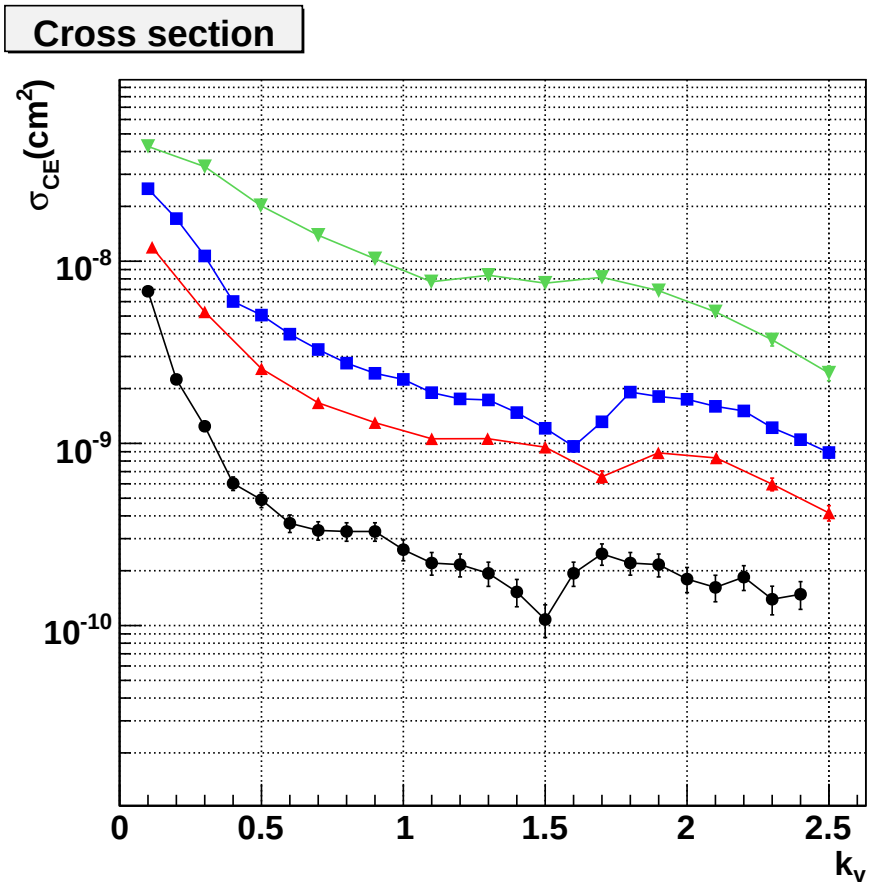

Figure 4.2: In this plot the cross section as a function of k_v for different values of n_{Ps} and $l_{Ps} = 2$ is shown. From top to bottom n_{Ps}=50,35,30,20. The corresponding velocities for $k_v = 1$ are 22 km/s, 31 km/s, 36 km/s, 54km/s

$$k_v = \frac{v_{Ps}}{v_{orb}} \tag{4.11}$$

v_{orb} is the speed of the positron averaged over its orbit for a given value of n_{Ps} and l_{Ps}. For circular orbits

$$v_{orb} = \frac{1}{2}\frac{e^2}{\hbar}\frac{1}{n} \tag{4.12}$$

If k_v is larger than about 3 the cross section is small while for $k_v < 1$ the cross section maintains high values. Of particular interest are the high values of the cross section for low k_v. Because in our case we have very cold antiprotons (100 mK) v_r is in practice the positronium center of mass velocity v_{Ps}. Figure 4.2 plots the cross section for the formation of antihydrogen by charge exchange as a function of k_v for some values of the Ps principal quantum number and $l = 2$.

Note that the absolute values of the cross sections are very high even for an atomic process. The presence of the velocity matching effect sets an important requirement on the positronium production mechanism: the Rydberg positronium leading to antihydrogen formation has to be cold. As a reference the Ps velocities corresponding to $k_v = 1$ for $n_{Ps} = 20, 30, 35, 50$ are 54 km/s, 36 km/s, 31 km/s, 22 km/s. It is important that the positronium velocity does not exceed about twice the value corresponding to $k_v = 1$ but a precise tuning of the center of mass velocity as a function of the quantum number is not needed.

Note that for a thermal distribution $v_{Ps} \simeq 4 \cdot 10^3 \sqrt{T_{Ps}(K)}$ m/s.

Figure 4.3 shows the cross sections obtained with $k_v = 1$ versus the principal quantum number of Ps in two cases: mixed l and fixed l (l=2). Very small differences are found between the two cases. The cross section increases as n^4 if $k_v = 1$.

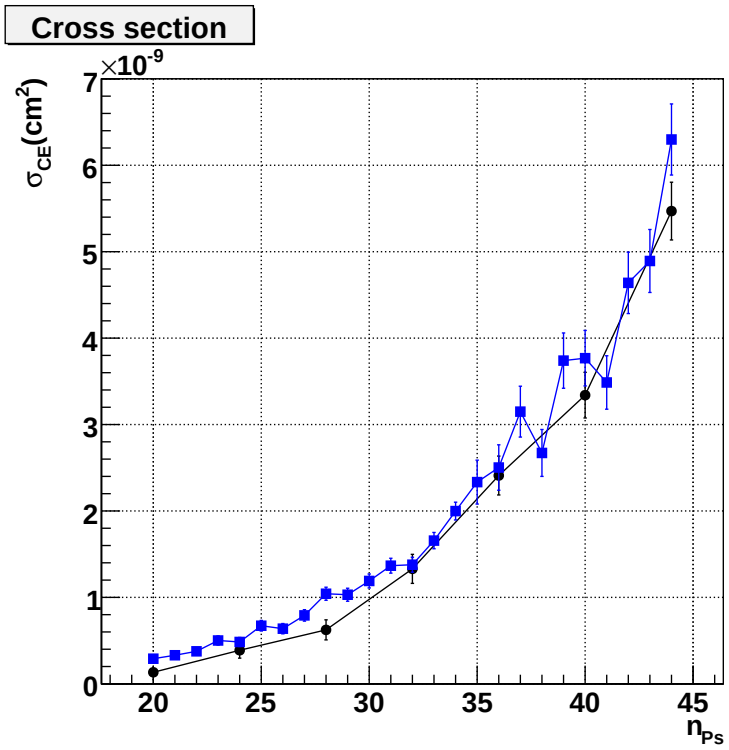

Figure 4.3: Cross section versus the positronium principal quantum number for $k_v = 1$. Squares refer to l_{Ps} randomly chosen between 0 and $n_{Ps} - 1$ while circles correspond to $l_{Ps} = 2$

The distribution of the produced $\overline{H}$ final states has been studied as a function of the positronium initial state.

Rydberg positronium will be produced in AEGIS by laser excitation of ground state positronium with tunable lasers. The n value can be chosen within a wide range $n \simeq 20 - 40$. Regardless of the initial state of the positronium, we always obtain a distribution of final $n_{\overline{H}}$ and $l_{\overline{H}}$. The mean value of the $n_{\overline{H}}$ distribution is linearly related to the principal quantum number n of the Ps (see figure 4.4) and it corresponds to a charge exchange reaction with $Q = 0$ or, in equivalent terms, $n_H = \sqrt{2} n_{Ps}$.

The distributions of the n, l quantum number of the produced antihydrogen obtained with positronium with $n = 35$ and $l = 2$ and $n = 20$ and $l = 2$ are shown in figures 4.5 and 4.6. The figures also show the distribution of the quantum number k used to describe the atoms in electric fields. We recall that $k = n_1 - n_2$ where n_1 and n_2 are the parabolic quantum numbers related to the the spherical quantum number n, l by $n = n_1 + n_2 + |m| + 1$.

The distribution of the principal quantum number n of antihydrogen produced via charge exchange for a number of Ps initial states is shown in figure 4.7.

Figure 4.8 shows the distribution of the velocity of antihydrogen obtained starting from antiprotons with a Maxwell distribution at 100 mK and Rydberg positronium with $n_{Ps} = 35$ and $k_v = 1$.

In the presence of a magnetic field, a reduction of the cross section is expected: for AEGIS, the strength of the magnetic field in the antihydrogen formation region will be 1 T; the resulting reduction factor is expected to be only 30%. Calculations for the final state distributions in a magnetic field are in progress.

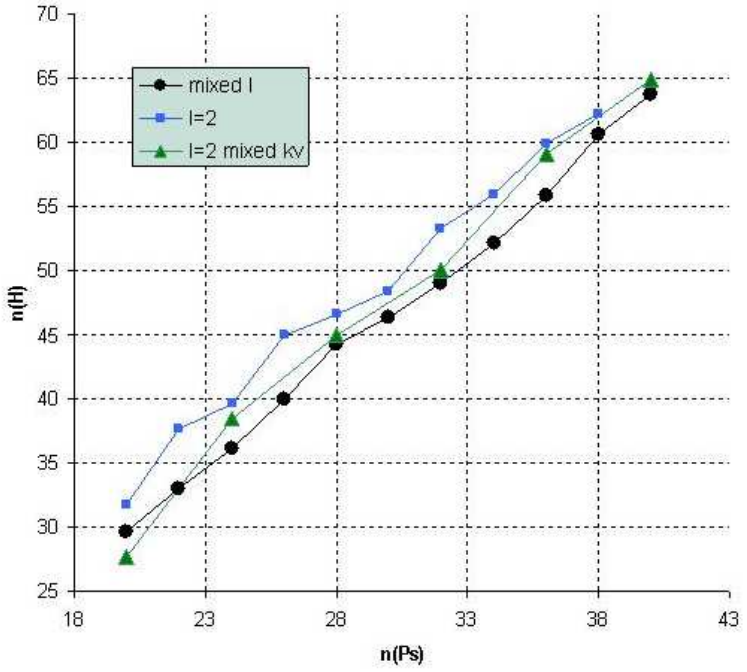

Figure 4.4: Mean value of the principal quantum number $n_{\overline{H}}$ of the produced $\overline{H}$as a function of the initial n_{Ps} state. Different conditions are evaluated:
■ fixed l_{Ps},
• mixed l_{Ps} [0;n-1]
▲ $l_{Ps} = 2$ with different values of kv

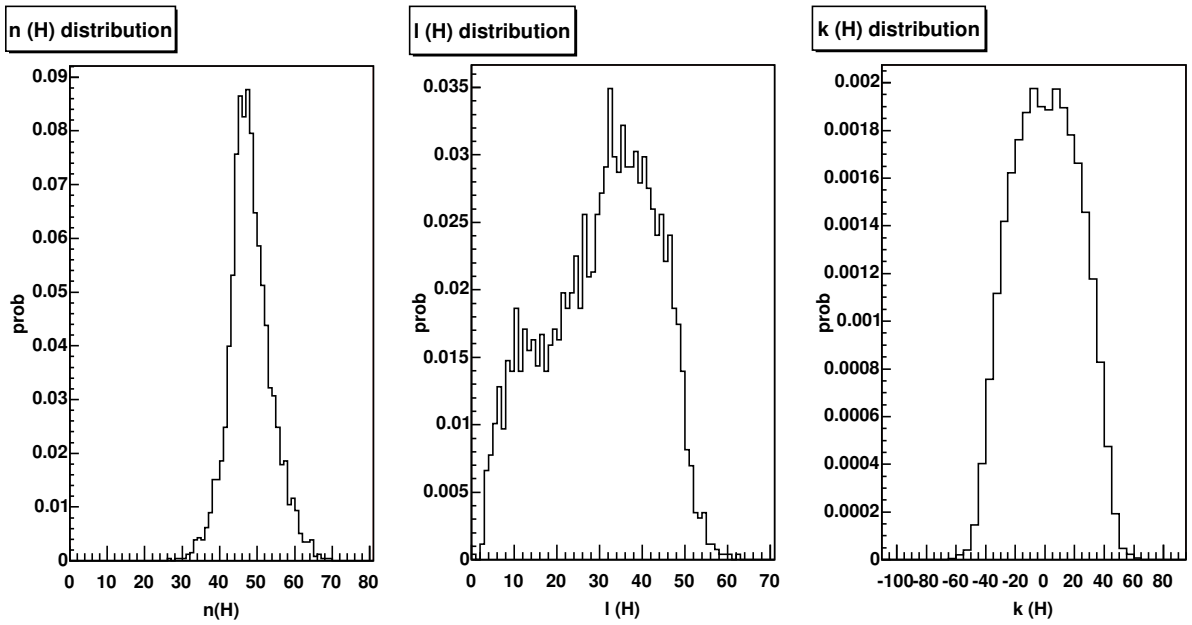

Figure 4.5: Distribution of final states obtained with 3000 anti-hydrogen atoms; from left to right, the three plots show the distribution of $n_{\overline{H}}$, $l_{\overline{H}}$ and $k_{\overline{H}}$. The initial state of the positronium used to simulate the charge exchange process was: $n_{Ps} = 35$ and $l_{Ps} = 2$.

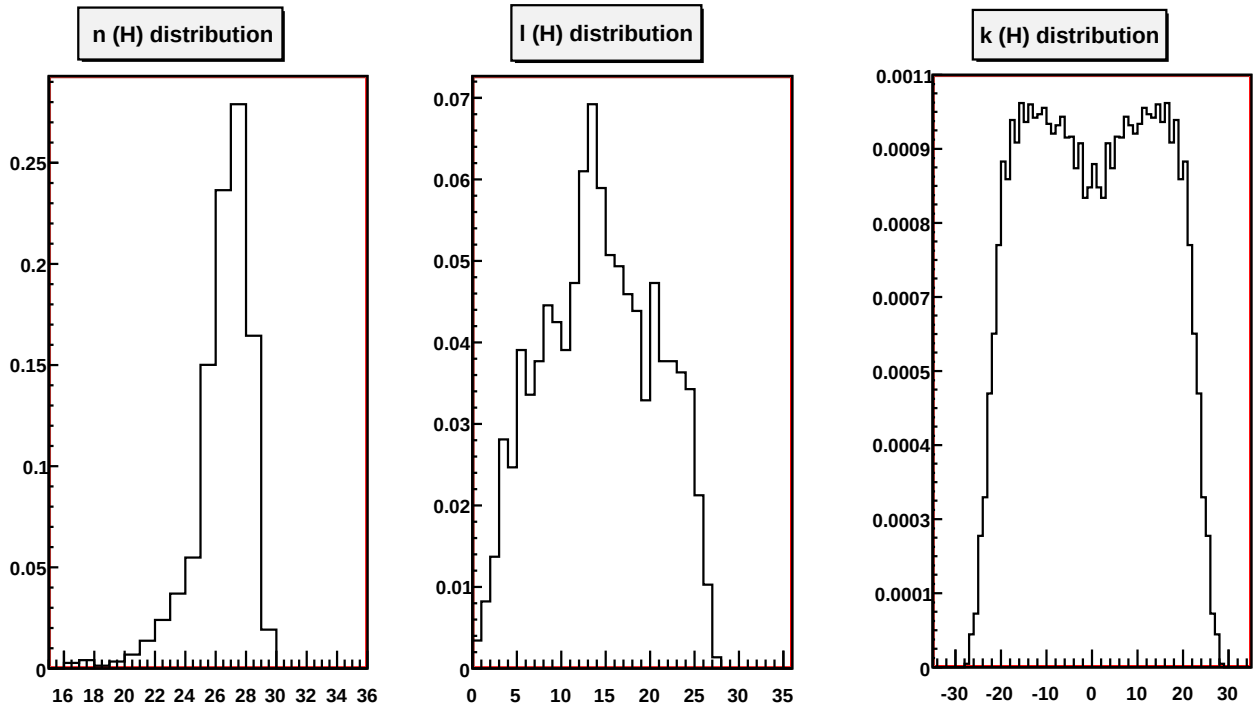

Figure 4.6: Distribution of final states of antihydrogen atoms: from left to right, the plots show the distribution of $n_{\overline{H}}$, $l_{\overline{H}}$ and $k_{\overline{H}}$. The initial state of the positronium used to simulate the charge exchange process was: $n_{Ps} = 20$ and $l_{Ps} = 2$ and $k_v = 1$.

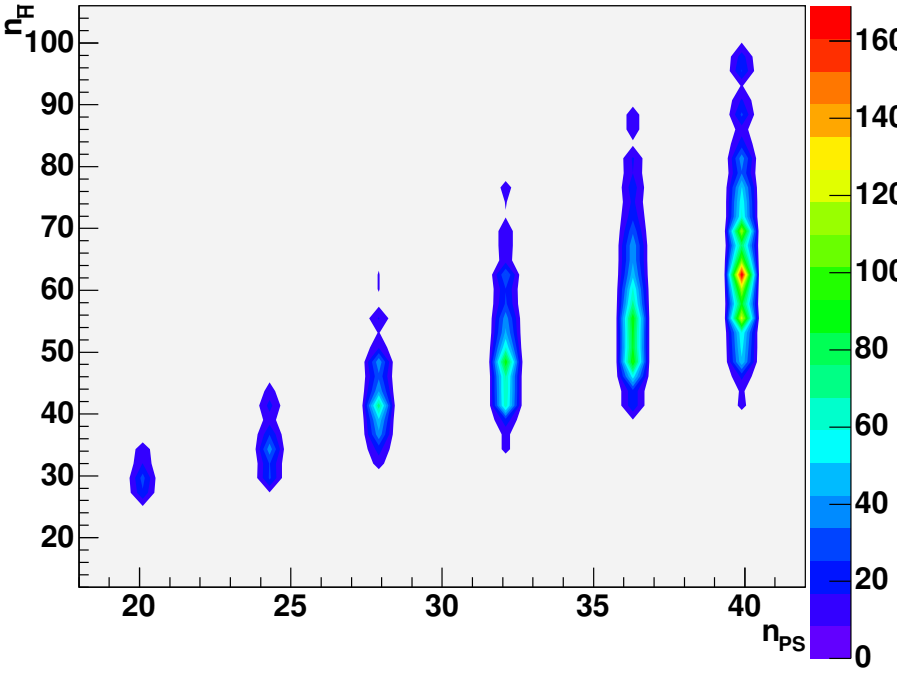

Figure 4.7: Distribution of $n_{\overline{H}}$ as a function of $n_{\overline{P}s}$.

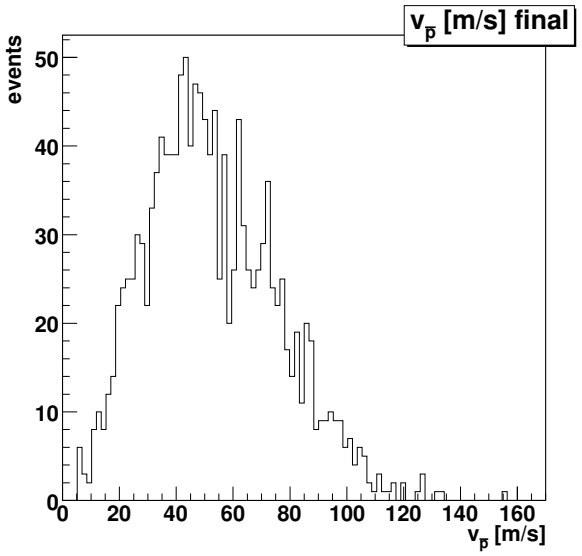

Figure 4.8: Antihydrogen velocity distribution obtained with $100mK$ antiprotons and $n_{Ps} = 35$ with $k_v = 1$

Chapter 5

Acceleration and deceleration of Rydberg atoms

In preparation of this proposal acceleration and deceleration experiments on hydrogen Rydberg atoms have been performed by members of the AEGIS collaboration at ETH Zürich. The results have shown that a Rydberg hydrogen beam with velocity of 700 m/s with quantum number n in the range 15-40 can be stopped in 5 μsec over a distance of 1.8 mm only. The basic principles are described below.

5.1 Forces on dipolar Rydberg atoms

In recent years various techniques with which to control the translational motion of samples of dipolar atoms and molecules in the gas phase have been developed. Of particular relevance to the formation of a $\overline{\mathrm{H}}$ beam in the AEGIS experiment is the Rydberg Stark acceleration/deceleration technique which has been demonstrated experimentally at the University of Oxford for H_2 molecules [82] and at ETH Zürich for argon [83] and atomic hydrogen [84], and has lead to the realization of components with optical analogues such as a Rydberg atom lens [85], a mirror [86] and both two-dimensional [87] and three-dimensional traps.

Property	n-dependence	H(30p)
Binding energy	n^{-2}	15×10^{-3} eV
Energy between adjacent n-states	n^{-3}	1×10^{-3} eV
Orbital radius	n^2	70 nm
Field-free radiative lifetime	n^3	5 μs
Diamagnetic energy shift in a magnetic field of 1 T	n^4	0.1×10^{-3} eV
Classical ionization electric field	n^{-4}	1050 Vcm^{-1}
Inglis-Teller electric field	n^{-5}	70 Vcm^{-1}
Maximum induced electric dipole moment	n^2	1300 Debye

Table 5.1: Scaling of Rydberg state properties with n.

These experiments rely on the force exerted on an electric dipole by an electric field gradient. As presented in Table 5.1, the maximum induced electric dipole moment for a Rydberg state of a given principal quantum number scales with n^2 and at $n = 30$ in atomic hydrogen has a value of ~ 1300 Debye. To first approximation the energy levels of the H atom in an external, homogeneous electric field of magnitude F are given, in atomic units, by

$$E = -\frac{1}{2n^2} + \frac{3}{2}nkF, \tag{5.1}$$

where k is a quantum number already introduced in chapter 4 and which runs from $-(n-1-|m_\ell|)$ to $(n-1-|m_\ell|)$ in steps of two and m_ℓ is the azimuthal quantum number. Here 1 a.u. = 27.211 eV in the case of the energy and 5.14×10^9 Vcm^{-1} for the electric field strength. The manifold of these Rydberg Stark states with principal and azimuthal quantum numbers $n = 30$ and $m_\ell = 0$ in atomic hydrogen is displayed schematically in Figure 5.1 as a function of electric field strength. In this figure the vertical axis indicates the detuning from the zero-field position of the $n = 30$ Rydberg state. The states represented that exhibit the largest dipole moment are the outermost Stark states for which $k = \pm 29$. If one excites an H or $\overline{\text{H}}$ atom to the $k = +29$ state, for example at the point labeled A in Figure 5.1, which is shifted higher in energy by the electric field, and lets the excited atom move out of the electric field, its internal energy will decrease and the atom will accelerate. Similarly if one excites the $k = -29$ state under the same conditions the atom will decelerate as it moves out of the field. The corresponding gain/loss in kinetic energy is equal to $\Delta E = \frac{3}{2} nk\Delta F$ in atomic units.

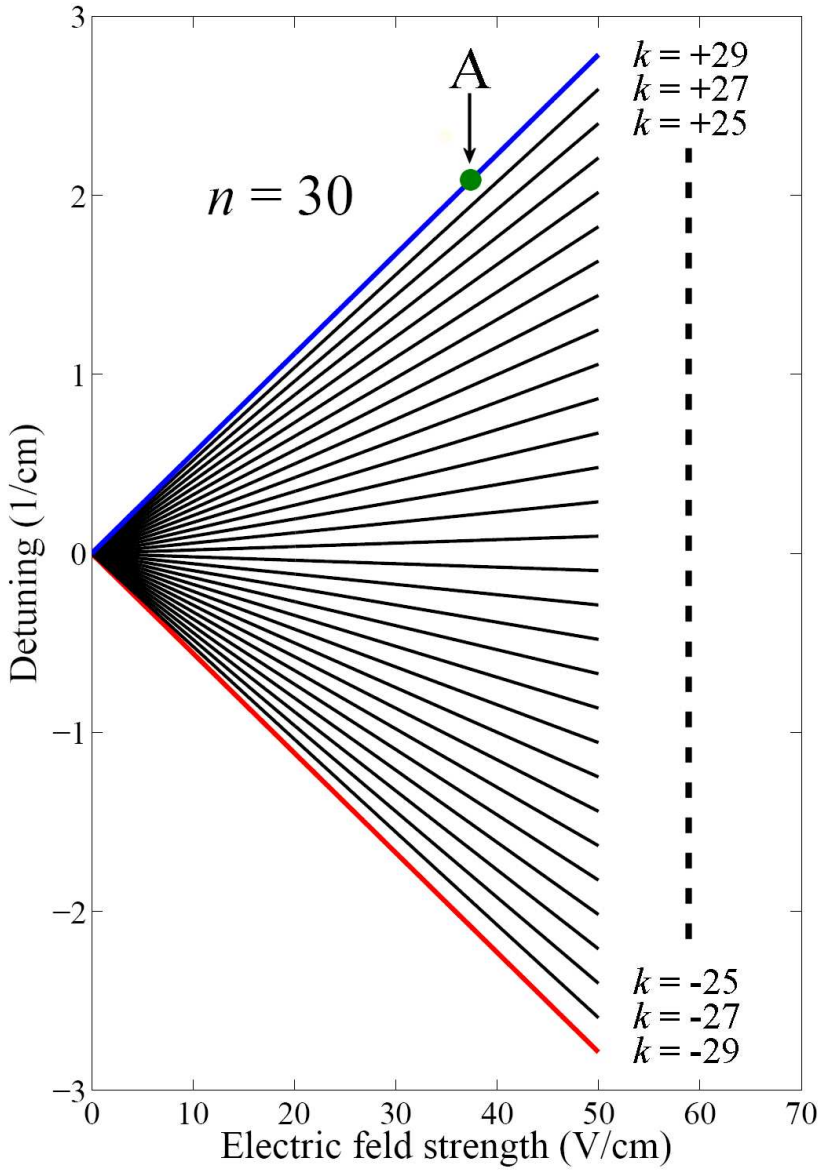

Figure 5.1: Stark structure of the $n = 30, m_\ell = 0$ state of atomic hydrogen as a function of electric field strength. The vertical axis indicates the detuning from the energy position of the field-free Rydberg state in units of inverse centimeters (1 cm^{-1} $\simeq 0.12 \times 10^{-3}$ eV).

This Rydberg Stark acceleration/deceleration technique has been employed experimentally to manipulate a cold cloud of H atoms excited to Rydberg Stark states around $n = 27$ in a two photon excitation via the $2\,^2$P state. Accelerations of up to 2×10^8 ms^{-2} have been achieved in the experiments and the initial kinetic energy of the atoms traveling with an initial velocity of 700 ms^{-1} has been more than quadrupled over a flight distance of only 3 mm in a time of less than 5 μs [84]. Because of the large dipole moments of Rydberg Stark states, fields of only a few kVcm^{-1}, which are easily produced, are required to achieve accelerations of this magnitude.

In the cases of H or $\overline{\text{H}}$ in an homogeneous electric field, the crossings which occur between the positive and negative Stark states associated with adjacent n states when the electric field is increased sufficiently are exact as a result of the spherically symmetric Coulomb potential of the ion core and therefore do not limit the field which may be applied to accelerate the atoms. The electric field at which these states begin to cross is known as the Inglis-Teller field and is given by $F_{\text{IT}} = 1.7 \times 10^9 \cdot n^5$ Vcm^{-1}. However this limitation exists for for non-hydrogenic atoms in pure electric fields and may exist for H or $\overline{\text{H}}$ atoms in combined electric and magnetic fields which are oriented at an arbitrary angle to each other. If these exact crossings become avoided crossings [89] then the useful range of electric fields which may be applied to accelerate/decelerate the atoms is limited. This issue is discussed in next section: here we point out that to obtain the maximum acceleration of the $\overline{\text{H}}$ atoms over a short distance, it will be necessary to apply a time-dependent electric field gradient to accelerate the atoms as was done in the experiments performed at ETH Zürich on Ar [83] and H [84]. This presupposes a pulsed operation of the experiment which is compatible with the pulsed antihydrogen production planned in AEGIS.

5.2 Rydberg Hydrogen deceleration and trapping: experimental results

In order to outline the electrode and electric field requirements for the Stark acceleration of Rydberg $\overline{\text{H}}$, the electrode setup used at ETH Zürich to accelerate/decelerate H and Ar atoms is presented in Figure 5.2. In these experiments the pulsed gas beam, which has a diameter of $\sim$ 1 mm as it passes through the electrodes is excited to a well defined Rydberg Stark state between electrodes 1 and 2, where the electric field has a magnitude of $\sim$ 65 Vcm^{-1}. Following excitation the potentials on electrodes 3 and 4 are switched to $\pm$700 V producing a field between them of $\sim$ 2.3 kVcm^{-1}. This field itself is larger than that required to ionize $n = 27$ Rydberg states, however when it is switched on the atoms are still between electrodes 1 and 2 and experience a significantly smaller field. As the atoms travel forward in the direction indicated by the arrow they decelerate as they move into the increasing electric field, while at the same time the field strength is reduced exponentially as a function of time so as to avoid ionization of the Rydberg atoms.

The electrode setup in Figure 5.2 consists of four polished, rectangular stainless steel blocks which are 20 mm long in the direction perpendicular to the plane pictured. Thus they do not have the cylindrical symmetry about the axis of the antihydrogen beam which is required in the AEGIS experiment. It is therefore proposed that in the AEGIS experiment, the ring electrodes forming the Malmberg-Penning trap which initially confines the anti-protons will be split, so as to produce a field gradient along the common axis of the trap and the superconducting magnet at the time when the $\overline{\text{H}}$ atoms are to be Stark accelerated. In this way, it will be possible to produce an $\overline{\text{H}}$ beam with a mean longitudinal velocity of $\sim$ 1000 ms^{-1} within 1-2 cm of the production volume, while not permitting the atoms to experience an electric field greater than the Inglis-Teller field.

5.3 Rydberg atoms in electric and magnetic fields

The antihydrogen atoms are produced in the AEGIS apparatus inside a Penning-Malmberg trap hosting the cold antiprotons and they will be accelerated by applying electric fields of the type previously described but, and this is the main difference with the reported experiments, in presence of the trap magnetic field. The magnetic field will be uniform in the acceleration region. Under completely general conditions, the dynamics of Rydberg hydrogen atoms in electric and magnetic fields with arbitrary mutual orientation is a rich and complex matter [89]. Several regimes are possible depending on the range of parameters (values

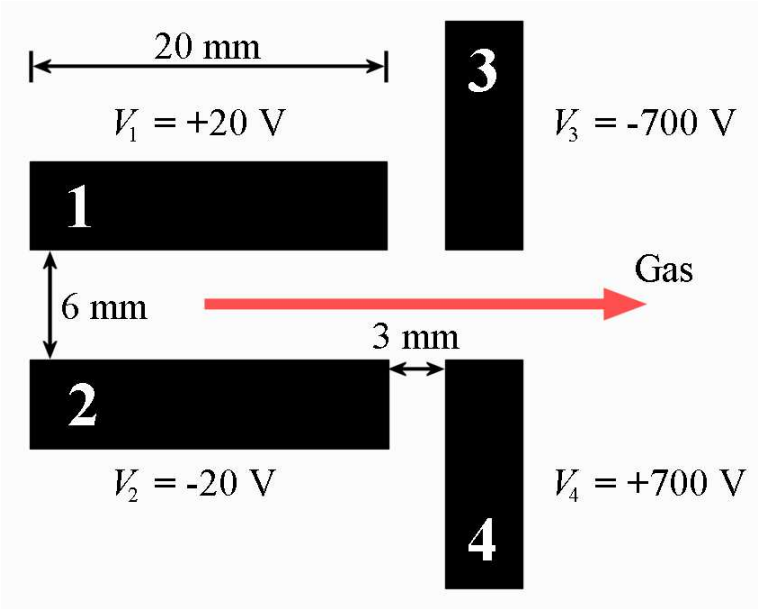

Figure 5.2: Electrode setup and typical potentials used at ETH Zürich to accelerate/decelerate H and Ar atoms in Rydberg states around $n = 27$ [83, 84].

of the electric and magnetic fields, n quantum number value). The magnetic field in the antihydrogen formation region is chosen following a compromise between the requirement of the charged particle trap (that demands high magnetic fields) and the need to softly perturb the Rydberg antihydrogen. The choice of B=1 Tesla realizes this compromise for Rydberg antihydrogen having n not higher than $\simeq 35$. The Hamiltonian of the hydrogen atom in electric and magnetic fields (in atomic units) is

$$H = \frac{p^2}{2} - \frac{1}{r} + \frac{\gamma l_z}{2} + \frac{\gamma^2(x^2+y^2)}{8} + \vec{f}\cdot\vec{r} \tag{5.2}$$

In writing this Hamiltonian we have made the approximation that the center of mass and the relative motion of antiproton and positron can be separated. This is true with good approximation within our typical range of parameters. The magnetic field influences the energy levels with a linear term (Zeeman effect) and a quadratic one (diamagnetic effect). Without any electric field the linear term shifts the unperturbed energy levels with given quantum numbers n, l by an amount proportional to m. n, l, m are still good quantum numbers but the the energy levels are no more degenerate: $E_n = -\frac{1}{n^2} + \frac{mB}{2} + ...$

The second order diamagnetic interaction mixes the l states and the energy shift is roughly proportional to $\gamma^2 n^4$. For $B = 1$ T and $n = 30$ the diamagnetic term is still smaller than the Zeeman term but it is not completely negligible.

When the diamagnetic term has to be included in the energy calculation, but the shift induced by it is smaller than the unperturbed energy level spacing, then n can still be considered a good quantum number (weak field). This condition can be written as

$$\gamma^2 n^7 < 1 \tag{5.3}$$

Our regime will be that of a weak magnetic field with a diamagnetic term smaller than the Zeeman term.

If 5.3 is not satisfied then several levels with different n are mixed; it also possible to reach a regime in which the force due to the Coulomb field is smaller than the magnetic force (strongly magnetized Rydberg atoms and guiding center atoms).

The energy levels in presence of electric and magnetic fields with arbitrary mutual orientation have been calculated by first and second order perturbation and by exact diagonalization of the Hamiltonian in a complete basis set [89] The interesting point is that the classical dynamics could become chaotic and the corresponding quantum behavior is the presence of large avoided crossings between adjacent levels.

This fact could influence and eventually limit the acceleration of the Rydberg atoms induced by a given electric field in presence of a magnetic field. According to [89] the chaotic regime is likely to appear when the angle between the magnetic and electric fields is in the interval $40^0 - 70^0$ and if the parameters $n^3\gamma$ and $n^4 f$ are close to (but less) than 1. The electric field of the Rydberg accelerator will be mostly perpendicular to the magnetic field and we will choose field values in order to have $n^3\gamma, n^4 f < 1$ avoiding the chaotic regime.
Quantum calculations with our parameters will be very useful to drive the experimental choices. Experimental tests with hydrogen are planned at ETH [90].

Chapter 6

Positronium formation

Positronium will be obtained in AEGIS by sending a bunch of positrons on a suitable target acting as positronium converter with high efficiency. Rydberg positronium will then be formed by two step laser excitation of the resulting cloud of ground state ortho-positronium. As already discussed in chapter 4, the velocity of the Rydberg positronium must be of the order of some 10^4 m/s corresponding to a kinetic energy of about 10 meV. We will refer to this as cold positronium.

We recall here the current knowledge regarding the mechanisms of conversion of e^+ into Ps, the relevant material properties and the tests in progress inside the AEGIS collaboration to select the proper positron converter.

The important parameters that have to be be optimized, and that are somewhat linked to each other, are the choice of the target material, the yield of positronium emitted and its velocity distribution. The AEGIS design is focused on positronium emitted in reflection geometry, that is on positronium emitted from the same side of the target where positrons are injected. It is important to underline that in the AEGIS apparatus the converter target will be mounted in a cryogenic environment with temperature of $\sim$ 100 mK.

6.1 Mechanisms of positronium formation and material properties

Positronium in vacuum is normally produced by implanting positrons with a kinetic energy of the order of several hundred eV or few keV into a solid target (converter). Slowing down at thermal energies occurs rapidly in comparison with annihilation. Thermal or epithermal positrons can be re-emitted into the vacuum as positronium atoms after capture of an electron. The $Ps/e+$ yield and the energy distribution of the emitted Ps depend on the nature of the converter material, and, for a specific material, on the implantation depth and on the temperature of the target.

Ground state positronium is formed with equal likelihood in the singlet state (para-Ps with spin 0) or in one of the three triplet states (ortho-Ps with spin 1). The self-annihilation lifetime of para-Ps is short, 125 ps, and it mainly occurs with the emission of two γ with 511 keV. Ortho-Ps in vacuum is required to annihilate at least into 3 γ with a total energy of 2×511 keV and this process has a longer characteristic lifetime of 142 ns. We are interested only in the fraction of positronium emitted as o-Ps, since the lifetime of p-Ps is too short to allow its laser excitation before its decay. As a reference, positronium emitted from the converter material with a velocity of $\simeq 5 \cdot 10^4$ m/s needs a few tens of ns to reach a distance from the surface of the order of a few mm where the laser excitation can easily take place.

In a magnetic field the triplet state with spin component $S_z = 0$ is mixed with the singlet state, resulting in a reduction of the self annihilation lifetime. The lifetime in a 1 T magnetic field is reduced to about $15ns$ while about $45ns$ are expected in a $0.5T$ field [92]. On the contrary the lifetime of the triplet states with $S_z = \pm 1$ are not affected by the magnetic field, therefore the maximum expected yield reduction in a magnetic field of 1 T is 1/3 of the o-Ps fraction.

Positronium production occurs in metals and semiconductors as well as in insulator materials but the production mechanisms are somewhat different.

In metal and semiconductors, positronium formation is only a surface process originating from positron back-diffusion to the surface followed by electron capture. Thermalized positrons can produce positronium by an adiabatic charge transfer reaction at any temperature, provided that the positronium formation potential W is negative

$$W = \Phi_- + \Phi_+ - 6.8eV < 0 \tag{6.1}$$

6.8 eV is the Ps ground state binding energy and Φ_- and Φ_+ are, respectively, the work functions of the electron and of the positron for the converter material. In this case, positronium leaves the surface with an energy distribution extending from zero up to the work-function energy, resulting in a mean energy of the order of eV [98]. If $W > 0$ adiabatic emission is scarce and it is essentially due to epithermal positrons. When also $\Phi_+ < 0$ the process of direct positron emission is in competition with the adiabatic emission. Figure 6.1 shows the Ps formation potentials. Elements for which Ps formation is unfavorable ($W > 0$) are barred in red; blue bars show the elements for which there is a competition between positronium formation and bare positron emission ($W < 0$, $\Phi_+ < 0$).

In addition to adiabatic emission, thermally activated formation has been observed. This additional process is dominant when the target temperature is of the order of several hundred kelvin and it is interpreted in terms of surface traps in which the positrons reside but from which they may be desorbed as positronium [93]. In this case positronium has an energy distribution corresponding to the target temperature. As a reference for $Ag(100)$ the measured Ps yield is around 30% for a target temperature in the range $300-500$ K (adiabatic contribution) and it increases up to 100% when the target temperature is raised up to about 1100 K [95]. Another example is that of Ge, where the high temperature limit is very near to 100% with an adiabatic contribution of less than 1% [94].

In insulators surface formation of positronium by thermal positrons is unlikely since the binding energy of the positronium atom is normally insufficient to compensate for the extraction of the positron and of the electron ($W > 0$). However the thermalisation of positrons in an insulator is less efficient than in a metal, thus a larger flux of positrons returning to the surface of the insulator with sufficient kinetic energy to form positronium can be expected. This process is known to occur in Al_2O_3 and MgO (maximum conversion yield in the low implantation energy limit of 28% and 24% respectively). The energy spectrum in this case reflects the energy distribution of the epithermal positrons and may extend up to several eV.

In addition positronium can be formed in the bulk, it can reach the surface and then be emitted into the vacuum. Ps is formed during the slowing down of e^+ , mostly when the e^+ energy is in the interval between $E_{gap} - E_{solid}$ and E_{gap} (the so-called Ore gap). E_{gap} is the energy necessary to excite an electron of the insulator from the valence to the conduction band and E_{solid} is is the binding energy of the e^+e^- system in the solid. In general $E_{solid} < 6.8eV$. Bulk positronium formation is also possible when a positron encounters a spur electron, i. e. an electron raised in the conduction band by the positron itself during its slowing down. A bound e^+e^- pair is a mobile system, as long as it is not trapped by a defect or self-trapped in a phonon cloud; it will eventually reach the surface with a residual kinetic energy E_{CM} that depends on the depth of formation. Bulk formation of Ps is known to be the only important channel for Ps emission in ice and ionic crystals (conversion yields of $30 - 40\%$) and to be the dominant one in SiO_2 (conversion yield of 72%, in addition to another 12% coming from surface formation). The positronium energy spectra observed for the above materials extend over a few eV and, for shallow implantation, reflect incomplete Ps thermalisation prior to emission.

The two alternatives described above (surface or bulk formation) depend on the temperature of the sample only indirectly, through temperature effects on migration and trapping. Thus the e^+Ps conversion yield may be expected to stay high even at cryogenic temperatures.

6.2 Ps formation in porous materials

Positronium formation in porous materials is specially interesting [99]. A material can have pores not connected to the surface or a network of pores (ordered or not ordered) connected to the surface. Positronium formed in the bulk can diffuse into a pore or it can be formed at the surface of the pore. If the pores are connected to the surface of the material then the positronium can escape toward the vacuum following the pore channels and colliding with the pore walls. The energy spectrum of the emitted positronium

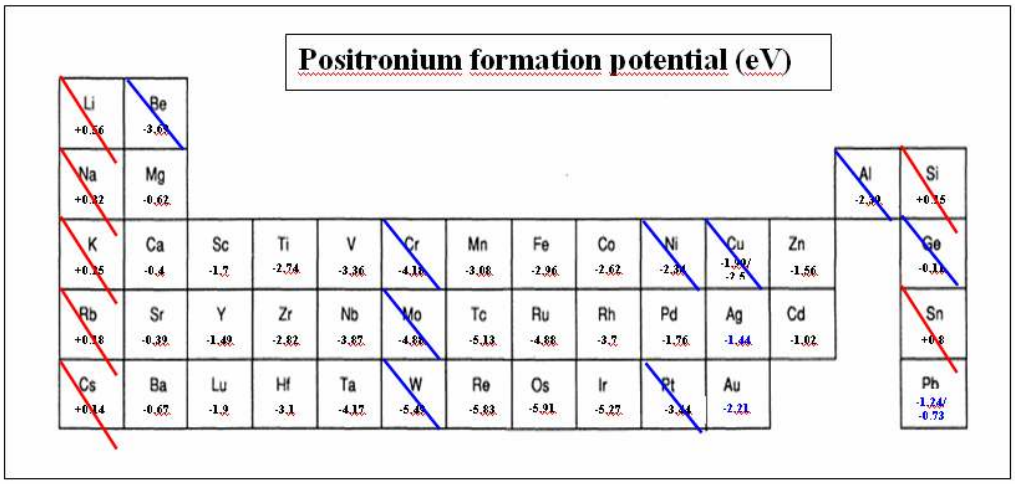

Figure 6.1: Positronium formation potential W for various materials. Favorable materials for Ps formation are the ones with $W < 0$

depends on the energy of the positronium entering the pore, on the number of collisions with a pore surface and on the mean energy loss for each collision. The depth in the bulk where positronium is formed depends on the e^+ energy and with an appropriate design of the pore geometry and by controlling the implantation depth through the positron implantation energy, we expect to be able to tailor the energy spectrum of the emitted positronium to match the required values.

Figure 6.2 shows schematically the mechanism of positronium production and cooling in porous materials.

The described cooling of Ps by collisions has been observed for Ps formed in silica-powdered grains or silica aerogel [96] and the results are quite consistent with theoretical models.

Assuming that the initial energy of the Ps atom is already below the band gap of the solid, the cooling process occurs only by elastic collisions with the atoms at the surface of the solid. The maximum energy transfer ΔE in a single collision of a Ps atoms (with mass =2 m_e) and an object of effective mass M_{eff} can be estimated by [96]:

$$\frac{\Delta E}{E} \simeq \frac{8}{2 + M_{eff}/m_e} \simeq \frac{8m_e}{M_eff} \tag{6.2}$$

where M_{eff} coincides with the mass M of the single atom of the solid only when the Ps energy is higher that a few hundred meV; otherwise is lower and it can be approximated by $M_{eff} = nM$ where

$$n = \frac{{\lambda_{DB}}^2}{r_a^2} \tag{6.3}$$

with λ_{DB} being the DeBroglie wavelength of Ps and r_a the typical inter-atomic distance.

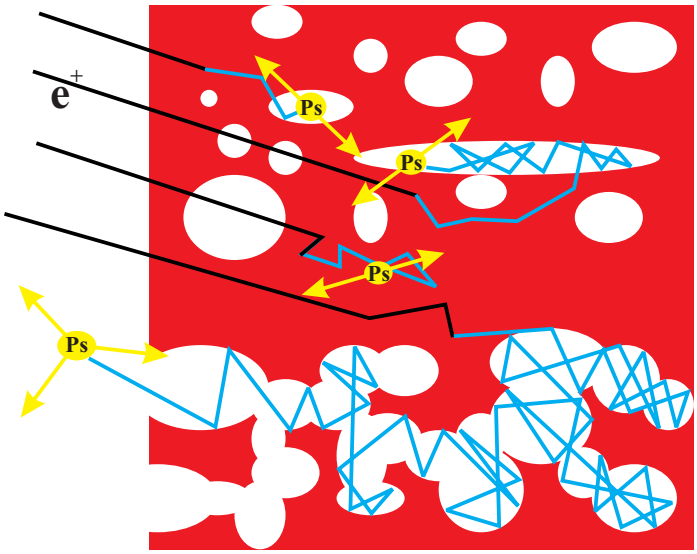

Figure 6.2: Ps formation in porous films, from [99].

Average values of $\frac{\Delta E}{E} \simeq 1 - 4 \cdot 10^{-4}$ are expected. Thus, cooling a Ps atom from an initial energy of about $1eV$ down to some meV requires about 10^4 collisions. Annihilation by pick-off with the pore walls cannot be avoided but the total pick-off loss is expected to remain at the tolerable level of $60 - 70\%$.

In addition the pores must be suitably designed to keep the positronium travel time well below the 142 ns lifetime. A simple stochastic approximation for the random walk of a positronium atom bouncing against the walls of the pore and diffusing toward the open end, links the number n_c of collisions to the aspect ratio of the pore (ratio between the length L and the diameter d)

$$L = d\sqrt{n_c} \tag{6.4}$$

Within the same approximation, the travel time t is related to the diameter of the pore and to the average speed v of Ps by

$$t = n_c \frac{d\sqrt{2}}{v} \tag{6.5}$$

If we assume $t \simeq 140ns/10$, $v = 4 \cdot 10^4$ m/s, $n_c = 10^4$ we obtain reasonable results: $d \simeq 40$ nm and $L \simeq 4\mu m$. Of course, these numbers are to be taken only as a first orientation on the selection of possible converters among structures that are commercially available or that can be produced with a reasonable effort.

The use of a metallic converter would certainly be more efficient from the point of view of cooling, since a single collision of a positronium atom with a free electron at the surface of the metal can produce a fractional energy loss of 50% thereby reducing the number of necessary collisions to less than about 100. However pick-off annihilation losses in a metal are expected to strongly reduce the flux of Ps emerging from the channels.

Nevertheless, the lack of experimental data on this subject suggests that one should not abandon a priori any attempt to use a metallic converter.

Available experimental data on low temperature Ps formation are scarce. One of the first experiments on cold Ps formation in SiO_2 powder with the TOF (Time Of Flight) technique to measure the Ps velocity, has been performed by A. Mills, Jr. in 1989 [97]. For a 19 keV positron implantation energy about 2% of Ps were found to be thermalized at 4.2 K. It was concluded that longer contact of Ps with the powder would provide better thermalization. The formation of Ps in porous films at room temperature studied with the TOF method has been reported in ref. [106]. Clean Ps emission peaks in TOF spectra have been observed. The measurements support the assumption that the Ps velocity is strongly dependent on the converter film's properties, such as degree of porosity and level of pore interconnectivity.

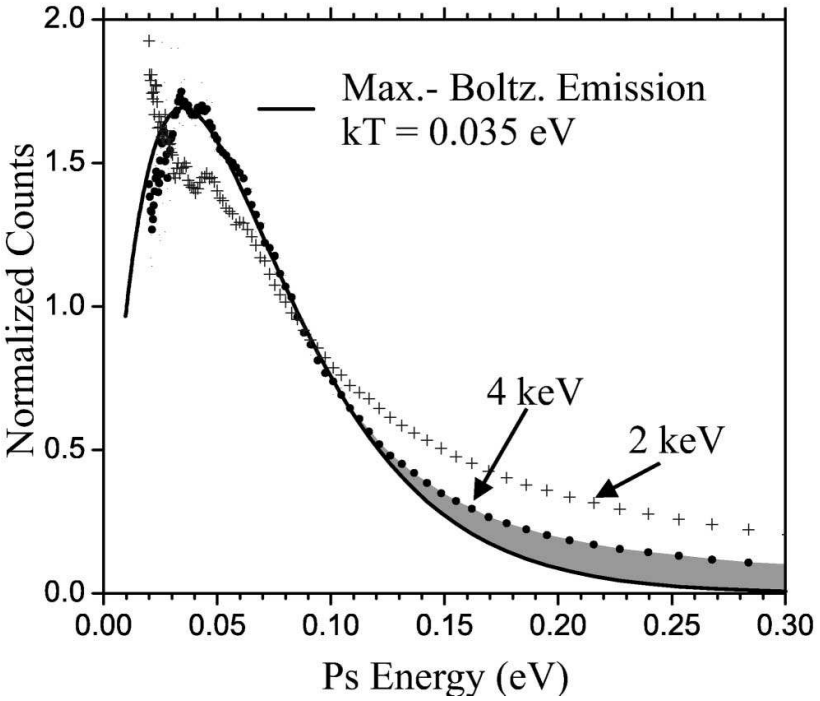

Figure 6.3: Ps energy spectra from typical porous silica film at 300 K [104].

Recently, Fischer [107] investigated the formation of Ps in porous films from 400 to 50 K. Copious amounts of Ps atoms, up to 30% per implanted positron, have been observed at 50 K. This amount was found to increase even further down to 10 K, thus making these films a promising target for cold Ps formation. Authors use the so-called, $3\gamma/2\gamma$-ratio method for measurements of the Ps yield. This makes it difficult to extract information on the fraction of Ps emitted in vacuum from the film and in particular on the Ps atom's velocity distribution.

Experimental evidence of high yield emission of thermalized positronium from a porous silica target kept at room temperature has been obtained in an experiment attempting precision measurements of the vacuum decay rate of the triplet Ps [104].

Figure 6.3 (from [104]) shows the energy distribution of Ps emitted from the porous silica film. The number of thermalized Ps obtained per positron in this experiment was about 0.3-0.33.

As shown in Figure 6.3, higher energy positrons implanted more deeply into the film and produced more thermalized Ps. Thus, by proper selection of the film porosity and the implantation positron energy one may expect to tailor the Ps velocity distribution. The experimental observations (detection of a 140 ns component in the annihilation spectra) confirm that Ps is really escaping into the vacuum.

Similar results are reported in [108].

6.3 Choice of the converter material for AEGIS: test experiments in progress

Among several available materials for the cold positronium formation target, the focus of this proposal is on the use of porous materials like silica or porous alumina films, as they potentially could provide long enough contact for Ps atoms to cool down to a temperature of a few ten K.

The lowest limit on the kinetic energy of the emerging Ps is the target temperature but the previous considerations indicate that a proper choice of the pore size and length can allow one to obtain meV positronium from a colder target. This is particularly important in the AEGIS design where the positronium production target is mounted in in a cryogenic (100 mK) environment very close to the antiproton

trapping region and is presumably in thermal equilibrium with its surroundings.

Porous silica films have been recently developed as low-dielectric interlayer insulators for use in future high-speed microelectronic devices. Voids are fabricated in these films in order to obtain a high degree of porosity and hence to make the dielectric constant lower. Important characteristics of the films are the average size of pores and the size distributions that can be efficiently measured with the so-called Positron Annihilation Lifetime Spectroscopy (PALS) method [100, 101, 102, 103], (see Addendum II).

Test experiments are already in progress in the AEGIS collaboration to select the best material and to optimize the yield of cold positronium.

Equipments suitable for these studies are the one of the [110] group and the ones installed in Trento, in Milano.

6.3.1 Yield of cryogenic converter measurements

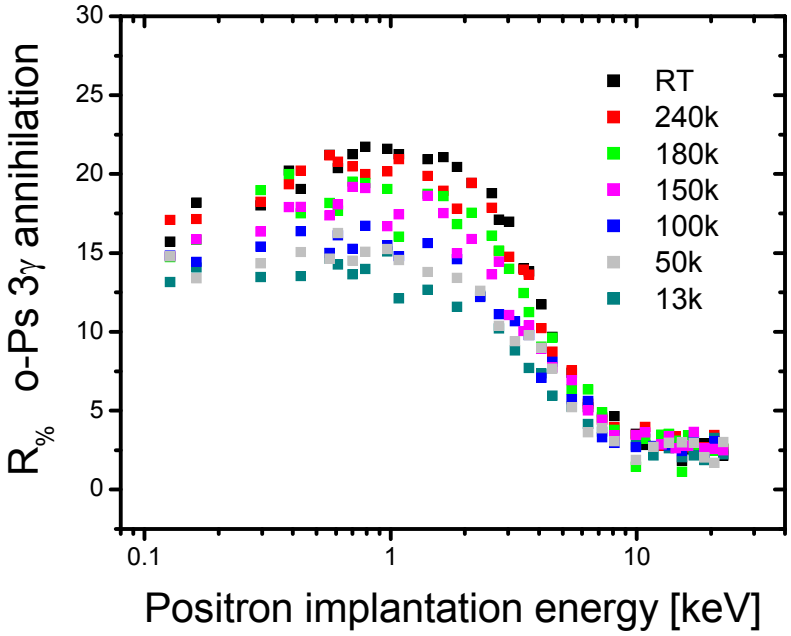

Figure 6.4: Ratio of 3 γ annihilation events to number of implanted positrons vs. positron implantation energy at different sample temperatures (R.S. Brusa and S .Mariazzi, unpublished).

Positronium yield measurements with targets at cryogenic temperatures are in progress in Trento [113] using a slow positron beam. Figure 6.4 shows recent experimental results obtained using as target a thin layer of SiO_2 deposited by spin coating on Si. The addition of porogen PVP 5% and subsequent heating at $600^O C$ ensures the formation of diffused porosity, partially open towards the direction of incoming positrons (reflection geometry). The figure depicts the fraction of implanted positrons that annihilate into 3 γ as a function of the positron implantation energy, for different sample temperatures. 3 γ are the signature of $O-Ps$ annihilation in vacuum. A preliminary analysis of these curves leads to the following conclusions:

- The total yield for conversion of $e+$ into Ps inside the pores is about 72% (in accordance with the known properties of SiO_2)
- At room temperature, a fraction that is evaluated between 10% and 20% escapes from the pores into the vacuum
- The number of 3 γ annihilations decreases moderately when the temperature decreases. The decrease might come from a reduction in the conversion yield, which however is not expected since the Ps process in SiO2 does not depend on thermal activation, or by an increase of the pick-off rate against the walls of the pores.

Similar measurements will soon be performed with a nanoporous membrane of Al_2O_3, which is commercially available as *Anopore* (Whatman).

6.3.2 Ps velocity measurements

The distribution of the velocity of the emitted Ps can be measured using the apparatus of the group of [110] and the one installed in Milano.

The first of the two mentioned equipments uses a time-of-flight method (see e.g. [105]). When positrons are injected into the target, they produce secondary electrons and then stop in the target and form positronium. The number and lifetime spectra of Ps's emitted and decaying in vacuum in flight are measured as a function of the distance between the slits and the target. The secondary electrons, emitted upon positron injection, are used to START the time-clock, while annihilation photons STOP it. Thus, these measurements allow to estimate they Ps yield and velocity distribution.

The experimental setup [111] is designed with the goals of measuring simultaneously i) the Ps TOF spectra even for low intensity components, and ii) the Ps decay position along the beam axis with an accuracy $\simeq mm$, allowing to estimate the $\simeq$ 10 K Ps decay length. Accordingly, the apparatus consists of several distinct and separated parts: i) a slow positron beam with energy range $\simeq$1-10 keV, ii) the lifetime spectrometer, based on secondary electron detection [109], iii) a photon detector to detect photons from Ps annihilation in flight.

The schematic diagram for the slow positron beam and the lifetime spectrometer is shown in Figure 6.5. The beam could also operate in a pulsed mode. A more detailed description can be found in [110].

Slow positrons are produced by moderation of fast positrons emitted through β^+-decay of a radioisotope with intensity $\simeq$ 10 mCu. Mono-energetic positrons from the moderator are separated from the high-energy positron component by a curved B-field serving as a velocity filter. The magnetic coils provide a quasi-uniform longitudinal magnetic field of about 70 Gauss to guide positrons down to a sample, see figure 6.5. The positron transportation energy is selected to be 200 eV, while for the transportation through the velocity filter it is about 30 eV. The lifetime detector is located at the end of the beam line. The energy of a positron impinging on the sample can be varied simply by floating the sample to a desired electrostatic potential.

The principle of the PALS spectrometer is as follows [109]. The continuous beam of positrons with an energy of a few keV guided by the magnetic field passes through a first region with transverse electric and longitudinal magnetic fields, i.e. the $E \times B$ region. The transverse electric field is created by a pair of deflection plates (DP) with potentials $\pm$ 200 V applied to either plate, respectively. For the given values of the electric and magnetic fields the drift velocity of positrons perpendicular to the E-and B-fields is $V_d = 2 \times 10^3$ m/s resulting in a positron displacement of a few cm. Positrons then move further toward the sample and enter the second region of deflection plates (DP2). The electric field in this region has the same value of 20 V/mm but the opposite direction with respect to region DP1. Hence, the drift direction of the positrons is also reversed. As a result, downstream of region DP2 , positrons will move back onto the axis of the beam.

In order to detect annihilation photons from the Ps decays in flight, two kinds of available scintillators are planned to be used: i) NE110 plastic scintillators, and ii) BaF_2 scintillators. The NE-110 or BaF_2 scintillators could be coupled to the photo-cathode of photomultipliers, e.g. XP 2020(Q). Due to the magnetic-field environment, the (PMT+scintillator)-assembly has to be magnetically shielded. The size and type of the magnetic shield materials is chosen in accordance with the simulation results.

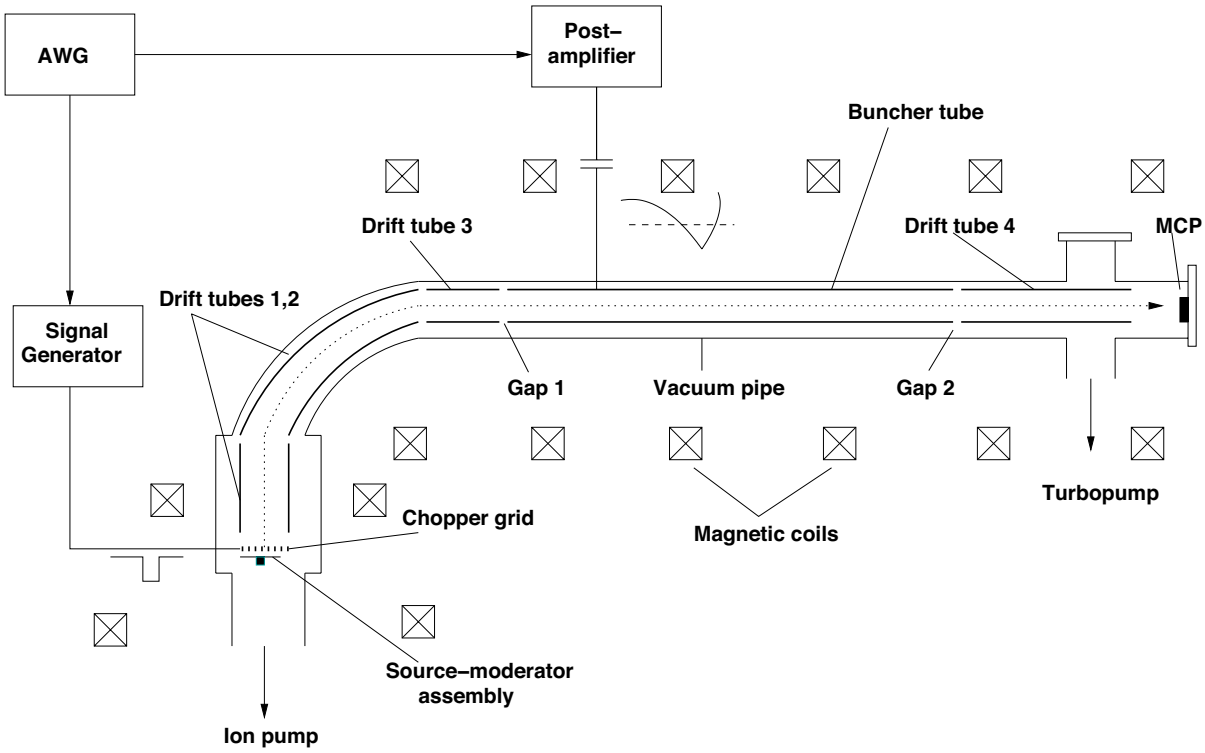

Figure 6.5: Schematic diagram for the slow positron beam with the secondary emission lifetime spectrometer.

A facility with a slow positron beam is available in Milano; an upgrade [112] to allow the measurement of the Ps velocity spectrum is planned. In addition, the construction of a pulsed positron beam is planned in Trento.

A simple experiment that can give important indications about the velocity of Ps is in progress with the equipment of [112]. The positron source is mounted in a sandwich geometry between two discs of Anopore (13 mm diameter) inside a vacuum chamber. Part of the positrons will slow down in the membrane and form Ps in the pores. The Ps atoms coming out of the pores in the vacuum chamber will either annihilate in flight or hit a pair of metallic diaphragms symmetrically mounted at a variable distance x from the source-membrane sandwich. Two experiments are envisaged with this simple apparatus:

- Measurement of the time spectrum of the annihilation. It is expected to observe time spectra containing: a) in the time region from 0 to a few nanoseconds, a very large distribution coming from all positrons that do not form Ps and from Ps formed and annihilating inside the pores; b) an exponentially decreasing distribution that corresponds to o-Ps annihilation in flight (mean life 140 ns); c) a delayed distribution corresponding to o-Ps atoms that annihilate when colliding with the diaphragms after a time-of-flight $t = x/v$.

- Measurement of the number of 3 γ annihilations by means of a triple coincidence set-up. The number of triple coincidence events is expected to grow toward an asymptotic limit when the distance of the diaphragms increases from 0 to a few millimeters (the distance that a Ps atom of 10 meV can travel during 140 ns is about 5 mm). The slope of the curve contains information on the Ps velocity spectrum.

Chapter 7

The design of AEGIS

In this chapter we describe the design of the experimental apparatus able to realize the production of the antihydrogen beam and the gravity measurement with the Moiré deflectometer. The basic experimental steps have been already summarized in Chapter 1: for clarity here we recall them and we add some more details.

- The production of antihydrogen is based on the charge exchange reaction between Rydberg positronium and cold antiprotons $Ps^* + \overline{p} \rightarrow \overline{H}^* + e^-$. Antihydrogen will be produced with a velocity distribution of few tens m/s (energy of about 100 mK) and with a distribution of quantum states peaked around an experimentally tunable value of principal quantum number n. n will be in the range $25 - 45$ and it will be experimentally optimized.
- An appropriate electric field will be applied to sectors of the trap electrodes (Stark accelerator) immediately after the formation process to give to the antihydrogen a velocity of the order of few hundreds m/s in the horizontal (z) direction, while keeping the radial velocity in the tens m/s range.
- The Rydberg antihydrogen will decay toward the fundamental state (or the 2S state) during flight before reaching the end of the bore of the magnet and the Moiré deflectometer (about 30 cm). If necessary the decay can be accelerated by a appropriate laser stimulatiion.
- The Moiré deflectometer is mounted outside the bore of the magnet and in zero magnetic field. The beam will traverse the grating of the Moiré deflectometer for the gravity measurement. The vertical position and the arrival time of each antihydrogen atom are measured by a silicon strip detector.

To achieve these conditions will require the following:

- A bunch (some 10^7 particles with a bunch length of few tens ns) of antiprotons is delivered by the AD every $\sim$ 100 sec. They will be trapped in a Malmberg-Penning trap (catching trap) mounted in a horizontal cryostat inside the bore of a 3 Tesla magnetic field and cooled by electron cooling down to sub–eV energies in a cryogenic environment at $\simeq 4K$. The antiproton cloud will be radially compressed and then transferred into a second trap mounted in a colder region (100 mK) and with a magnetic field of 1 T (antihydrogen formation trap). Here antiprotons will be cooled down to 100 mK. By stacking several AD shots and by careful handling of the antiprotons we can assume to have on average $\simeq 10^5$ cold antiprotons ready for recombination. Cooling in the antihydrogen formation trap can be carried out in parallel to catching and cooling of new antiprotons arriving from the AD.
- 10^8 positrons (or more) accumulated in a Surko type device in about $200-300sec$ will be transferred from the accumulator in a dedicated trap (UHV positron trap) mounted inside the same magnetic field as the antiproton catching trap. Here the bunch will be compressed in space and time with standard non–neutral plasma techniques. The positrons will then be transferred into a trap in the region close to the porous target where positronium will be formed. We expect to obtain a bunch length of the order of ten ns and a radius of the order of 1 mm. The bunch will be accelerated towards a porous target material where ground state positronium atoms with a velocity of the order of a few 10^4 m/s will be produced.

- The positronium cloud emerging from the target will be excited by two laser pulses into a selected Rydberg state with quantum number n ranging from 18 to about 30. We estimate that we could have about $5 \cdot 10^6$ excited positronium atoms.
- The antihydrogen formation trap hosting the cold (100 mK) antiproton cloud is mounted very close to the positronium production target. Cold (100 mK) antihydrogen atoms will be produced during the time in which the Rydberg positronium atoms traverse the antiproton cloud. The expected number of Rydberg antihydrogen atoms is in the range between 100-1000 / cycle.
- Focusing of Rydberg positronium by proper electric field will be exploited to maximize their spatial overlap with the antiprotons.
- A detector (similar to the one used in the ATHENA experiment) able to reconstruct the antihydrogen annihilation vertex by measuring the space and time coincidence of the pions generated in the antiproton-nucleus annihilation and the two gammas coming from the e^+e^- annihilation surrounds the antihydrogen formation trap. This detector allows the identification of the antihydrogen production and the measurement of the antihydrogen velocity.
- Antiprotons that have not recombined can be rapidly transfered back towards the catching region before applying the accelerating Stark field, and will of course be reused.
- Radial cooling of the Rydberg antihydrogen beam using pulsed (quasi CW) Lyman-α laser light can be implemented to focus the beam onto the gratings.

The flexibility of the design allows to experimentally optimize the implementation and timing of the various steps leading to the formation of a beam of antihydrogen atoms, and to introduce different types of particle manipulations. The gravity measurement requires accumulating the signals of individual atoms over several weeks; this demands a high stability of the experimental conditions. We plan to insert in the measuring cycles a number of checks on the stability of all procedures, devices and conditions and to continuously monitor the experimental parameters.

A particular feature of AEGIS is that the antihydrogen production is pulsed. While the preparation of the cold antiproton cloud and the Rydberg positronium require a time of the order of few hundred seconds, the production of antihydrogen will happen during a short time interval, less than 1 μsec, experimentally well determined. This pulsed production leads to several advantages compared to the continuous antihydrogen production typical of the nested trap in which the antihydrogen is produced over a time interval of several tens of seconds [127]. Among them we underline

- the definition of the production time allows the use of time-varying electric field gradients to generate the beam;
- the definition of a start time allows to measure the velocity of the antiatoms in the Moiré deflectometer by their time of flight;
- the antihydrogen velocity distribution immediately after its production can be determined by measuring the time difference between the formation time and the annihilation time on the trap wall;
- high power pulsed Lyman-α light can be used to radially cool the antihydrogen beam.

7.1 Layout of the apparatus

The main components of the AEGIS apparatus are a Surko–type positron accumulator, a superconducting magnet (we will refer to it as main magnet), a dilution refrigerator cryostat, several electromagnetic traps for charged particles, the grating system for the gravity measurement, various types of detectors and laser systems.

The cryostat mounted inside the main magnet provides the cryogenic environment necessary for the handling and cooling of the charged particles. The traps for the charged particles, the target for the positronium formation and the electrodes for the Rydberg antihydrogen acceleration, as well as the gratings of the Moiré deflectometer and the antihydrogen position detector at its end are mounted inside

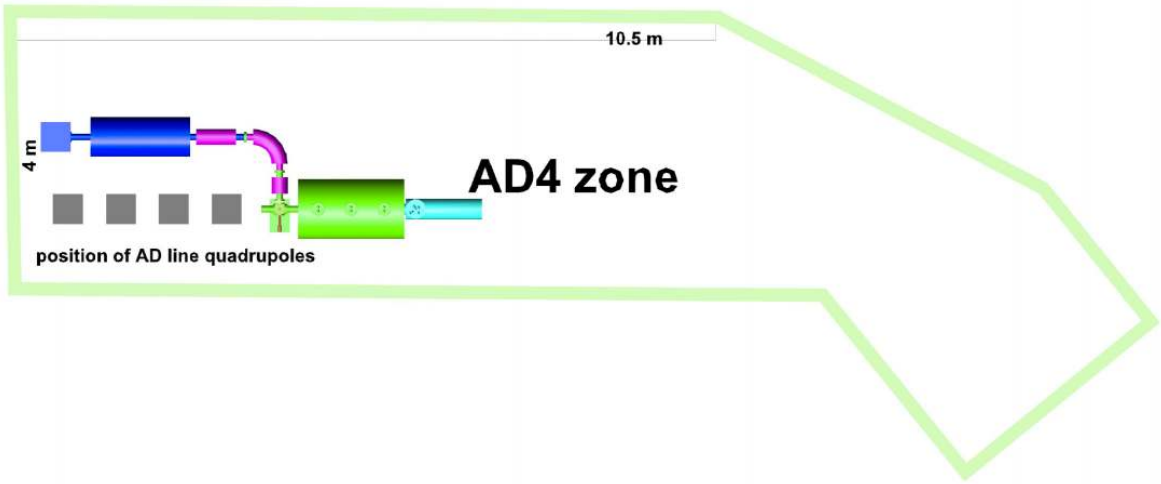

Figure 7.1: Overview of the AEGIS apparatus in the AD4 experimental area. The blue cylinder is the cryostat; the green cylinder around it indicates the main magnet. The second blue cylinder is the magnet of the positron accumulator.

the cryostat. A low temperature of 100 mK is needed only in the small region where the antihydrogen will be formed; a temperature of $\simeq 4\ K$ is sufficient in other regions of the apparatus. A dilution refrigerator cryostat will cool the central region to the required 100 mK.

Positrons must be injected inside the main magnet from the same side as the antiproton beam because one side of the apparatus has to be free to allow the gravity measurement.

Space constraints due to the available room in the requested experimental (AD DEM) area are taken into account in the design.

Figure 7.1 schematically shows the main magnet, the cryostat and the positron accumulator in the experimental DEM area at the AD. Figure 7.2 shows the AEGIS apparatus in more detail.

Electromagnetic traps for charged particles are widely used in various sections of the apparatus: to accumulate positrons in the Surko–type accumulator, to catch and cool antiprotons and to prepare the positrons for positronium production. They are basically made by a series of cylinders of appropriate length and radius to which static voltages are applied to ensure the axial trapping while a uniform magnetic field along the trap axis provides the radial confinement. Space charge electric fields very often have to be taken into account to describe the dynamics of the confined particles. In most cases, our clouds will behave like non–neutral cold plasmas whose properties are well know and largely studied, both theoretically and experimentally [119]

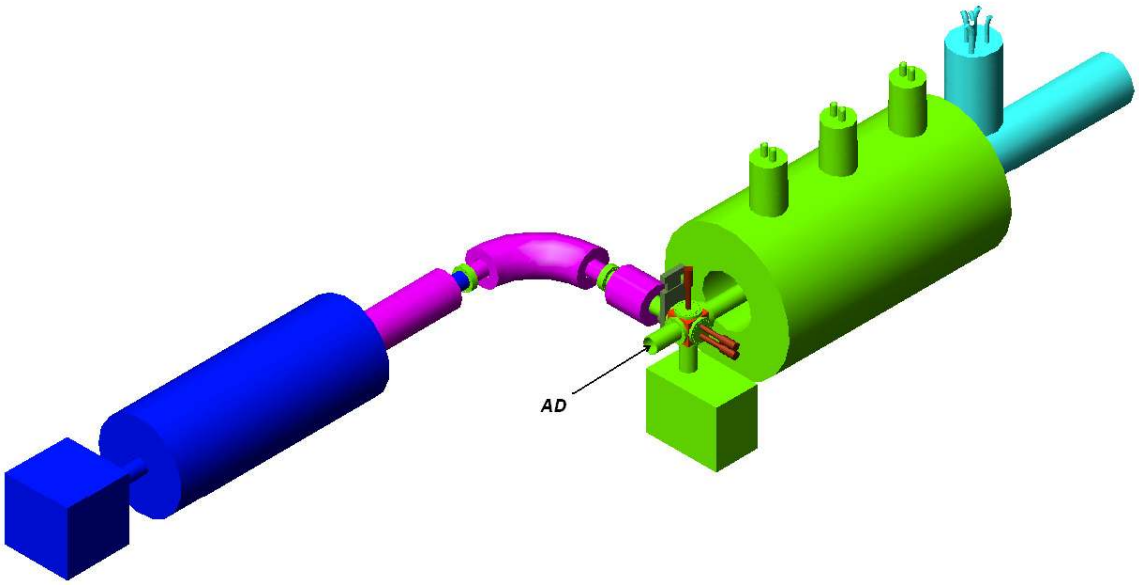

Figure 7.2: Overview of the AEGIS apparatus (see 7.1).

7.2 Positron accumulator

Positrons will be accumulated using a Surko–type positron accumulator. The techniques were pioneered at the University of California San Diego positron [140, 141, 142] and electron [143, 144, 145] groups; a device of this type has been used with success in the ATHENA experiment and the technology is now so well established that a commercial version of the system is available [117].

The operation of the positron accumulator is based on the buffer gas capture and cooling of positrons in a Penning-Malmberg trap. Positrons emitted from a radioactive ^{22}Na source are moderated using solid neon. Moderators are usually grown at a temperature of 7 K with ultra-pure neon admitted at a pressure of 10^{-4} mbar for few minutes. [118],[146, 147, 148]. After the moderator a slow positron beam with typically $2 \cdot 10^5 e^+/smC$ is obtained. Using a 40 mC source $8 \cdot 10^6 e^+/s$ are expected. The accumulator traps and cools this continuous beam of slow positrons guided into the trapping region using axial magnetic field transport. Figure 7.3 shows the trapping region.

In order to remain trapped, positrons have to lose some axial energy during their travel before reaching the end of the trap. Electronic excitation of the nitrogen gas is the cooling mechanism. Such a transition is favored in nitrogen compared to positronium formation, which is the only other major inelastic channel open at those kinetic energies. Once trapped the positrons continue to lose energy in collisions with the gas, finally residing in the potential well formed by the voltages applied to the large diameter trap electrodes. As figure 7.3 indicates, a differential pressure is maintained along the trap axis. The trap potential well minimum is located in the region with the lowest pressure. A magnetic field of $0.15T$ is normally used . This is realized with non-superconducting coils. Standard non–neutral plasma manipulation techniques (rotating wall [143, 145]) are used to radially compress the positron cloud thus

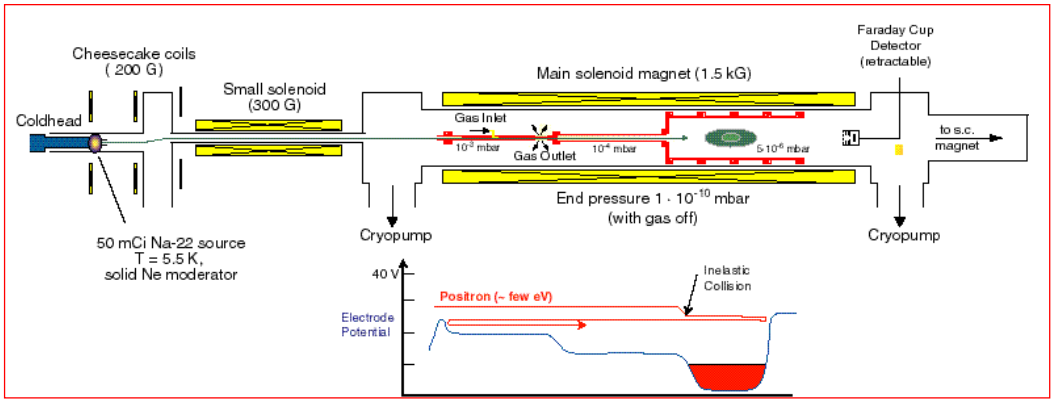

Figure 7.3: Schematic overview of the positron accumulator (see text).

increasing the storage time and the number of accumulated positrons. To implement the rotating wall, one of the trapping electrodes (see fig. 7.3) is split into six segments to which appropriate time–varying electric fields are applied. The compression will be applied during the accumulation phase following the experience of ATHENA. More than 10^8 positrons are expected to be accumulated in 200-300 seconds as figure 7.4 shows.

The detection systems that will be installed to monitor the performance of the positron accumulator are a phosphor screen (allowing imaging the radial profile of the positron cloud); a Faraday cup by which the number of positrons is counted and a CsI-photo-diode detector to monitor the annihilation signal generated when the positrons strike the Faraday cup or the Phosphor screen. Plasma mode detection (described in section 10.8) will in addition be used to follow and optimize the accumulation process. This technique is particularly powerful because is non destructive.

7.3 Transfer of positrons into the main magnet

After accumulation, positrons will be transferred into the trap located inside the main AEGIS magnet.

Before beginning the transfer procedure the gas in the accumulator must be pumped out [164] to limit the gas flux in the ultrahigh vacuum and cryogenic region in the main magnet. The vacuum chamber of the main magnet and of the accumulator are separated by a valve which is opened only at the time of positron transfer. Pulsed magnets and an appropriate electrostatic guiding system will be used to drive the positrons into the trap located in a 4 K region in the main magnet. Depending on details of the transfer procedure, positrons will reach the trapping system with a kinetic energy of several tens or hundreds eV. The high magnetic field provides a cooling mechanism for light particles through the emission of cyclotron radiation (the cooling time constant is about 1 sec). The positron cloud will reach a thermal equilibrium state at a temperature of the order of $4K$ and it will behave as a cold non–

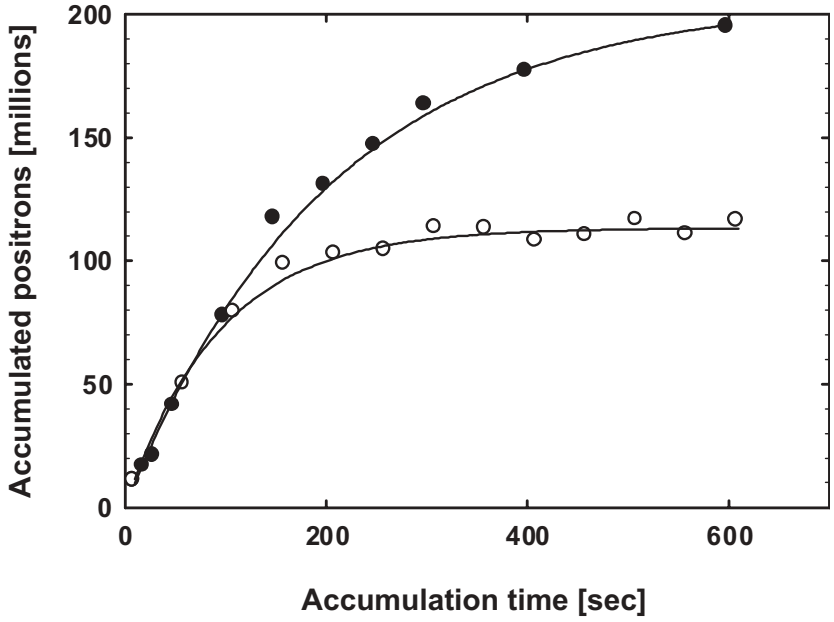

Figure 7.4: Number of accumulated positrons vs time in a Surko type accumulator with and without the use of the technique (rotating wall) allowing radial compression of the cloud. The source activity is 40 mC [164].

neutral plasma [119]. The structure of the electrodes is flexible to allow several plasma manipulations: in particular, stacking of several positron bunches extracted from the accumulator is foreseen.

7.4 The main magnet

A high value of the magnetic field is needed to trap and cool antiprotons in an efficient way while low magnetic field values are desirable in the region where the Stark acceleration of the Rydberg antihydrogen atoms takes place. We are designing an appropriate system of super-conducting multi-coils providing two different regions of homogeneous magnetic field values. The field homogeneity is an important parameter to allow reaching long plasma storage times and low plasma temperature. The first one at 3T with a relative inhomogeneity of less than 10^{-4} (within a cylinder of length 30 cm and radius 3 cm) houses the antiproton catching and cooling trap and the UHV positron storage trap (catching and cooling region). The second region at $1T$, with magnetic homogeneity better than one part in 10^5 (within a cylinder of radius 1 cm and length 4 cm) is in the antihydrogen formation region. The bore end should be at a distance of the order of 30 cm from the center of the homogeneous region at 1 Tesla.

The inhomogeneity $I(\rho, z)$ is defined as follows:

$$I(\rho, z) = |\frac{B_z(\rho, z) - B_0}{B_0}| \tag{7.1}$$

where B_0 is the field value at the center of the given volume and $B_z(\rho, z)$ is the z-component of the magnetic field in the ρ, z position.

Particular care is devoted to reduce the fringe field value in the direction of the grating system.

The bore of the magnet will be at room temperature. A dilution refrigerator cryostat, able to reach 100 mK in the region where antihydrogen is formed and completely independent of the one hosting the coils of the magnet, will be inserted inside the bore. The traps are mounted inside this cryostat (called trap cryostat).

The free space between the room temperature inner bore surface and the external part of the trap cryostat allows laser access to the interaction region. The external flanges of the magnet are used to fix the supports of the mirrors designed to deflect the laser beams from the axial to the perpendicular direction. The length of the magnet bore is 1.6m and its inner diameter is 30 cm.

The magnetic axis of the coil has to be aligned to the axis of the inner bore vessel to within σ 1 milliradians angular deviation.

The magnet can be charged to the desired values in few minutes. Helium consumption is 3 l/day while nitrogen is roughly 1 l/hr.

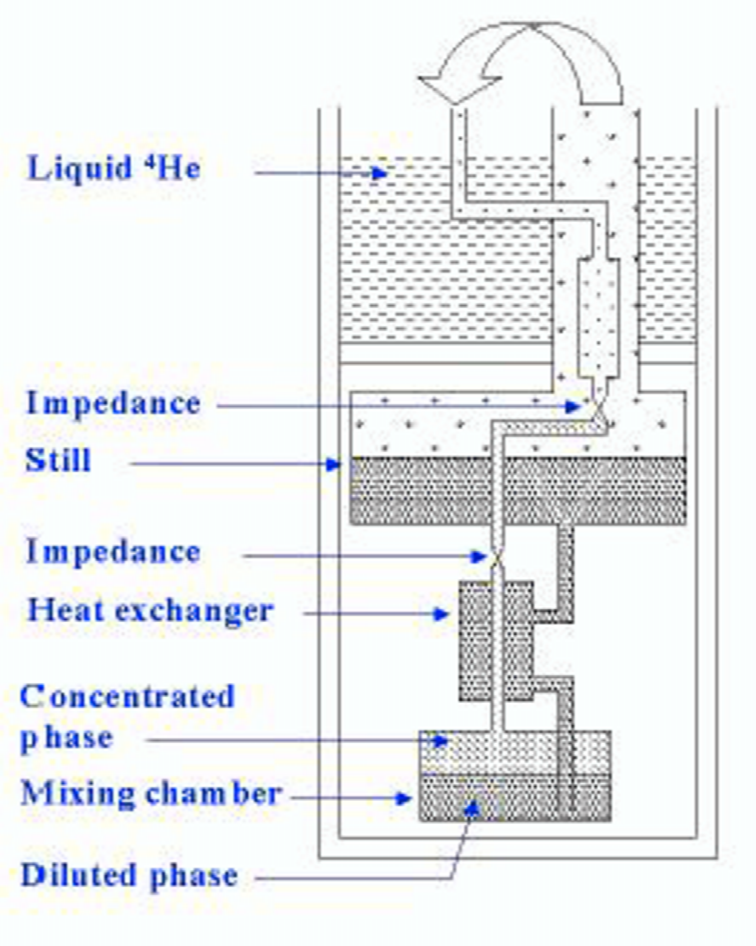

Figure 7.5: Principle of the dilution process

7.5 The cryostat

[1] The principle of operation of a dilution refrigerator (see figure 7.5) is based on the quantum properties of liquid mixtures of the two He isotopes (^{3}He and ^{4}He). When such a mixture is cooled to 0.86 K it separates into two distinct phases: a concentrated ^{3}He phase and a diluted ^{3}He phase. The key point is that even at zero temperature the ^{3}He concentration in the diluted phase of the mixture is finite (6.4%). Below 0.5K, the superfluid ^{4}He of the diluted phase is in a fundamental state with a negligible entropy. For that reason, ^{4}He behaves as a "vacuum". In the mixing chamber, the lighter concentrated phase forms above the diluted phase. A cooling effect is created by ^{3}He atoms passing from the concentrated phase to the diluted phase. This cooling effect can be viewed as an "evaporation" of ^{3}He. This process

[1]The development of the cryogenic design is done in association with O. Testard (retired from CEA/Saclay)

produces cooling of the two phases in the mixing chamber. The solubility limit (6.4%) allows passage of the ^{3}He atoms into the dilute phase even at the lowest temperatures, thus maintaining a large cooling power. The ^{3}He atoms are extracted by pumping on the still at a temperature a little below 1 K. The dilution process runs in a closed cycle. Before being re-introduced into the cryostat, the evaporated ^{3}He is cooled down to 4.2K in a liquid helium Dewar. Then the ^{3}He is liquefied: Finally the liquid ^{3}He is cooled at the still and in the heat exchangers before again reaching the mixing chamber.

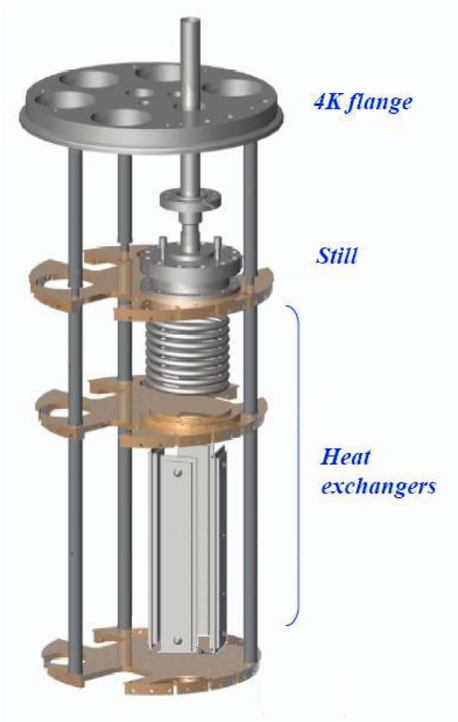

Figure 7.6: External part of the cryostat

The mixing chamber is then the point at the lowest temperature in the system. In the AEGIS setup the mixing chamber will be installed very close to the trap region where antihydrogen will be formed. The rest of the system will be placed outside the main vacuum chamber to optimize the efficiency of the cryostat without affecting the UHV vacuum of the trap region. In figure 7.6 the external part of the dilution cryostat is shown.

Two tubes bring the fluids to the mixing chamber placed below the antihydrogen formation region as shown in figure 7.7. To ensure a good thermal insulation from the room temperature a series of concentric cylindrical shields surround the traps as shown in figure 7.7.

The heat load in the cryostat is dominated by the radiation coming from regions at high temperature. In fact the cryostat cannot be completely closed because antiprotons and positrons have to be injected from a room temperature region in their traps installed inside the cryostat. The two holes necessary for the particles incoming (from the AD and positron injection side) bring 300 K radiation into the cold region. In addition we need windows for the laser access in the region at 100 mK where positronium is formed. In our setup the radiation contribution is estimated to be $\simeq 400\mu W$.

The second contribution is the conductive flow of heat through cables and apparatus supports. The assembly uses the high cooling power available at the temperatures of the different shields (77K, 4K, 0.7K). Solid parts connected to outside of the vacuum chamber and having 300K at one side are thermally anchored at intermediate temperatures, allowing a reduction of the heat load in the coldest region. We estimate at $\simeq 250\mu W$ the contribution to the heat load due to the cables and the various supports. Taking into account these considerations we conclude that the necessary cooling power is about 800 μW@$100mK$; refrigerators meeting this requirement are commercially available.

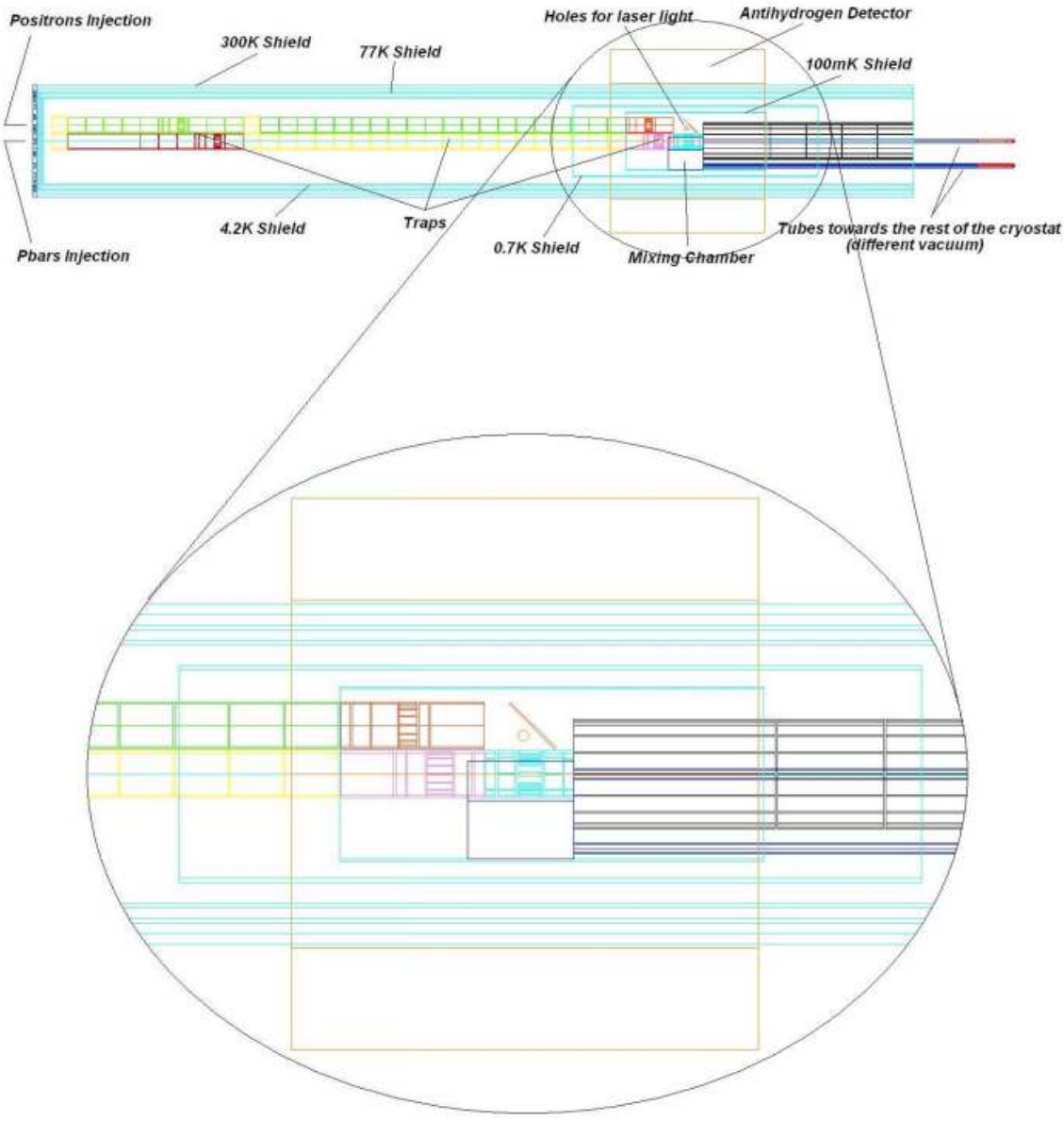

Figure 7.7: Inner view of the cryostat

7.6 The trap system

Malmberg-Penning traps of cylindrical shape are used to handle the charged particles and plasmas. Antiprotons, electrons and/or positrons are accumulated, cooled, manipulated and detected in these

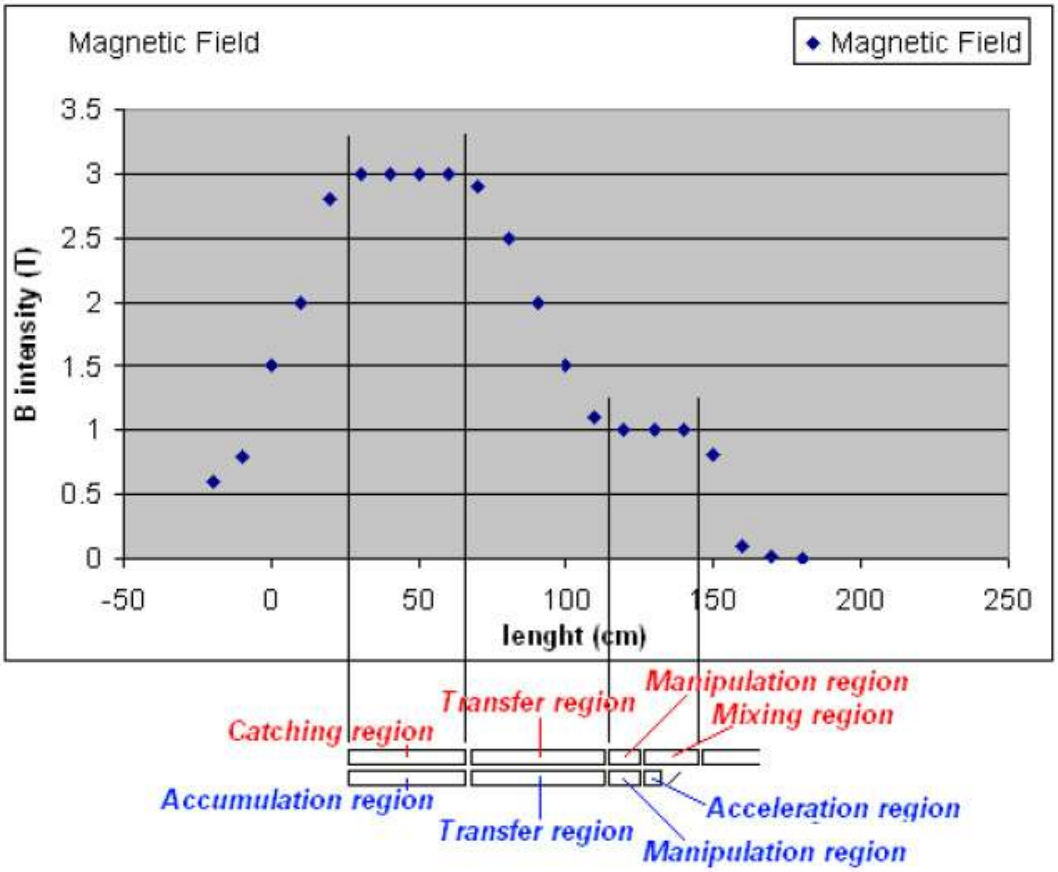

Figure 7.8: Magnetic field profile and related trap system sections. The two parallel trap systems (antiproton and positron traps) are shown.

traps. Each trap electrode receives static or time–variable voltages. Two parallel series of electrodes are mounted inside the cryostat close to each other: one of them (the bottom one in figure 7.9) is used to handle the antiprotons while the second one is devoted to positrons. Figure 7.9 shows the design of the AEGIS charged particle traps and figure 7.8 shows the magnetic field profile and the traps. The trap radius will typically be 1 cm.

7.6.1 Traps in the high field region: antiproton catching trap and UHV positron accumulation trap

The trap in which catching, cooling and stacking of the antiprotons coming from the AD is realized and the trap where the positrons transferred from the Surko accumulator are stored and manipulated are mounted in the homogeneous magnetic field region at 3 Tesla.

The antiproton catching trap is composed of 12 cylindrical electrodes. The two outermost electrodes ($HV_{entrance}$ and HV_{exit}) supply the high voltage to catch the incoming AD antiproton bunches. Their profile is smoothed to avoid electrical discharges, and particular care is put in designing their supports. Alumina spacers are used for this purpose. The central part of the trap, composed of 10 electrodes, is used to cool the caught antiprotons via electron cooling and subsequently store the cold antiprotons until the time when they are transfered. In this central section seven (out of ten) electrodes are designed to produce an harmonic potential (Penning trap) along the axis by an appropriate choice of the electrode lengths and applied voltages. The presence of the harmonic well is important to measure the shape and density of the electron plasma by detecting the plasma modes as described in chapter 10.8. One of the electrodes of the harmonic region is radially split in four in order to allow the application of the rotating

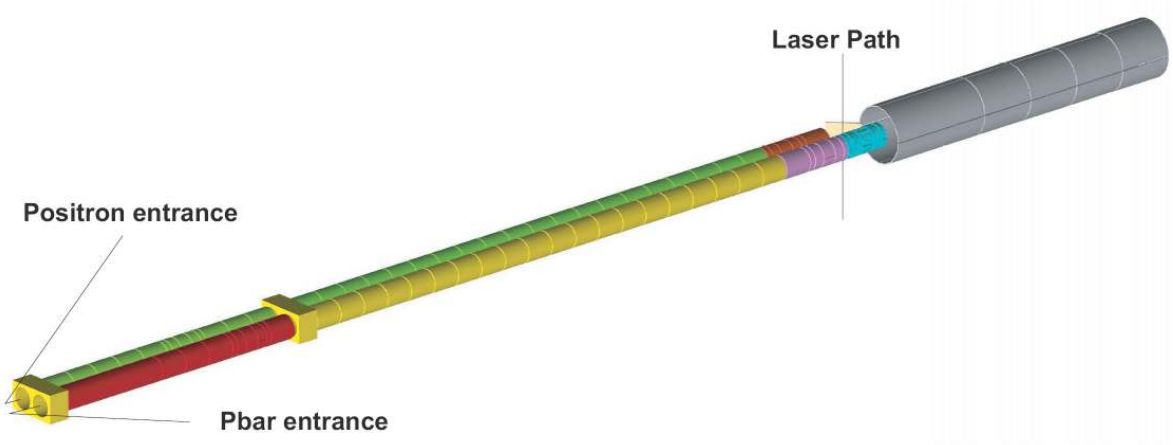

Figure 7.9: Overview of the AEGIS trap system. Note the two parallel stacks of electrodes that will be used for positrons and antiprotons. The trap radius is 1 cm in this drawing.

wall technique for plasma compression [143] or to perform antiproton sideband cooling. A detailed view of the electrodes is provided in figure 7.10.

The UHV positron trap section located in the 3 Tesla field is composed of 12 electrodes and it is dedicated to accumulating and shrinking the positron bunch via a rotating wall technique using the sectored electrode. Also in this region, the possibility of forming an harmonic potential enables the monitoring of the shape of the positron cloud through detection of the plasma oscillatory modes. Once every $\sim$ 100 seconds a positron bunch accumulated in the Surko–type device is injected into this trap and is cooled there through cyclotron radiation emission down to the cryogenic temperature of 4 K. This electrode stack, parallel to the catching trap, can be seen in detail in figure 7.10.

A residual gas pressure well below 10^{-12} mb is needed to obtain a sufficiently long storage time of the antiprotons. The cryogenic environment ensures such a very low pressure. Particular care has to be used to limit the gas flow from the Surko–type accumulator during the transfer of positrons.

7.6.2 Electron source, Faraday cup, antiproton degrader and imaging system

Antiprotons are delivered by the AD with 5 MeV kinetic energy. An appropriate set of foils placed along the antiproton path before the trap entrance degrades the antiproton energy and produces an antiproton beam with lower energy [164]. A small fraction of these antiprotons is caught in flight in the trap by properly timing the trap voltages. A cloud of electrons (about 10^8 electrons), needed to cool the antiprotons in the trap, has to be preloaded in the inner region of the catching trap before the arrival of the bunched antiprotons. These electrons are obtained from an electron source (a barium oxide

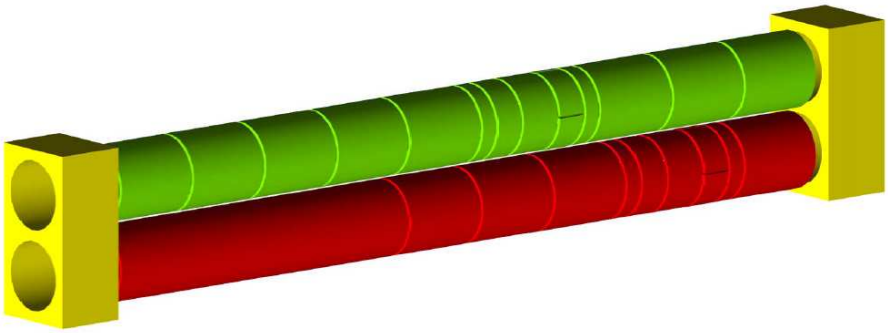

Figure 7.10: Catching trap for antiprotons (bottom trap) and UHV accumulation region for positrons. Note that the two stacks share the two HV electrodes.

disc cathode from Kimball Physics Inc.) mounted outside the cryostat on the AD side on a movable support. In this region, again on a movable support, a charged particle imaging system made by an MCP and a phosphor screen with a suitable light guide will be mounted. The last antiproton degrader acts as Faraday cup and allows to count the number of electrons, as well as to detect antiprotons that are dumped on it through detection in the various scintillators mounted outside the bore of the magnet of the antiproton annihilation products (monitor detectors described in chapter 10). A similar Faraday cup will be mounted on a movable feed-through at the end of the UHV positron trap.

7.6.3 Traps in the low magnetic field: antihydrogen formation region

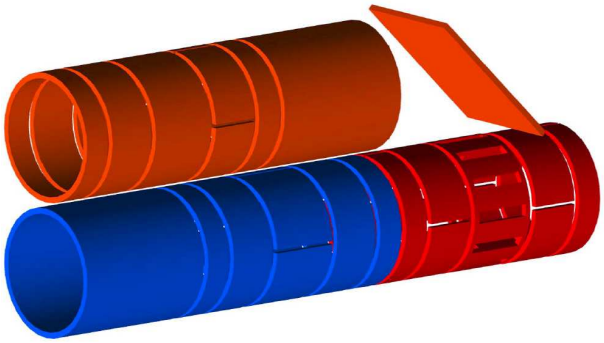

Figure 7.11: Final parts of the stacks. Manipulation and acceleration electrodes for positrons and manipulation and mixing trap for antiprotons. The last part (mixing region) is formed by a Penning structure in which the inner electrode is "transparent" to allow the positronium produced on the 45° converter, and laser–excited into Rydberg positronium, to traverse the cold antiproton cloud.

Antiprotons and positrons will be transferred into traps located in the ultra-cold region ($100mK$) at 1 Tesla by properly shaping the electric field along their path. The approximately 20 electrodes located in the region where the magnetic field changes from 3 to 1 Tesla are designed for this purpose. There is a similar set of electrodes for antiprotons and positrons. The magnetic field maintains the radial confinement. Its decrease by a factor of three leads to an increase of the cloud radius by a factor $\sqrt{3}$.

At the end of the transfer region 6 additional electrodes can be used for re-shrinking the bunches via rotating wall or sideband cooling.

The manipulations of the positron cloud before and after the transfer from high to low magnetic field have the purpose of producing a positron bunch with a radius of $r_{Ps} \simeq 1$ mm. This bunch has to be accelerated towards the porous target with a tunable kinetic energy of some keV. The time length of the

positron pulse hitting the target has to be of the order of ten ns. This condition has been already obtained in a similar experimental apparatus [120] [118] by properly shaping the electric field. The simplest way consists in producing a parabolic potential. Then, if space charge electric fields are negligible, the time to arrive at the well minimum is the same for all the positrons. Voltages of the order of few KV are necessary to produce pulses with sub-ns time lenght in presence of space charge.

A set of electrodes is devoted to the antiproton transfer and manipulation.

The final trap region where the antiprotons should reach the $100mK$ temperature is a Penning trap. A semitransparent electrode has to be used to allow the passage of the Rydberg positronium 7.11: its design should be optimized to allow the passage of the maximum number of positronium atoms while maintaining a good harmonicity of the trap. A cryogenic tuned circuit will be connected to this Penning trap to cool the axial motion of the electrons stored together with the antiprotons.

7.6.4 Positronium formation target

The porous target where positronium will be formed is mounted at a suitable angle in front of the transparent electrode of the antiproton trap (see figure 7.11). The choice of a geometry that allows to maintain a standard trap design for the cold antiprotons and to position the positronium production target as close as possible to it is particularly complicated. The antiproton trap should in fact behave as much as possible as an "ideal" trap with a high level of symmetry in the applied field to prevent heating due to the expansion and radial transport of the plasma, phenomena commonly present in asymmetric traps. These effects could limit the possibility of reaching a temperature as low as 100 mK.

The present design choice satisfies this requirement once the transparent electrode is carefully designed. The high voltages applied to the positron section should not perturb the antiproton trap and this is also achieved in the proposed design. In addition the necessity of shielding (from the electrical point of view) the antiproton cloud from the positronium target if this is made by non–conducting materials has to be taken into account.

Our geometry allows also for the possibility of inserting in the space between the conversion target and the antiproton trap a set of suitable electrodes to create an electric field that would focus the positronium cloud onto the antiprotons. This would maximize the number of formed antihydrogen atoms.

In addition, having the parallel trap design avoids that the secondary electrons emitted from the target when positrons hit it reach the antiprotons; they are guided by the electric field in the direction of the AD and are radially confined by the magnetic to within a few mm; these electrons can be used as a diagnostic for the formation of positronium. The temperature of the target will be that of the environment. We assume here that the porosity of the target and the energy of the positron beam can be selected to obtain positronium with the needed velocity of a few 10^4 m/s. Assuming 10^8 positrons, we will produce some 10^7 positronium atoms exciting the conversion target into the vacuum.

7.6.5 Stark acceleration region

The sets of electrodes forming the trap and those nearby are used to create the electric field which will accelerate the Rydberg antihydrogen atoms after their formation. The Penning trap is transformed into a Rydberg Stark accelerator. For this reason all the electrodes in this section are radially cut in appropriate ways to allow the creation of an electric field with a strong gradient along the magnetic field direction, and a small gradient in the radial direction. Immediately after the formation of antihydrogen, the trap electric field will be manipulated in time and space to salvage the antiprotons that have not recombined in a nearby trapping region in the direction of the 3 T section of the magnet; only subsequently will the electric field needed to accelerate the Rydberg antihydrogen atoms towards the deflectometer be applied. The acceleration takes place in a region of the order of 1-2 cm length. The radius of the electrodes is enlarged in the region behind the acceleration section to allow for an expanding antihydrogen beam.

7.7 Grating system

The two grating of the Moire deflectometer and the position sensitive silicon detector will be mounted inside the cryostat. The main reason for having the grating cold is to avoid that hot radiation from their surface reaches the cold antiproton trap. The temperature of the detector will be around 140 K. As a

reference, the grating will have a radius of 20 cm and their distance will be 40 cm. These values can still be tuned. A proper magnetic field shielding will externally surround the grating system.

The gratings of the deflectometer must be carefully aligned and we must consider two different tunings:

- the slits of the gratings must be made parallel with a very good accuracy, estimated to be of the order of 1 μm over the grating useful height close to 10 cm, corresponding to an angle error close to 10 μradians. The direction of the slits should be made horizontal, or vertical for test purposes, but with a considerably lower accuracy.

- for each grating, the transverse position x of a reference slit modifies the phase of the fringe pattern by a phase term:

$$\phi_{grating} = 2\pi(x_1 + x_3 - 2x_2)/a$$

  It is useful to control this fringe phase. As we replace the last grating by a detector, it is the detector position which must be connected to the positions of the gratings.

We propose to use the know-how developed to control atom interferometers grating positions by optical methods. For this purpose, transmission optical gratings with moderate number of lines per millimeter (a typical value is 200 slits/mm) are used to build an optical three grating Mach-Zehnder interferometer. The operation and properties of such an interferometer are described in the work of the Toulouse group [138].

The analysis of the alignment defects on the signal of a three grating Mach-Zehnder interferometer was carried in another paper of the Toulouse group devoted to atom interferometer [63] and the validity of this calculation has been tested experimentally [139]. Obviously, these results apply also to optical interferometers. In particular, the fringe visibility, given by equation (24) of this reference, is very sensitive to minor grating misalignments, provided that the useful height of the grating is sufficiently large.

Therefore, we propose to build on the grating and on the detector support supplementary optical gratings with about 200 slits/mm, the slits of these gratings being, by construction, parallel to the slits of the main gratings or of the pixel lines of the detector. With a useful height of about 1 cm, the fringe visibility vanishes for a grating rotation of the order of 2×10^{-4} radians from their optimum position, following equation (24) of reference [63]. With this signal, it seems possible to tune the grating position with the required accuracy.

The combination $(x_1 + x_3 - 2x_2)$ of the x-grating positions can be tested with great sensitivity thanks to this interferometer. The transfer of these x values to those of the gratings used with anti-hydrogen is not trivial, especially because the two types of gratings have not the same period. It should be possible to simplify the problem by using grating periods which are in a simple integer ratio like 3 or 4 and if necessary to use two different optical interferometers with different periods so as to fully suppress any ambiguity.

Finally, the laser power needed to operate such an optical interferometer is very low: excellent signals can be obtained with laser power of the order of a few 10 μW. Moreover, the laser source and the detector can be outside of the vacuum tank, thanks to optical fibers. In these conditions, the power injected in the setup may be reduced at a level fully compatible with the cryogenic environment.

Chapter 8

Positronium excitation by two laser pulses

8.1 Introduction

The optimum value of the mean antihydrogen quantum number, and so the needed positronium quantum number, will be selected on the basis of the experimental data. The range of useful Rydberg levels will be in the range of $n = 20 \div 40$. The laser system devoted to Ps excitation should cover this n range. In the following, we take a value of the principal quantum number of n=35 as reference.

Ps atoms are foreseen to have a maximum temperature of about 100 K. Moreover, they will be immersed in a magnetic field of intensity around 1 Tesla. The Rydberg level will be broadened by the Doppler effect and all its sublevels will be separated by the motional Stark effect and by linear and quadratic Zeeman splitting. Because of these effects, the transition will be to a Rydberg level–band, which results in a width of about two times the Doppler width of our n = 35 reference level.

Since the transition energy between ground state and one of those n states is greater than 6 eV, we are proposing a two-stage process (with lower energy photons), since a 6 eV laser suitable for Ps excitation is not commercially available.

The characteristics of the two laser pulses in terms of power and spectral bandwidth must be tailored to the geometry, the Rydberg level–band, and timing of the Ps expanding cloud. The power of the laser pulses must be enough to provide excitation of the whole Ps cloud within few nanoseconds. The characteristics of the Ps cloud lead us to take into consideration a laser setup composed of the following two systems:

- a system made up of a Dye-prism laser (pumped by the second harmonic of a Q-switched Nd:YAG laser) followed by a third harmonic generator for producing the required 205 nm radiation, see Fig.8.2
- a system composed of an OPG (Optical Parametric Generator) followed by an OPA (Optical Parametric Amplfier) for the generation of the 1670 nm by down–conversion of the fundamental Nd:YAG radiation (derived from the above mentioned laser).

The first laser drives the transition from the ground state to the allowed n = 3 sublevels, and the second laser drives the jump from this n = 3 state to the required Rydberg level–band. The two proposed optical systems are reliable and capable of delivering the required power. This system provides incoherent excitation because of the limited coherence level of the laser light. Therefore the expected excitation probability, when both transitions are saturated by the laser radiation, cannot exceed 30 %. The OPG-OPA laser can be tuned over the frequency interval foreseen for the possible Rydberg range (from n=20 to n=40) thereby providing sufficient flexibility.

This approach makes use of the n=3 intermediate levels, thereby avoiding the problem of the rapid decay of the n=2 level and minimizing the losses due to the ionization process (which is in competition with the desired transitions). In fact, the lifetime of the n=2 excited state is about 3 ns, which is three

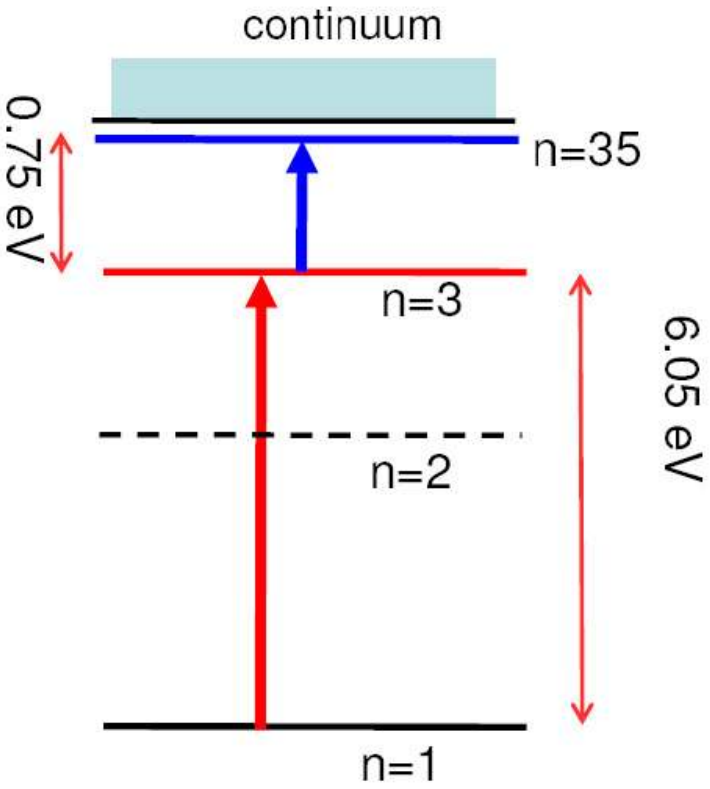

Figure 8.1: The relevant energy levels, with the reference value $n = 35$ (not to scale)

times lower than the lifetime of the n=3 excited level (about 10.5 ns). In addition, while the power required for the transitions $1 \rightarrow 2$ and $1 \rightarrow 3$ up to saturation are close to each other, the transition $2 \rightarrow n$ (up to saturation) requires one order of magnitude higher power when compared with the transition $3 \rightarrow n$, mainly due to the broadening of the Rydberg level–band of the Ps excitation lines, as explained below.

8.2 The detailed scheme of the laser system

The scheme of the laser system which we are proposing is shown in Fig 8.2.

A Q-switched Nd:YAG laser of about 140 mJ and 4 ns drives both the Dye and the OPG-OPA laser systems shown in Fig. 8.2. These generate the pulses for the first and for the second transition, respectively. Most of the energy of the Nd:YAG laser, about 135 mJ, is conveyed along the first branch and is up-converted to the 532 nm second harmonic for pumping a 615 nm Dye laser. The bandwidth of this laser has to be sufficiently large as to cover the Doppler bandwidth of the $1 \rightarrow 3$ transition (nearly 0.04 nm at 100 K). Hence its optical cavity must have prisms as selective elements. The output radiation from the Dye laser is then up-converted with a succession of a second and third harmonic crystals. This system is able to deliver up to 200 μJ at 205 nm wavelength and the expected linewidth can be larger than 0.05 nm.

An exploded view of the second branch of the laser system is depicted in Fig. 8.3. This laser system

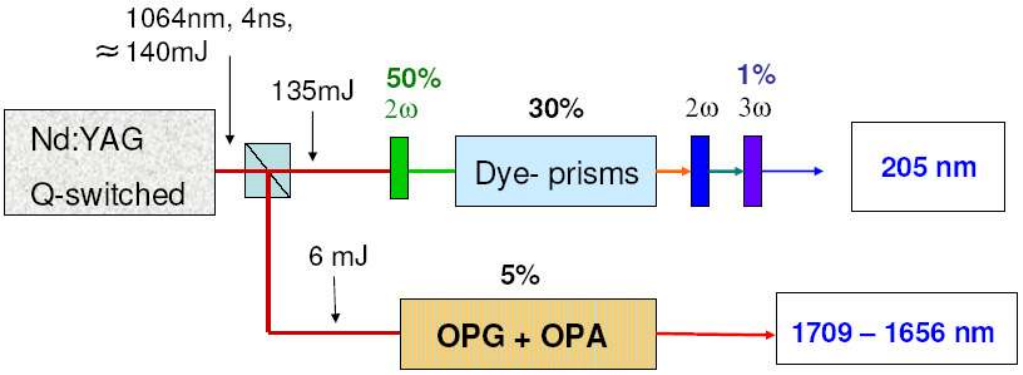

Figure 8.2: Sketch of the laser system proposed for Ps excitation.

generates the radiation in the optical band $1660 \div 1700$ by the OPG. It narrows the spectral bandwidth of this radiation and amplifies - through the OPA - the radiation. The optical parametric generator performs the down–conversion of the 1064 nm radiation of the Nd:YAG. In this down–conversion process the radiation has a spectrum much larger than the one required by the Rydberg level–band of the transition (nearly 0.67 nm on the n = 35 reference level); therefore, in order to reduce the waste of energy in the excitation process, the bandwidth is tuned to the Rydberg level–band by an appropriate etalon. The radiation beam coming out from the etalon is used as a seed of the OPA process, where the 3 mJ radiation beam coming from the the Nd:YAG laser operates as the pump of the amplifier. The seed is amplified up to the the power of $300\,\mu$J.

Both the OPG and the OPA consist of a Periodically Poled Lithium Niobate (PPLN)[114] crystal with a period of $30\,\mu$m, commercially available. The crystal has a very high non linear coefficient ($d_{eff} \simeq 17$ pm/V) and, operates in the Quasi Phase Matching (QPM) condition, absorbing a 1064 nm photon to generate two new photons: a *signal* photon with $\lambda \in [1600, 1700]$ nm and an *idler* photon with $\lambda \in [2600, 3000]$ nm. In this kind of down–conversion process [115] the *idler* and *signal* frequencies can be finely tuned by controlling the crystal temperature of around 200 °C.

8.3 Ps excitation from n = 1 to high n levels

Ps atom excitation by the two described laser pulses is theoretically studied using a multilevel density matrix model, including spontaneous decay from the excited levels and photoionization. The time evolution of the excited states depends on the features of the laser pulses. These are taken, for definiteness, with a gaussian time profile in intensity and a suitable random phase. The linewidth of the laser radiation should be of the same order as that of the Rydberg level–band $\Delta\lambda$ of the Ps atoms in order to maximize the excitation efficiency due to resonant interaction. The time coherence of the laser pulse, or the time

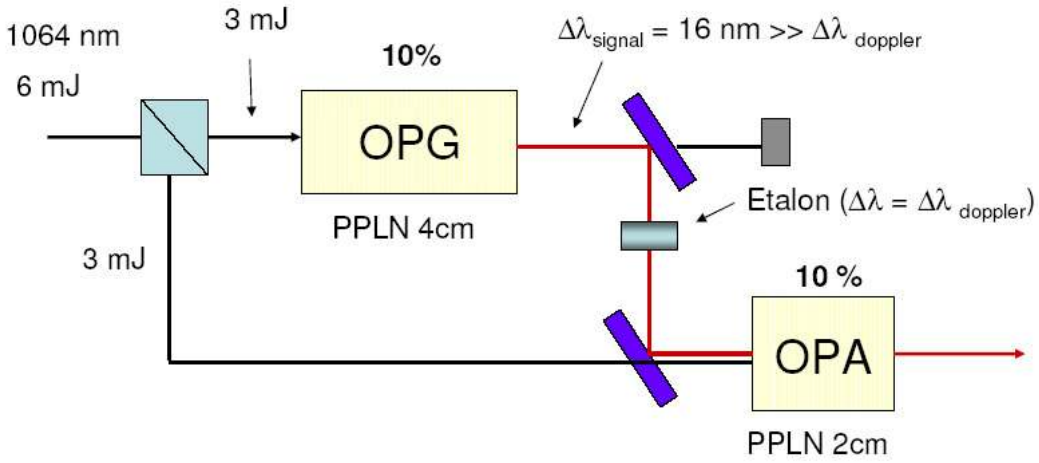

Figure 8.3: Expanded scheme of the OPG–OPA laser system for generating the radiation for the second transition $3 \rightarrow n$.

scale in which the radiation phase can be considered sufficiently constant, is given by:

$$\Delta t_{coh} = \frac{\lambda^2}{c\,\Delta\lambda} \ . \tag{8.1}$$

The Rydberg level broadening comes from the Doppler and the magnetic field effects. The Doppler broadening $\Delta\lambda_D$ at the 100 K temperature turns out to be around 0.35 nm at the reference level. The magnetic field of 1 T induces a wide splitting of the quasi–degenerate n–sublevels due to the notable motional Stark effect over the fast travelling Ps atoms, which mainly mixes l and m states. The maximum splitting can be estimated to be of the same order as that of the energy difference between adjacent n–levels (3×10^{-4} eV at n=35), assuming negligible n–mixing. This splitting is nearly two times the Doppler linewidth (1.6×10^{-4} eV). At the end, the magnetic field effect is responsible for the level broadening at high n–levels.

The coherence time of Eq.(8.1) comes out orders of magnitude smaller than the time length of the pulses. Because of this, the phase of the light in our model is taken as a "random walk" with that time step.

We have made simulations considering transitions from $(n, l) = (1, 0)$ to the state $(3, 1)$ and from this state to the final states $(35, 2)$ and $(35, 0)$. We have assumed in simulations that the total cross section of the transition from the lower level to the upper band of levels is substantially the same as the cross section of the transition between the two levels connected by electric dipole selection rules. This choice is quite usual in problems of this kind [116]. Because of the presence of a strong magnetic field we assume the polarization of the laser beams to be parallel to the direction of the field, which implies $\Delta m = 0$.

An example of the level populations as a function of time with two in–time laser pulses resulting from simulations is presented in Fig 8.4. The characteristics of the two pulses are tailored to a Ps cloud

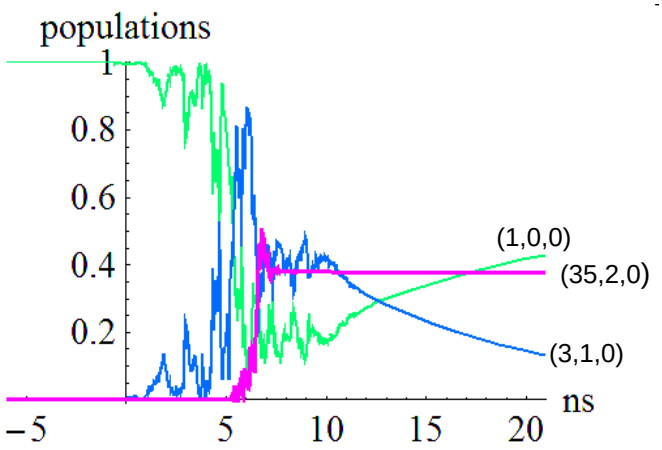

Figure 8.4: Plot of level populations versus time for incoherent excitation.

expanding from the source for about 30 ns at a temperature of 20 K, and are: (1) time length 4 ns, power 20 μJ and spectral width $\Delta\lambda = 0.02$ nm, (2) time length 1 ns, power 40 μJ and spectral width $\Delta\lambda = 0.17$ nm, respectively.

The final excitation probability comes from an averaging process over many simulation outputs. We have verified that when laser pulses are powerful enough so that their fluency F (spectral integrated intensity) is larger than a suitably defined saturation fluency F_{SAT}, the excitation level reaches the expected theoretical value of 30 % valid for incoherent excitations. Simulations relative to a Ps cloud at 100 K, and with an area of about 6 mm^2 (from 30 ns of expansion time) lead to laser power levels (corresponding to saturation fluences) of about 20 μJ and 100 μJ for the first and the second pulse, respectively. These amounts of energy are well below the amounts delivered by our lasers. In the case of a (much) larger Ps cloud area (due to a longer expansion time), we would add a second amplifier stage on the second laser.

We would like to note that the transition $3 \rightarrow n$, with respect to the transition $2 \rightarrow n$, needs a significantly lower saturation fluency, which in turn means a reduction in ionization probability.

A Note. The proposed laser system for the first transition $1 \rightarrow 3$ is a reliable and mid–cost market laser. The laser system for the second transition $3 \rightarrow n$ has instead some state-of-the-art technology which, however, is reported in published literature. This part of the system is already under test and results are expected by the end of this year.

Simulations show an excitation efficiency considerably higher than the 30 % predicted before by exploiting coherent laser light. A study of a new laser design with the required features is under way.

Chapter 9

Ultra-cold antiprotons

9.1 Antiproton capture and cooling down to a few Kelvin

The standard operating procedure for antiprotons in AEGIS will consist of capture in the catching trap, cooling by collisions with a preloaded cloud of electrons, stacking of many AD shots, and possibly radial compression of the antiproton cloud followed by transfer into the antihydrogen formation region. Here antiprotons will be cooled to sub-Kelvin temperatures. Any antiprotons that have not recombined during the production of antihydrogen will be reused through suitable electrode voltage manipulations to move them from the recombination region to the catching region.

The antiprotons delivered by AD in bunches of about $2.5 \cdot 10^7$ particles within $\simeq$ 100 ns and with a kinetic energy of 5 MeV, traverse a few foils acting as energy degrader. By suitably pulsing the voltages of the catching trap electrodes a fraction of the antiprotons with energy in the keV region can be caught. This procedure has been largely experimentally demonstrated [164] and routinely used in the AD experiments. The maximum antiproton energy is related to the voltage potential V_{HV} applied to the electrode that ends the trapping section. The potential of the last trap electrode of the catching trap is initially set to V_{HV}. Antiprotons traversing the last foil of the degrading system with axial energy lower than eV_{HV} are reflected from this potential and captured by "closing the trap", that is applying a voltage V_{HV} to the entrance electrode before they bounce back and return to it. Typically the trap has to be closed after a time interval of 500-700 ns from the antiproton's arrival at the entrance. The antiproton arrival time is measured using the antiproton beam monitor detectors described in Chapter 10. Figure 9.1 shows how the number of captured antiprotons increases with applied trap potential as measured in ATHENA. Typically around 10^4 antiprotons are captured at 5 kV for an incident AD flux of 2.5×10^7/pulse. To maximize the number of available antiprotons, the AEGIS catching trap is designed to sustain voltages up to 10 KV.

Cooling of the high energy antiprotons through Coulomb collisions between them and an electron cloud preloaded in the catching trap has been largely demonstrated [164]. Although the electrons are heated by this process, they efficiently cool themselves by emission of cyclotron radiation in the 3 Tesla magnetic field with a time constant of about 0.4 sec. Ideally, the two species of particles will reach a final equilibrium temperature equal to that of the environment. The cooling process [130] is usually described by the differential equations:

$$\frac{dT_p}{dt} = -\frac{(T_p - T_e)}{\tau_c} \tag{9.1}$$

$$\frac{dT_e}{dt} = \frac{n_p}{n_e}\frac{(T_p - T_e)}{\tau_c} - \frac{(T_e - T_t)}{\tau_e} \tag{9.2}$$

where T_e and T_p are the electron and $\bar{p}$ temperatures, T_t is the unperturbed electron temperature, n_e and n_p are the electron and $\bar{p}$ densities, τ_e is the synchrotron and τ_c the electron cooling time. The latter is given by

$$\tau_c = \frac{3 m_e m_p c^3}{8(2\pi)^{1/2} n_e e^4 ln(\Lambda)} \left(\frac{kT_p}{m_p c^2} + \frac{kT_e}{m_e c^2} \right)^{3/2} \tag{9.3}$$

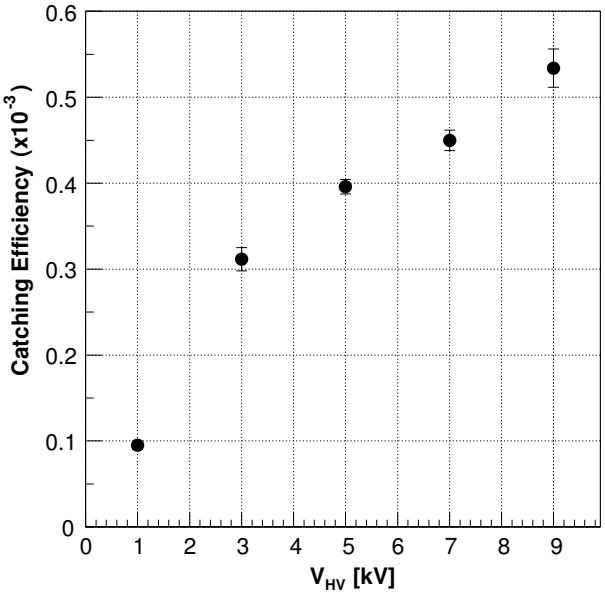

Figure 9.1: Dependence of the catching efficiency on the applied high voltage, V_{HV}. The antiprotons were released from the trap one second after capture. The numbers of captured antiprotons are normalized to the beam intensity measured with HPD-based external beam detectors. [164]

Here m_p and m_e are the $\bar{p}$ and electron masses, e is their electrical charge and Λ is given by

$$\Lambda = \frac{4\pi\epsilon_0}{n_e}\left(\frac{kT}{e^2}\right)^{3/2} \tag{9.4}$$

The solution of these equations shows that 10^4 antiprotons having energies in the keV range can be cooled down to less than a few eV within a few tenths of a second if they overlap completely with an electron cloud of density around 10^7 - 10^8 cm^{-3}.
The cooling process is not exponential and its rate increases very rapidly while the antiproton energy decreases.

As already done in the past by previous experiments, the cooling process can be experimentally optimized by dumping the "hot" antiprotons from the high voltage well (simply releasing the high voltage on the entrance electrode) and then later dumping the "cold" antiprotons stored in the internal electron potential well by varying the potential shape in that region. In this electron trap usually potentials of the order of some tens or few hundred Volts are used. Figure 9.2 shows the fraction of cold and hot antiprotons as a function of the interaction time as measured in ATHENA. Nearly all antiprotons are cooled in about 60 s. At the end of the cooling process, antiprotons and electrons share the same volume. The electrons can then be ejected from the trap by applying appropriate electric pulses of about 100 ns duration which do not affect the heavier antiprotons.

Since the high voltage does not influence the potentials in the central region where the cold antiprotons and the electrons are collected and since the storage time of cold antiproton in the UHV cryogenic environment is very long (hours), it is possible to stack many bunches of antiprotons in the catching trap before transporting the cold antiprotons towards the mixing region. This is illustrated in figure 9.3 which shows a linear increase in the number of trapped cold antiprotons with the number of AD shots.

The cold electron cloud at the end of the cooling process behaves as a cold non neutral plasma since the Debye length is shorter than the typical plasma dimensions. The phase space distribution at thermal equilibrium [121] with temperature T is given by

$$f_{\mathrm{Maxwell}}(r,z) = n(r,z)\left(\frac{m}{2\pi k_B T}\right)^{3/2} e^{-\frac{m}{2k_B T}(\mathbf{v}^2 - \omega_r r\hat{\theta})} \tag{9.5}$$

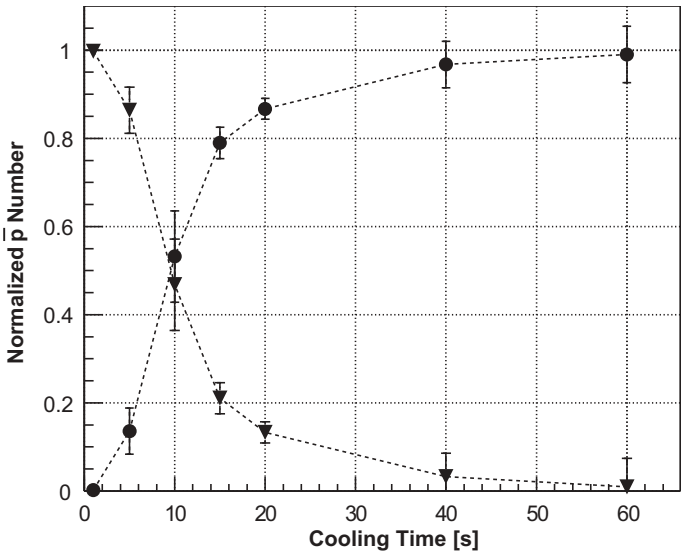

Figure 9.2: Measured fraction of cold (circles) and hot antiprotons (triangles) as a function of their interaction time with electrons. The dashed lines are to guide the eye [164]

The velocity distribution is of Maxwell type in a frame rotating with an angular velocity ω_r that is related to the plasma density. The plasma density $n(r, z)$ can be determined by a self consistent model which takes into account the particle distribution function at equilibrium, the applied electric and magnetic fields and the space charge electric fields [119]. For a Debye length λ_D that is small compared with the dimensions of the plasma, the picture that emerges is that of a uniform density plasma rigidly rotating around the z axis in which the space charge electric field completely shields the applied axial electric field and reinforces the radial field. The plasma is bounded by a surface of revolution where the density falls off within a few Debye lengths. For a Penning trap such surface is an ellipsoid. The approximation T=0 is usually a good one and in this case the the rotation frequency is ω_r is simply given by

$$\omega_r = \frac{qn_e}{2\epsilon_0 B} = 9 \cdot 10^{-3} \frac{n_e(cm^{-3})}{B(T)} \tag{9.6}$$

and the ellipsoid semi-axes r_p and z_p depend on the plasma density and on the trap parameters through the single particle axial oscillation frequency $\omega_z^2 = \frac{4qV}{md_t^2}$. d_t is a geometrical trap parameter whose value is close to the trap length.

Mixed multi-species plasmas in the Penning trap (like electrons and antiprotons) reach the same temperature in a time scale related to their collision time and they can be initially mixed in the same volume. The final equilibrium configuration is the one in which all the particles, regardless of the mass (or generally of the mass to charge ratio), rotate with the same frequency. This configuration is characterized not by a uniform spatial distribution but by a distribution in which the different species form concentric shells ordered by their mass, and where the heavy antiprotons lie outside, but at the border, of the electron cloud. The separation is of the order of the Debye length [123] The time scale to reach such a separation is much longer than the thermalization time and it is unclear if such an effect will play a role in our experimental conditions.

9.2 Antiproton cloud radial compression

When space charge effects can be ignored, the reduction of the radius of the orbits of particles stored in a Penning trap can be performed by a well-established procedure called sideband cooling [157] [158]. This is based on the particular features of the classical motion of a particle in the Penning trap. Referring to

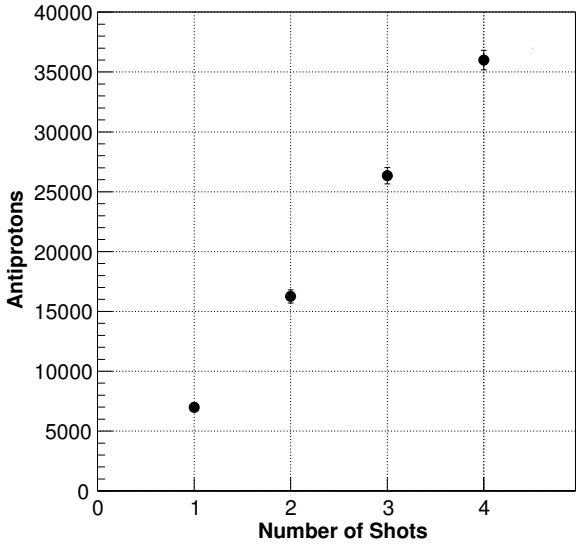

Figure 9.3: Dependence of the number of cold antiprotons on the number of stacked AD shots [164]. Each AD shots contains about 2×10^7 antiprotons.

the radial motion, the combination of the trap radial electric field (proportional to the radial position) and the uniform magnetic field induces an oscillatory motion with two frequencies ω_+ and ω_- and two amplitudes called cyclotron radius and magnetron radius. The sum of the two frequencies is the true cyclotron frequency $\omega_c = qB/m$ of the particle in the magnetic field. The two radii are constant if no dissipation occurs while, in case of cooling, the cyclotron radius is reduced while the magnetron radius changes in a negligible manner. If an additional quadrupolar electric field with frequency equal to the true cyclotron frequency is applied in the trap then the magnetron and cyclotron motion are mixed and coupled: the two radii oscillate in time and the motion is converted into a periodically varying mixture of pure cyclotron and pure magnetron motions. The oscillation period depends on the amplitude of the coupling field and can be experimentally controlled. If a cooling mechanism is present in the trap during the coupling, then both the cyclotron and magnetron radii are reduced and radial compression of the orbit is achieved. The final limit for a single particle is when the cyclotron and magnetron radii are equal. In the case of heavy ions, collisions with a buffer gas are used as cooling mechanism. In the case of antiprotons the presence of the cooling electrons has to be taken into account because they deeply modify the trap electric field. We have developed a model and performed preliminary experiments [159] on sideband cooling of antiprotons immersed in an electron cloud that show that this procedure is a very promising method for centering the antiproton cloud.

In addition succesfull experiments on radial compression of large number of protons (and antiprotons) with the rotating wall technique have also been performed [160].

These two procedures (sibedand cooling in the presence of electrons and rotating wall) will be implemented in the antiproton catching trap.

9.3 Transport of antiprotons from the catching region to the interaction region

Antiprotons cooled by electrons in the catching region will be transported into the recombination region by adiabatically changing the trap electrode voltages in order to move the axial well from the catching trap region to the recombination region. Here adiabatically means that the trap voltages are changed in a time interval longer than the periods of the particle motion in the trap. This transfer procedure allows to transport antiprotons together with electrons and it has been shown to have high efficiency, both in ATHENA as in the transport of a dense electron plasma through a very inhomogeneous magnetic field

in a different experimental setup [128]. The transfer procedure can be completed in a time scale of tens of ms.

The movement of the plasma from a region with magnetic field B_i to a region with magnetic field B_f causes an increase of the radial cloud dimensions of a factor $\sqrt{(B_i/B_f)} \simeq= 1.7$ when going from a 3 T to a 1 T field. The radial symmetry of the confining system, which is known to be essential to guarantee a good plasma stability is present in the whole trap region. If needed, further plasma manipulation and radial compression similar to those performed in the catching trap will be carried out in the recombination region. We will transport $10^4 - 10^5$ antiprotons together with a suitably large number of electrons ($10^7 - 10^8$) and will store them in a Penning-Malmberg trap with an half length of about 1-2 cm in the 100 mK region.

9.4 Constraints on the minimal antiproton temperature

Clouds of antiprotons cooled to 4.2 K and 4.2 K electron and positron plasmas with densities in the range $10^6 - 10^9/cm^{-3}$ are routinely used in antihydrogen experiments and in non-neutral plasma physics devices. Colder (50-100 mK) clouds of electrons with lower density have been stored in a trap mounted inside a dilution refrigerator cryostat for high precision measurements [122]. We discuss here the physics constraints that must be satisfied to allow the antiproton plasma to reach the 100 mK temperature of its surroundings.

If electron cooling is used to cool the antiproton cloud, the consequence is that the 100 mK antiproton plasma cannot be a pure antiproton plasma: electrons must likely remain together with the antiprotons. In fact, they cannot be easily removed from the trap without giving energy to the antiprotons. This is understood because inside a non neutral plasma with T=0 the axial trap electric field is exactly balanced by the space charge electric field. The particles axially bounce back and forth inside the plasma with a velocity related to their temperature. If we suddenly remove all the electrons from the trap then the trap electric field is restored and the antiprotons gain a potential energy depending on their position; this potential energy will be converted into kinetic energy during their oscillation. This energy is a large fraction of eV.

While the presence of electrons is essential, their density can be controlled and optimized. We are planning to reduce in a controlled way the number of electrons stored together with antiprotons by applying fast (50-100 ns long) voltage kicks that "open the trap" for a time short enough to eject the electrons while the antiprotons do not move in a significant way. The amplitude of the kicks compared with the trap energy depth allows to tune the number of escaping electrons. This procedure has been already experimentally proven. After waiting until a new thermal equilibrium condition is reached, the procedure can be repeated. The range of electron densities has to be chosen taking into account that the rotation velocity has to be maintained at a level not exceeding that of a thermal distribution. Using 9.6 we find that – assuming a cloud with 1 mm radius – we need $n_e < 5 \cdot 10^6\ cm^{-3}$ in a 1 Tesla magnetic field to achieve this result. If the plasma half length is $z_p = 1cm$ this density corresponds to about $2 \cdot 10^5$ electrons.

An additional important effect limiting the minimum plasma temperature is Joule heating. We already mentionned in the description of the positron accumulator that, ideally, a non-neutral plasma in a rotationally symmetric trapping system can be confined forever [124] and that, on the other hand, a long series of experiments have shown that mechanical asymmetries, non ideality of the trapping system and collisions with residual gas cause a phenomenon of transport across the magnetic field, leading to a radial plasma expansion. This mechanism is the main process leading to loss of particles in an ultrahigh vacuum and cryogenic environment. Generally, as a charged plasma expands, the electrostatic energy of the space charge decreases and it is converted into internal energy: this effect (Joule heating), being only partially compensated by the cyclotron radiation cooling, causes a significant increase of the plasma particle kinetic energy during its evolution and leads to a regime with a temperature higher than the ambient temperature. Following [129] the heating power $\left(\frac{dKT}{dt}\right)_{exp}$ due to the expansion is roughly estimated here by modeling the plasma as an infinite column with radius r_p and uniform density expanding in the radial direction:

$$\left(\frac{dKT}{dt}\right)_{exp} = \frac{1}{6}\frac{q^2}{\epsilon_0}\left(\frac{n_e}{r_p^2}\right)_0 \frac{1}{r_p}\frac{dr_p}{dt} \tag{9.7}$$

where the product (plasma density × radius squared) is constant in this simple model. Assuming that a cooling system with time constant τ_{cool} is present (radiative cooling and/or resistive cooling) then the time behavior of the temperature can be modeled as

$$\frac{dKT}{dt} = \frac{1}{6}\frac{q^2}{\epsilon_0}\left(\frac{n_e}{r_p^2}\right)_0 \frac{1}{r_p}\frac{dr_p}{dt} - \frac{KT - KT_a}{\tau_c} \tag{9.8}$$

where the first term describes the heating and the second one the cooling. Assuming for simplicity an exponential expansion of the plasma versus time with time constant τ_{exp} then the final equilibrium temperature T_{equil} is

$$T_{equil} = T_a + \frac{1}{6}\frac{q^2}{\epsilon_0}\left(\frac{n_e}{r_p^2}\right)_0 \frac{\tau_{cool}}{\tau_{exp}} = T_a(K) + 3.510^{-3}\left(n_e r_p^2\right)(cm^{-1})\frac{\tau_{cool}}{\tau_{exp}} \tag{9.9}$$

To keep the second term lower than the 100mK ambient temperature we need $\tau_{exp} \simeq< 10^4$ sec assuming $\tau_{cool} \simeq 10$ sec. Expansion rates as low as this have been already achieved in cryogenic, well designed traps. Critical parameters are the homogeneity of the magnetic field in the trap region, the symmetry of the electric field, and the alignment between them.

Electronic noise associated with the trap voltage supply could be a source of heating. All the trap voltages must be properly filtered to avoid that noise components with frequencies close to the plasma modes excite and heat the plasma. The plasma mode detection should be switched off during the cooling phase; the same holds for other active amplifiers connected to the trap electrodes.

9.5 Cooling antiprotons to 100 mK by electron cooling and resistive cooling

The energy of the antiprotons and electrons immediately after their transfer into the antihydrogen formation trap can easily be in the eV range. Due to the low magnetic field of the antihydrogen formation region, the electrons radiate energy with a time constant of $\simeq 4$ sec, longer than in the catching region. On the other hand, the exchange of energy between antiprotons and electrons is much more efficient when antiprotons have eV energy instead of keV energy as in the catching trap. For ambient temperatures higher than few Kelvin, electrons radiate their cyclotron energy and they come into equilibrium with the environment by absorbing black body photons. For lower ambient temperature the cyclotron motion is decoupled from the environment because the number of black body photons with a frequency close to the cyclotron frequency is too low to ensure an efficient absorption. At such low temperatures quantum effects on the cyclotron motion become important. The energy E_c of the (single particle) cyclotron motion with frequency ω_+ of an electron in a Penning trap is

$$E_c = \left(n_c + \frac{1}{2}\right)\hbar\omega_+ \tag{9.10}$$

Here ω_+ is the cyclotron frequency in the trap $\omega_+ \simeq \omega_c = \frac{qB}{m}$ The electrons radiate their energy until the fundamental state with $n_c = 0$ is reached. Beautiful experimental results on this can be found in [125]. Note that in a 1 Tesla magnetic field $\hbar\omega_+ \simeq 1K$ and so the minimum cyclotron energy is 0.5 K. The axial motion of a single electron in a harmonic trap has lower frequency and can be cooled well below this value. Given that the radiation rate of the axial energy is negligible, a further external cooling mechanism is needed. We are planning to use a cold circuit tuned to the axial frequency of the electrons (resistive cooling [157]) to cool the axial motion of the electrons down to 100 mK.

Antiprotons confined together with electrons and colliding with them will be cooled until they reach the axial electron temperature. The higher electron cyclotron energy cannot be transferred to the antiprotons because it corresponds to the fundamental state of the electron cyclotron motion.

The need of a tuned circuit imposes the use of an harmonic trap in the recombination region. A RLC circuit, tuned to the axial oscillation frequency of the electrons ω_z , will be realized by connecting an inductor L to two electrodes of the trap. The resistance is the parasitic resistance associated to the circuit components and it is related to the circuit quality factor $Q = \omega_z LR$. A typical value of the frequency is in the MHz–tens of MHz range.

The current induced on the circuit by the axial motion of one electron is proportional to its velocity and can be written as

$$i_z = \frac{\alpha q v_z}{2 z_0} \tag{9.11}$$

where z_0 is the axial trap semi-length, α is a geometrical factor of the order of 1. The resulting voltage difference Ri_z induces an electric field in the trap and thus a force that damps the particle energy exponentially over time. The Johnson voltage noise V_n associated with the resistor R $V_n = 4K_B T_R \Delta v R$ (where K_B is the Boltzmann constant, $\Delta\nu$ is the bandwith and T_R is the temperature of the resistor R) determines the limiting energy $K_B T_R$ to which the particle cools. The resulting single particle cooling time constant is τ_r

$$\tau_r = \frac{4 m z_0^2}{(\alpha q)^2 R} \tag{9.12}$$

Tuned circuits with a Q factor of the order of 100 are routinely obtained at room temperature. A higher quality factor of the order of 1000 or more is obtained by building the inductor with superconducting wires. Note that the inductor has to be mounted very close to the trap electrodes inside the cryostat and that the temperature of the circuit has to be 100 mK. The capacity of the tuned circuit is usually the parasitic capacity of the trap electrodes. Assuming as reference values $\nu_z = \omega_z/(2\pi)$= 10 MHz, C= 10 pF, L=25 μ H and Q=1000 then $R = 1M\Omega$ and the cooling time constant is a few tens of ms if $z_0 = 1$ cm (the exact value depends on the exact value of α).

The fact that we have an electron plasma and not a single particle in the Penning trap imposes a further remark. The tuned circuit cools the center of mass motion of the plasma and electron-electron collisions transfer energy from the center of mass to the single particles. The typical expected resistive cooling time is that of the single particle multiplied by $\sqrt{N_e}$. We expect a cooling time constant of the order of $\simeq$ a few tens of seconds with N_e= few 10^5 electrons. The signal induced by the particle motion in the tuned circuit carries information on the number of electrons and indications on their temperature. The RLC circuit thus provides also a powerful, non destructive, diagnostic tool (see the discussion in chapter 10).

9.6 Antiproton cooling with negative ions

A novel technique to obtain ultra-cold antiprotons is based on the use of sympathetic cooling with the interaction of pre-cooled negative ions [131]. Member of AEGIS in Heidelberg are already working (through a funded project) on loading and cooling of negative ions for this purpose.

Negative ions of different species can easily be produced in high numbers (typically more than 10^6) using a sputter-ion source. They can be trapped in a Penning trap and cooled to the environment temperature by means of interaction with a pre-loaded electron cloud. After this pre-cooling phase, the electrons can be removed (or their number strongly reduced) and the ion temperature can be reduced by means of the evaporation of the warmest fraction and/or using a laser cooling technique.

In negative ions, the nuclear attraction is strongly suppressed [132]. Most elements nevertheless form stable negative ions due to the correlation energy, the energy gained when all $Z+1$ electrons adjust their motions such as to minimize the overlap of their wave-functions in accordance with the Pauli exclusion principle (exchange correlation) and electrostatic repulsion (Coulomb correlation). When one of the electrons is excited, it essentially moves around a neutral atomic core. Negative ions therefore have no Rydberg series, but only a few, if any, bound excited states. Until very recently the only bound excited states of negative ions that had been identified had the same parity as the ground state. That means that electric-dipole transitions between them are forbidden and that their absorption cross-sections are correspondingly small. Only a few years ago, the first bound state of a negative ion with opposite parity compared to the ground state was identified in the transition metal osmium [133].

Production of a negative ion plasma

Current designs of high-intensity negative-ion sources are based upon the sputtering of atoms of a desired element from a surface by means of positive ions [134]. Commercially available negative-ion sources of the Middleton type use cesium as the sputtering ion. For example in the case of Os^-, measurements with a standard cathode loaded with osmium powder have shown that osmium readily forms a negative

ion [135]. A current of 10 μA of $^{192}Os^-$ (41% abundance) was easily produced and sustained for many hours. It should therefore be straightforward to load about 10^6 negative ions into a high-field cylindrical Penning trap. With a characteristic trap diameter of 25 mm, a magnetic-field magnitude $|\mathbf{B}| = 1$ T, and a confining electric potential of 10 V, the ions will form a spheroidal plasma typically characterized by a density of few 10^7 cm^{-3}, a plasma radius of about 1 mm and half-length of several mm. A distinct property of the ion cloud will be a rigid rotation about the magnetic-field axis with a typical frequency of some tens of kHz.

After loading, the negative ions will be pre-cooled to the environment temperature with a pre-loaded electron cloud. Apart from being the starting point for additional cooling procedures, this preliminary decrease in ion kinetic energy will also allow avoiding possible auto-neutralization caused by the electric field experienced by the ions as they interact in Coulomb collisions [131].

Evaporative cooling

Once the negative ions have been pre-cooled, the evaporative cooling technique could be used to reduce further the temperature . For negative ions trapped in a Penning trap, the removal of the warmest ions can be achieved not only by lowering the depth of the trap but also by means of selective photo-detachment [136]. One peculiar property of negative ions, with respect to neutral atoms, is that the photo-detachment cross section at threshold is zero and there are no Rydberg series below threshold [132]. Using laser light tuning and thanks to the Doppler effect, it should be possible to selectively photo-detach an electron from the ions whose velocity component along the light propagation direction is larger than a given velocity threshold. If the energy of these selected ions is larger than the initial average energy of the whole cloud, energy redistribution among the ions remaining in the trap will lead to a thermal equilibrium with a lower temperature. Details of this evaporative cooling by laser photo-detachment are discussed in Ref. [136].

Laser cooling

The simplest form of laser cooling is based on the directional absorption of a photon by excitation of an atomic or ionic system, followed by the spontaneous emission of a photon when the system de-excites at some later time. For this "Doppler cooling" [137], the frequency of the light is detuned slightly to the red, or low-frequency side, of the transition frequency f_0 by Δf. Due to the Doppler effect, a photon can therefore only be absorbed by particles moving toward the light source with velocity $v = c(\Delta f/f_0)$, thereby reducing their momentum. The mean momentum transferred in the subsequent isotropic emission is zero; as a result of many absorptions and emissions the particle is cooled. The cooling action is countered by a smaller heating effect due to the spontaneously emitted photons. It limits the temperature that can be achieved with this technique to the Doppler temperature T_D, which is proportional to the natural line-width of the transition.

While evaporative cooling can be used with any species of negative ions, negative osmium is the only known negative ion that has a bound excited state with opposite parity from the ground state and it is therefore the only candidate for laser Doppler cooling. The atomic level diagram of singly negative and of neutral osmium, with the tentative term assignments for the negative ion, is shown in Fig. 9.4, with the excited bound state identified as $5d^6 6s^2 6p^6 D^0 j_a$. The excitation energy of the state was found to be 1.066 eV, which corresponds to a wavelength of 1163 nm while the absorption cross-section was found to be $\sigma_a \approx 6 \times 10^{-16}$ cm^2 . It was deduced that this bound-bound transition is an electric-dipole transition. This transition should be well-suited for the laser cooling of a collection of Os^- ions. With a natural line-width of $\Gamma \approx 10$ kHz, the Doppler cooling limit of the negative osmium ions, and thus in principle also of the sympathetically cooled antiprotons, is $T_D \simeq 0.24\mu$K.

Cooling of Os^- ions from a few K to sub-mK temperatures can be achieved in a few minutes using continuous laser light with a power in the mW range and with a reasonable bandwidth of a few MHz. The bound $^6D^o_a$ state in Os^- can not only decay to the $^4F^e_{9/2}$ ground state but also to some of the intermediate states ($^4F^e_{5/2}$ and $^4F^e_{7/2}$) of even parity. These states are characterized by long lifetimes (fraction of second or few seconds) and this means that the states will probably have to be optically re-pumped to the $^6D^o_a$ state ($\lambda_{5/2} = 3810$ nm and $\lambda_{7/2} = 2290$ nm) [131].

The absorption of a second photon by the ion in the $^6D^o_a$ state leads to a detachment of the extraneous

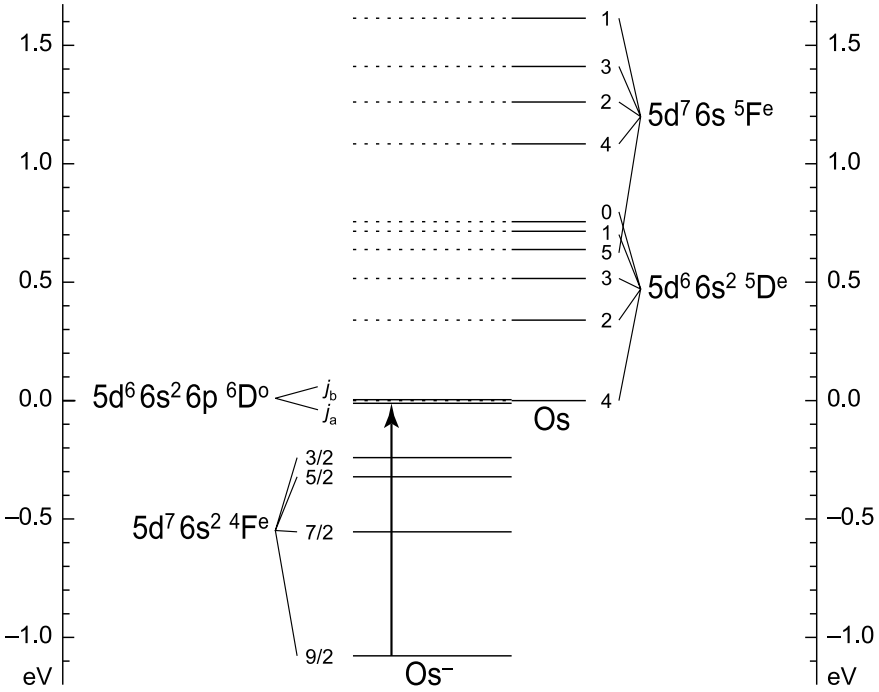

Figure 9.4: Energy level diagram for Os^- (from [131]). The arrow indicates the transition applicable for laser cooling.

electron and neutralization. This process has a cross-section about a factor 10 lower than the resonant excitation to the bound state and constitutes a competing "decay" branch for the ${}^6D_a^o$ state. Depending on the laser power, a fraction of osmium ions can be lost in this way and this mechanism is the main limiting factor on the maximum power that can be used for cooling.

Sympathetic cooling

In the proposed scheme, the antiprotons can be injected into the negative ion plasma just after the pre-cooling with electrons or after a subsequent further cooling of the ions below the environment temperature. During the injection process, the antiprotons will initially carry some kinetic energy. After the injection of the antiprotons into the ion cloud, the temperature of the ion will be reduced further using evaporative and/or laser cooling. The evaporative cooling by lowering the trap depth will also provoke a loss of some antiprotons; for this reason evaporative cooling by means of photo-detachment or Doppler laser cooling are preferable. For example, if the antiprotons will be trapped together with a Os^- cloud during the laser cooling, they can be cooled down to sub-mK temperatures.

The sympathetic cooling process can be described with the formalism used for the equilibration of the temperature in a two-component plasma [130]. The collisional time between antiprotons and ions is not constant during the interaction process but it becomes faster and faster as long as the antiproton energy approaches the ion cloud temperature. For an ion plasma with properties characterized by $n_\mathrm{i} \simeq 10^7$ cm^{-3} and $T_\mathrm{i} \simeq 100$ mK, and for $T_{\bar{p}}$ ranges form 10^4 K down to 100 mK, the characteristic equilibration time falls in the range between fractions of μs up to several seconds.

The equilibrium temperature T_eq will be given simply by

$$T_\mathrm{eq} = \frac{N_{\bar{p}} T_{\bar{p}}^0 + N_i T_i^0}{N_{\bar{p}} + N_i} \simeq \left(\frac{N_{\bar{p}}}{N_i}\right) T_{\bar{p}}^0. \tag{9.13}$$

where $T_{\bar{p}}^0$ and T_i^0 are the initial temperatures of the antiprotons and of the ions, respectively. If a cooling mechanism is added to the process, the temperature of the two species can be further decreased

with respect to the value given by Eq. (9.13). If the heating of the negative ions due to the antiproton injection will turn out to be a problem, some electrons can be left inside the trap in order to bring back the ions to the thermal equilibrium with the surrounding environment or some alternative techniques (like, e.g., adiabatic cooling) can be used before the laser or evaporative cooling processes. In equilibrium conditions, the two species (negative ions and antiprotons) will centrifugally separate into shells due to their different masses [123]. At first sight, this can be viewed as detrimental to the sympathetic-cooling process. However, such a radial separation does not preclude further cooling of one population by the other, so long as the gap between the two species remains small with respect to the damping interaction, which is of course always the case with the Coulomb interaction. Furthermore, the centering of the lighter species is highly desirable, as it leads to a reduction of its rotational velocity. Without this effect, the velocity of particles near the edge of the plasma can be many orders of magnitude larger than the thermal velocities in the co-rotating frame.

Until the antiprotons are fully thermalized they have ample opportunity to be captured into negative ions, and thus be lost irrecoverably. Such loss can occur either by collisional neutralization followed by capture into the neutral atom:

$$\bar{p} + \mathrm{X} \longrightarrow \mathrm{X}^{+}\bar{p} + e^{-} \tag{9.14}$$

or by direct capture according to the reaction

$$\bar{p} + \mathrm{X}^{-} \longrightarrow \mathrm{X}^{+}\bar{p} + 2e^{-} \tag{9.15}$$

Since neutralized atoms rapidly leave the trap subsequent antiproton capture is highly unlikely. Depending on the initial antiproton energy, direct capture may, however, be a source for antiproton loss. In the case of Os, the rate for the direct capture process is essentially zero for center-of-mass energies below 2.5 eV [131]. If some care is taken to transfer the antiprotons without reheating them (*i.e.*, by ballistic transfer or transfer together with electrons), it should be possible to keep the ion temperature well below the threshold temperature of several 10^4 K.

Chapter 10

Detectors in AEGIS

10.1 Introduction

Several types of detectors integrated in the AEGIS setup allow monitoring and step-by-step optimization of the sequence of the various particle manipulations leading to the antihydrogen beam. Some of these detectors are of the type widely used in nuclear and particle physics while others are very common in the atomic and molecular physics community or in the non-neutral cold plasma physics field. In this section we first describe the particle physics detectors. In particular three independent set of detectors will be presented: the *monitor* detectors, the *antihydrogen* detector and the *position sensitive g-measurement* detector. The first two will be devoted to the control of different parts of the experimental setup to diagnose the steps of the production of the antihydrogen beam, while the third will be dedicated to the measurement of the fall of the antihydrogen beam itself. We then discuss field ionization and the power of Rydberg antihydrogen spectroscopy as a diagnostic method of the antihydrogen population. In the last section the plasma detection tools are described.

10.2 The monitor detectors

These detectors will be used to monitor various stages of the preparation of the $\bar{H}$ beam. The first detectors will be dedicated to the $\bar{p}$ beam (*beam counter* and *external beam detectors*), while a second set of detectors (*external monitoring detectors*) will be dedicated to the monitoring of the $\bar{p}$s movements inside the AEGIS apparatus.

10.2.1 Beam counter

The AD will deliver to the Aegis experiments a $\bar{p}$ beam (about 3×10^7 $\bar{p}$'s) with a momentum of about 100 MeV/c (5.3 MeV in energy) in bunches of about 200 ns every 100 s. To monitor the beam intensity and the beam alignment a silicon beam counter can be used. The design can be similar to the one used in the Athena experiment [161], previously adopted by the Crystal Barrel experiment, and that proved to be very useful for the beam diagnostic. It should consist of a 70 μm thick silicon diode, 15 mm in diameter and segmented in 5 pads, each connected to an individual signal line. The voltage required to fully deplete the diode is 4.5 V. The *beam counter* would be located in front of the antiproton catching trap and is able to operate between 10 and 300 K, in a vacuum of $\simeq 10^{-8}$ $mbar$ and in a 3 T magnetic field. The average energy loss of 5.3 MeV antiprotons in silicon has been estimated to be about 11.4 keV per μm of silicon [163], thus around 700 keV for such beam counter. In order to detect the high current generated by such energy loss in the silicon pads, a readout system was developed where the signal current is read directly across a 100 Ω protection resistor and fed into an ADC. The signal from the silicon beam counter can also be used to trigger the $\bar{p}$ catching trap. The 5 pad configuration ensures the possibility of measuring the alignment of the $\bar{p}$ beam, being sensitive to vertical and horizontal displacements of the beam.

10.2.2 External beam detectors

As a further monitor for the beam, a set of two plastic scintillators will be positioned in the vicinity of the beam degrader. In this way the annihilations of the $\bar{p}$ that don't go through the degrader can be measured and thus the beam intensity evaluated. Two modules of plastic scintillator, 1 cm thick and with a surface of (20x10) cm^2 would be coupled to Hybrid Photo Diodes (HPD), since the instantaneous rate will not allow the usage in single particle counting mode [162]. In this way, operating in current mode, the total charge deposited by the annihilation products can be measured and the intensity of the beam extrapolated. These detectors will be connected to ADC modules in order to record the signals coming from the HPDs.

To calibrate the two detectors a dedicated measurement of beam absorption must be performed. A target material (aluminum foil) is positioned in place in the beam line, close to the degrader, and is activated by the beam, while the two detectors measure the annihilation products. By measuring, after extraction, the target material activation and comparing it with the detector measurements, a calibration HPD counts/beam intensity can be established [164]. Previous measurement in the ATHENA experiment proved that the HPD can fully operate in a magnetic field.

10.2.3 External monitoring detectors

All along the path from the degrader to the g-measurement region, including the $\bar{H}$ production region, we intend to place plastic scintillators to detect the products of $\bar{p}$ annihilations. In this way we can monitor each phase of the $\bar{H}$ beam production and manipulation. Such detectors would be (70x30) cm^2 in surface and 1 cm thick, positioned vertically outside the the AEGIS apparatus setup, as close as possible to the central z-axis of the experiment. Given the size of the setup a total of 12-16 scintillators can be foreseen. Unlike the beam detectors, given the annihilation rate and the solid angle coverage, these detectors can be used to detect single particles, and thus can be coupled to standard photo-multipliers, two per scintillator to allow pairwise coincidences and thus reduce random noise, and read out by VME ADC modules.

10.3 The antihydrogen detector

The final goal of AEGIS is the production of an $\bar{H}$ beam for the measurement of the acceleration due to gravity. To achieve such an objective, $\bar{H}$ must be produced in a stable way and we believe that an antihydrogen detector is thus essential to monitor and diagnose the processes involved. It would allow 3-D imaging of the $\bar{p}/\bar{H}$ annihilation ([165]) and thus the monitoring of $\bar{p}/\bar{H}$ losses and $\bar{H}$ production. The presence of the antihydrogen detector, together with the pulsed antihydrogen production scheme allows a direct measurement of the antihydrogen velocity after its production.

The time of production of antihydrogen is known to the uncertainty in the arrival time in the antihydrogen cloud of the Rydberg positronium ($\sim 1\mu s$). With a velocity of 100 mK of $\sim$ 40 m/s, a distance to the nearest surface of 1 cm, and an expected production rate of $\sim$ 100 atoms, the $\bar{H}$ annihilation time distribution covers a range of $\sim$ few hundres μs, during which $\sim$ 100 annihilations take place. A single hit time resolution of $\sim 1\mu s$ will then allow measuring the velocity distribution of the ensemble of produced $\bar{H}$ atoms.

The antihydrogen detector must be able to recognize both antiproton and positron annihilation, thus it must be designed to allow the tracking of charged particles and the detection of 511 keV γ's. This can be achieved by using the design of the ATHENA antihydrogen detector (see Fig. 10.1 and Fig. 10.2), that proved to be so important for the success of the experiment. In a cylindrical geometry, and moving out radially from the center, two layers of 12 μ-strip modules were followed by 16 rows of 12 CsI crystal each (for a total of 192 crystals). The inner diameter was of about 7.5 cm, close to the inner layer of μ-strips modules, the outer diameter 14.0 cm, in the vicinity of the CsI crystal; the total length would be 25,0 cm. Such a detector can work efficiently in an environment of 140 K as previously experienced by the ATHENA experiment [166]. The overall dimensions have to be modified to fit the AEGIS final configuration.

Charged particles can be detected in the two layers of Si-μ-strips covering about 80 % of the solid angle. A three dimensional reconstruction of the $\bar{p}$ annihilation vertex can be achieved with a $\sigma = 4mm$

spatial resolution and with an efficiency close to 100 % by straight line extrapolation of the charged particle tracks. Photons from positron annihilation can convert in the 1.7×1.7×1.3 cm^3 CsI crystals via photoelectric effect with a probability of about 25 %.

Without entering into details the μ-strip modules could consist of two double sided sensors, 380μm thick and 8.2×2 cm^2 in size, glued onto a silicon mechanical support (see [164] and [167]). For what concerns the 511keV γ's detection pure CsI scintillation crystals have been considered, since they ensure efficiency and satisfactory light yield at low temperatures ([164] and [166]). These crystals would be coupled to avalanche photo diodes (APD), such as Hamamatsu APD type S8148, to ensure a good signal-over-noise ratio.

For readout, based on our experience in ATHENA, we plan to use the VA2_TA chip, which is based on a series of CMOS VLSI chips (Viking [168], VA), both for the silicon detectors and the crystals. Through repeater cards, the chips would be connected to VME modules (Caen V551B sequencer and Caen V550 ADCs). In such a configuration and with zero suppression, a 200 Hz rate would lead to 70% readout efficiency, the readout dead time being dominated by the MXI2 bus speed.

In summary, the AEGIS $\bar{H}$ detector has been designed to ensure the detection of $\bar{p}$ annihilations with an efficiency close to 100 % and the detection of $\bar{H}$ annihilation with an efficiency of about $(25\%)^2 \simeq 6\%$.

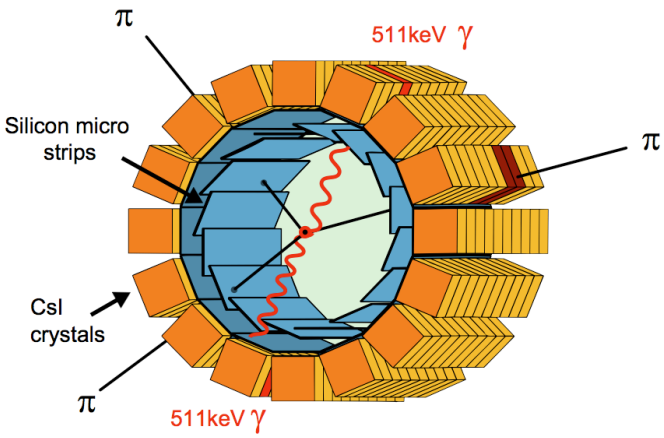

Figure 10.1: Schematic view of the antihydrogen detector

10.4 The position sensitive g-measurement detector

The requirements on the position sensitive detector able to measure the antihydrogen vertical coordinate and its arrival time are discussed in chapter 3. A position resolution of 10-13 μm is required to ensure a 1% uncertainty on the gravity determination. Given the geometrical dimensions of the Moiré deflectometer region, a detector with a 20×20 cm^2 sensitive region is desirable. The detector should also be fully operational at a temperature of at most 140 K.

Given such requirements, a Silicon μ-strip detector has been considered to be the best option. Monte Carlo simulations have been performed to study the resolution achievable on the annihilation point in a 300 μm thick silicon strip detector alone, notwithstanding the possibility of improving the vertex resolution through the addition of further detector planes (to reconstruct pions from the annihilation) behind the first one.

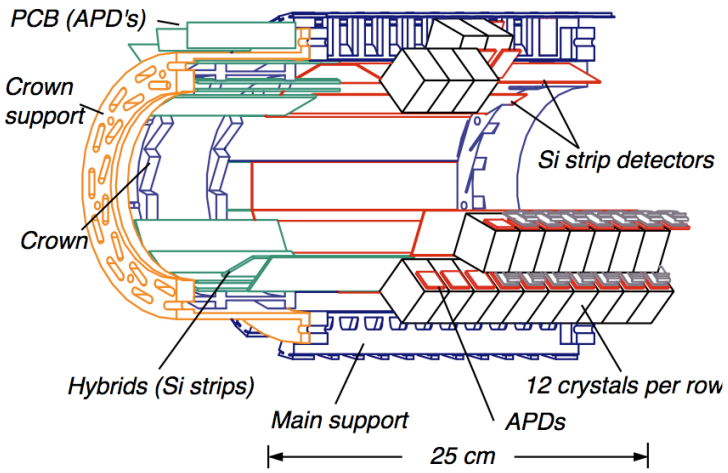

Figure 10.2: Three-dimensional drawing of the antihydrogen detector

10.4.1 $\bar{H}$-Si annihilation Monte Carlo Simulations

The simulations (using the GEANT 3.1 code) consist of antiprotons annihilating at rest on a a 20x20 cm^2, 300 μm thick silicon slab, composed of 8000 25 μm wide, 20 cm long horizontal strips (in order to measure the vertical position). The annihilation of an antiproton with a proton of the ^{28}Si nucleus produces charged and neutral pions. The remainder of the ^{28}Si nucleus (^{27}Al) can then undergo two different processes: it can recoil or it can disintegrate into a ^{12}C, 3 α particles and a tritium (in the following *heavy fragments*). The relative weight of the two different final states can be changed from 0 (only nuclear recoils) to 1 (only nuclear disintegrations).

In Fig. 10.3 the energy released in each hit strip by π's (a), heavy fragments (b) and ^{27}Al recoil nuclei (c) is shown. The π's and the heavy fragments can travel, on average, a few hundred μm, while the ^{27}Al recoil nucleus stops in a few μm. The results are in qualitative agreement with the model of [169].

Since the $\pi's$ and the heavy fragments can deposit energy over many strips, a procedure to obtain the position of the antiproton annihilation must be used. The most intuitive algorithm is the *center*

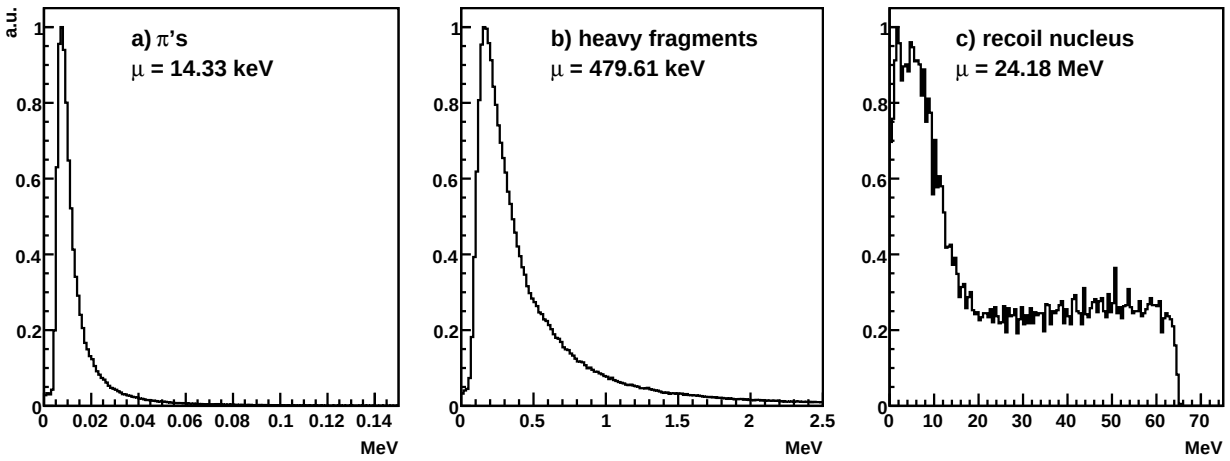

Figure 10.3: Energy released by π's (a), heavy fragments (b) and ^{27}Al recoil nuclei (c) in each hit strip of the 300 μm thick silicon detector.

of gravity, in which the particle position can be estimated as the weighted average of the positions of the n strips. This method however results in a bad resolution in our case, since the $\pi's$ and the heavy fragments can travel a few hundred μm and thus introduce a large uncertainty in the annihilation point reconstruction. A more complex procedure is the so-called η algorithm (well described for example in [170, 171, 174, 176]). This method works very well when the number of strips with signal is small (2, 3 or 4). To apply such a method to our case, a cluster finding procedure is first applied to localize the *hot spot* of the few strips on which we use the η algorithm. A simple *digital algorithm*, selects the strip which exhibits the biggest signal as the position of the antiproton annihilation. This method works perfectly well when we force the ^{27}Al nucleus to recoil, leading to a resolution[1] of $\simeq 7\mu m$ (as expected from the formula *strip pitch*$/\sqrt{12}$) with nearly 100% efficiency. In the case of ^{27}Al nucleus disintegration the procedure still works sufficiently well if we require that the second more energetic strip exhibits less than 60% of the most energetic strip. In this case a resolution of 10 μm is obtained with $20-25\%$ efficiency. In Fig. 10.4 we report the resolution obtained when generating 50% recoils and 50% disintegrations ($\sigma \simeq 8.6\mu m$) with an efficiency of about 60 %. The application of a more complex and sophisticated position finding algorithm, in presence of nuclear disintegration, can surely improve the efficiency and also the resolution. This could lead to a detector with a strip pitch of 25 μm and a readout pitch of 50 μm, which would reduce the number of readout channels and thus the overall cost of the detector.

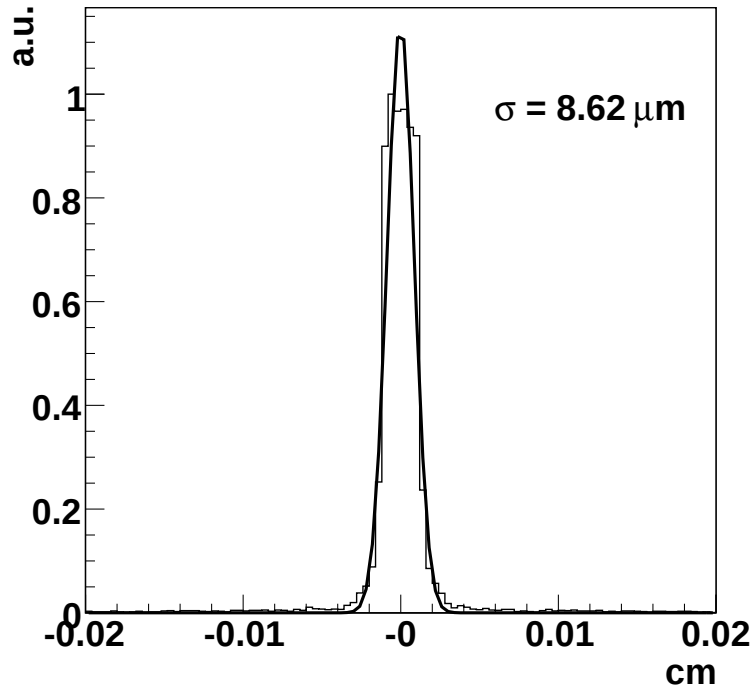

Figure 10.4: Distribution of the difference between the MC generated $\bar{p}-^{28}Si$ annihilation point and the reconstructed value (using the *digital algorithm*). The spatial resolution is given by the σ of the superimposed fit to a Gaussian distribution.

A single-sided silicon microstrip detector consisting of 20 cm long strips (60 cm long strips have been successfully constructed and used [175]) with a strip pitch of 25 μm and readout pitch of either 25 μm or possibly 50 μm (as in [173]) would thus meet the 10 μm spatial resolution requirements of AEGIS. This translates into a total number of 8000 strips and 4000 (or 8000) readout channels (required to cover a 20x20 cm^2 area). In recent years extremely good resolutions have been reached, down to a few μm (e.g. [170, 171, 172, 173, 174]), with similar detectors. This spatial resolution can be further improved upon

[1] As resolution we mean the σ of the Gaussian function with which we fit the distribution of the difference between the Monte Carlo generated $\bar{p}-^{28}Si$ annihilation point and the reconstructed position.

by implementing two additional planes of silicon strip detectors behind the first plane, with which the trajectories of pions from annihilating antihydrogen atoms can be reconstructed, and constrained to lie on the surface of the first detector. The combination of techniques leads to an overall resolution on the impact point of an antihydrogen atom on the first detector of better than the required 10 μm.

10.5 Detectors for positronium

Ground state positronium emitted from the converter with the velocity of interest for AEGIS (few 10^4 m/s) will travel in vacuum over several mm and a large fraction of it will decay before reaching the trap electrodes. The time spectrum of the emitted γ's will show a large component decaying in time with the typical 142 ns lifetime of O-positronium. This time spectrum is the signature of positronium formation and the number of counts provides a quantitative information about the actual positronium yield. The start signal is given by the time when the bunch is accelerated onto the target. A scintillator with a fast (few ns) time response connected to a fast photomultiplier (or to a MCP-photomultipler) will be used to detect the γ's. A possible choice of scintillator material is PbF_2. The anode signal will be connected to a fast digitizer allowing to record in a single shot the entire lifetime spectrum ($\simeq 10^8$ positrons hit the target within about 10 ns). This procedure has been already demonstrated in [180].

The time length of the positron bunch will be measured by detecting the signal induced on one of the trap electrodes in the positron branch by the passage of the cloud.

The laser excitated positronium has a lifetime longer than that of the ground state by orders of magnitude (see Chapter 12) and it will annihilate when hitting the trap electrodes. The component in the time spectrum corresponding to the O-Ps decay time constant of 142 ns will be reduced. Ideally, in the case of 100% excitation efficiency it should disappear altogether. The comparison of the time spectra with and without laser excitation provides a measurement of the excitation efficiency.

In addition, the excited positronium will be detected by field ionization using the various trap electrodes to apply an electric field. Electrons or positrons resulting from the field-ionized positronium will be trapped and then counted by dumping them on the Faraday cup or the MCP mounted on the AD side of the AEGIS apparatus.

10.6 Diagnostic through Rydberg Anti-hydrogen spectroscopy

As listed in Table 5.1, the spacing between adjacent Rydberg states at $n = 30$ is $\sim 1 \times 10^{-3}$ eV ($\sim$ 260 GHz) and therefore corresponds to a transition frequency in the mm-wave range of the electromagnetic spectrum. Transitions of this kind between neighboring or near-neighboring Rydberg states can be driven very efficiently because of their large transition dipole moments which scale as n^2. The low frequency of these transitions implies that the effect of Doppler broadening is minimal. In an environment in which external fields are homogeneous a very high spectral resolution can be obtained provided the interaction time between the Rydberg atoms and the mm-wave radiation is long. However, the sensitivity of high Rydberg states to external perturbations means that even small field inhomogeneities can cause large inhomogeneous broadenings and thus reduce the achievable resolution [80]. This sensitivity to field inhomogeneities can however be taken advantage of to obtain information on the field distributions and also, as measured in Ref. [80, 81], the density of charged particles in the measurement volume.

With these points in mind mm-wave excitation may be employed in the AEGIS experiment to characterize the combined fields due to the magnet, the trapping electrodes and the charged particles present in the $\overline{\mathrm{H}}$ production region. By accurately determining the fields and their inhomogeneities experienced by the Rydberg $\overline{\mathrm{H}}$ following charge exchange with the Rydberg positronium, information of particular importance for the formation of a $\overline{\mathrm{H}}$ beam by Stark acceleration can be obtained.

In addition to the need to accurately determine the electric and magnetic fields in the $\overline{\mathrm{H}}$ production volume, it will also be crucial for the Stark acceleration process to characterize the distribution of excited Rydberg states produced following charge exchange. This may also be achieved by mm-wave spectroscopy combined with state-selective electric field ionization. The technique of state-selective electric field ionization (SFI) will be discussed in more detail below (section 10.7) with regards to particle detection. Rydberg Stark deceleration experiments recently performed at ETH Zürich on beams of hydrogen atoms traveling with initial velocities of ~ 750 ms^{-1} have demonstrated a wide acceptance of Stark states with

a range of principal quantum numbers in a two-dimensional trap [87]. These results indicate that in the reverse process, Stark acceleration, which will be employed in the AEGIS experiment it should be possible to accelerate $\overline{\mathrm{H}}$ atoms in a range of Rydberg states to form a beam, rather than accelerating only those atoms in one particular $|n, k\rangle$ state. However, it will remain necessary to determine experimentally the distribution of states to be Stark accelerated so as to properly optimize the acceleration electric field gradient and its time dependence.

In order to obtain the maximum efficiency and minimum longitudinal temperature when producing the $\overline{\mathrm{H}}$ beam by Stark acceleration it would be desirable to minimize the range of Rydberg states populated prior to acceleration. This may be done by driving mm-wave transitions to lower n states so as to modify the distribution of excited states and in turn enhance the control which may be achieved when forming a $\overline{\mathrm{H}}$ beam.

Finally, the spectroscopic study of the crossings between Rydberg Stark states of H and $\overline{\mathrm{H}}$ as a function of electric field strength (with or without a magnetic field) may yield new insights into the symmetry properties of these atoms. The spherically symmetric $1/r$ Coulomb potential surrounding the proton or anti-proton gives rise to exact crossings between neighboring electronic states as the field induced energy shifts increase. These crossings become avoided when spin-orbit effects and other interactions are taken into account. The high spectral resolution which can be achieved in mm-wave excitation, in combination with acceleration/deceleration experiments, may lead to new insights into this problem.

10.7 Electric field ionization

Due to its very high efficiency and state selectivity, pulsed electric field ionization of Rydberg atoms is often employed as a detection tool in atomic and molecular physics [79, 88]. When a pulsed electric field is applied to ionize a field-free Rydberg atom, one side of the Coulomb potential in which the Rydberg electron is localized is raised in energy and the other is lowered as can be seen in Figure 10.5. Viewing this picture from a classical perspective it is clear that ionization will only take place if the Stark saddle point is lowered by the ionization field to below the energy of the excited Rydberg state. Since the ionization field for Rydberg states decreases rapidly with n as listed in Table 5.1, if sufficient care is taken, one can apply an ionization field that will only ionize Rydberg states above a particular principal quantum number, hence electric field ionization can be a state selective method of Rydberg particle detection.

Within a manifold of Stark states, such as that illustrated schematically in Figure 5.1, the electron density of the negative k Stark states is greatest on the side of the Coulomb center on which the Stark saddle point lies, with the positive k states having the greatest electron density on the opposite side of the Coulomb centerer. As a result the negative k states ionize at lower fields than the positive ones. Indeed the field required to ionize the extreme positive k states is typically twice that required to ionize the extreme negative k states. As a result, along with the possibility of identifying the principal quantum numbers of excited Rydberg states by selective field ionization, it is also possible to determine approximately their location within the Stark manifold.

For Eq. 5.1 to provide a valid description of the energies of the Stark states associated with a Rydberg state of principal quantum number n, the crossings which occur between Stark levels at high fields must be exact, or the slew rate of the rising edge of the ionization field must be large enough that they are traversed diabatically. The Rydberg Stark levels in a purely Coulombic potential cross exactly in a Stark map because the Runge-Lenz-Pauli vector is a constant of the motion [79, 179]. When spin-orbit and other small effects are taken into account the crossings become slightly avoided with the possibility of adiabatic crossings at sufficiently small slew rates. In hydrogen, field ionization occurs diabatically in the case of high-n or high-m states and for ionization pulses which rise on a time scale of a few 10's of nano-seconds. However observing non-adiabatic effects in the field ionization of H and $\overline{\mathrm{H}}$ Rydberg levels is an intriguing possibility, as was discussed in Section 2 in the context of the mm-wave spectroscopy experiments.

From a quantum mechanical perspective, the electron can tunnel ionize before the Stark saddle point is shifted below the energy of the excited Rydberg state, however the rate for tunnel ionization decreases rapidly as the electric field strength is reduced. Thus if the ionization electric field is pulsed with pulse durations shorter than the tunneling time (i.e. pulses of a few 10's of nano-seconds duration) the classical picture described above holds and efficient state selectivity can be maintained.

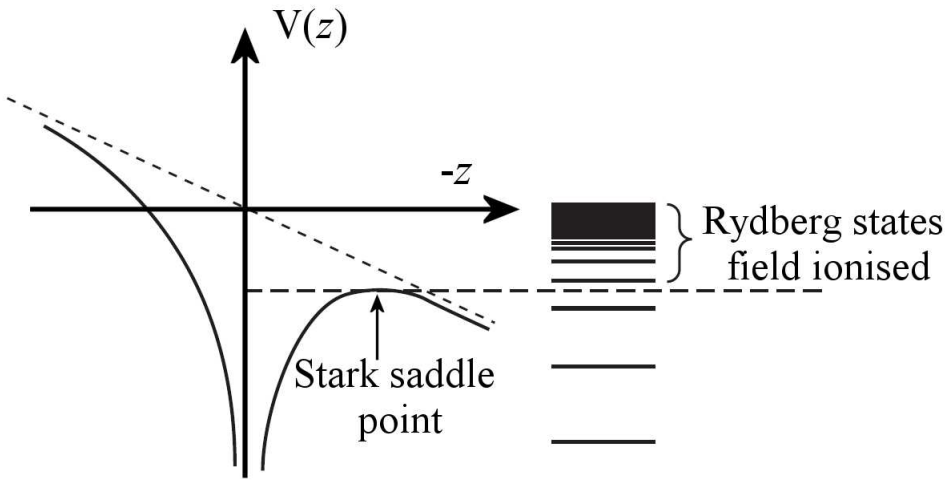

Figure 10.5: Static potential energy curve for a hydrogen atom in an electric field acting along the negative z-axis. The ionization of states with field-free energies above the Stark saddle point is indicated on the right (after reference [88]).

The charge exchange method which will be used in the AEGIS experiment to produce $\overline{\mathrm{H}}$ is expected to result in the population of a broad distribution of Rydberg states. It will therefore be important to characterize this distribution of states prior to Stark acceleration and $\overline{\mathrm{H}}$ beam formation. This may be done using a similar pulsed field ionization technique to that described above, but with a longer ramped electric field [79, 178]. From the arguments outlined above with regard to the electric field ionization process, Rydberg states of different principal quantum number will ionize at different electric fields. Therefore if one ramps up the ionization field strength at an appropriate rate and records the arrival time of the resulting antiprotons on a charged particle detector one will observe a series of time-of-flight maxima each corresponding to a Rydberg state of different principal quantum number. This technique may therefore be used in conjunction with mm-wave spectroscopy to determine the distribution of excited states of $\overline{\mathrm{H}}$ following charge exchange.

10.8 Plasma modes diagnostic

The thermal equilibrium state of a large number of positrons or electrons confined in a Penning trap at low temperature is a rigidly rotating spheroidal plasma [151] with a sharp boundary. Models predict that the density is almost constant within the ellipsoid and that it falls off exponentially with the Debye length at the plasma boundary.

Knowledge of the characteristics of the plasma (i.e. dimensions, density) can be obtained by means of a non-destructive method based on measurement of the first two axial electrostatic mode frequencies (dipole, quadrupole) [152, 153].

The modes are excited by applying sinusoidally time-varying potentials to one trap electrode, while the plasma response can be measured by acquiring the induced current on another electrode (see figure 16). The ratio of the induced current to the excitation amplitude is measured as a function of the drive frequency. A narrow step-wise frequency sweep (4 ms duration per 5 kHz step) is usually made across the resonant frequency of each mode. For each frequency step, the amplitude and phase (relative to that of the drive signal) of the voltage induced by the plasma motion is acquired. This excite-detect process can be performed by means of a network analyzer integrated with suitable attenuation and amplifying circuits. The cross talk signal between the transmitting and receiving electrodes is acquired without particles and subtracted from the signal measured with the plasma present. In addition high sensitivity, low noise custom circuitry has been developed for this purpose by members of AEGIS.

A detailed and simple analytic theory of the electrostatic modes in non-neutral plasmas exists [152]. In the framework of this theory the frequencies of the first two symmetric axial modes depend on the

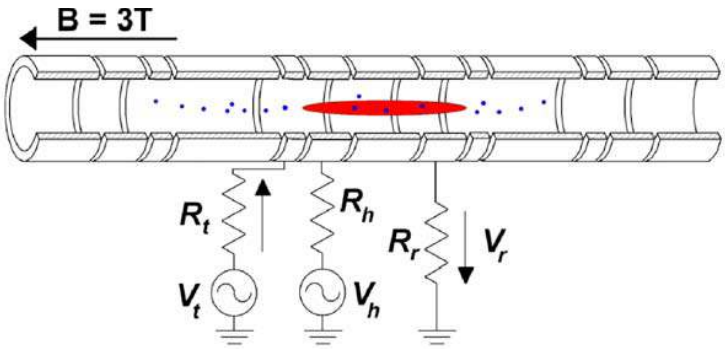

Figure 10.6: Schematic diagram of a Penning trap with the modes analysis and heating circuit

plasma size, density, and temperature. The zero temperature model is used to determine the plasma density and the ratio between the axial and radial extension of the plasma.

Moreover the exact plasma response (see Fig.10.7) can be modeled using a resonant circuit analogy, where the values of the components are related to the plasma properties. The diagnostic also allows, in addition to the the previous parameters, the plasma length ($2z_0$) to be obtained. The radius (r_0) and the particle number (N) are then determined and a complete nondestructive diagnostic system is obtained [155, 156]. Temperature shifts produced by the application of a radio-frequency signal resonant on the (1,0) mode are monitored as changes in the (2,0) mode frequency. The model [154] is used to calculate the induced temperature increase.

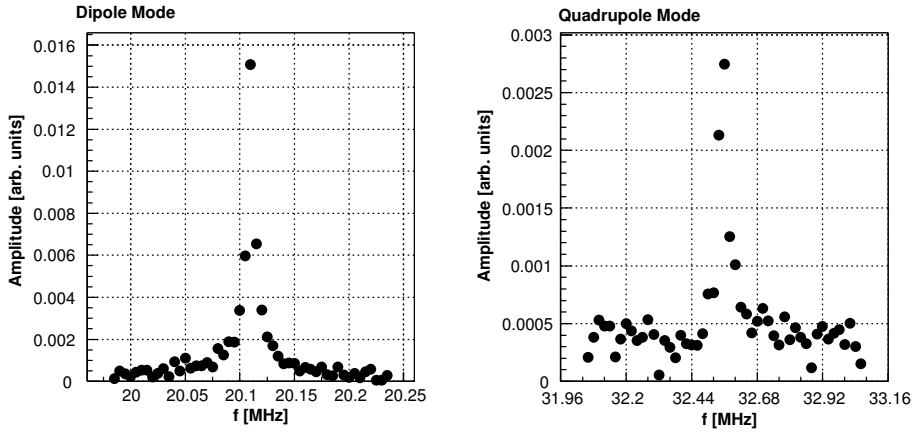

Figure 10.7: Measurement of the amplitude of the first two low-order axial modes as a function of the drive frequency. In this case the measured plasma parameters are $n = 6.3 \cdot 10^7$ cm^{-3}, $z_0 = 2.0$ cm, and $r_0 = 0.1$ cm.

10.9 Particle detection with tuned circuits

The electric signal induced by the electron motion on the circuit tuned to the axial frequency is read using a low noise cryogenic amplifier. This signal contains information about the number of electrons and their temperature. A measurement of the electron temperature in the range of Kelvin and below is very difficult mainly because the equivalent noise temperature of the amplifier is higher than the final particle temperature that we want to reach (100 mK). The amplifier has to be switched off during the resistive cooling process. With the amplifier on, the electrons will reach a temperature equal to the amplifier noise temperature. Neverthless the frequency spectrum of the voltage signal measured with the tuned circuit has a shape that can be easily modeled as described in [177] and its analysis allows to measure the number of electrons. In the absence of electrons the tuned circuit frequency spectrum $S(\omega)$ shows the familiar Lorentzian shape

$$S(\omega) \propto \frac{(\Gamma/2)^2}{(\omega_z - \omega)^2 + (\Gamma/2)^2} \tag{10.1}$$

In presence of electrons a dip at $\omega = \omega_z$ appears together with two peaks. Roughly speaking the distance of the two peaks is related to the number of electrons. More precisely, the shape of the spectrum can be fitted with a known function [177] and the number of electrons is measured in a nondestructive way. Examples of the expected signals are shown in figure 10.8. These types of signals are routinely detected with light particles in Penning traps and, with some particular care, they can also be observed with heavy particles.

10.10 Faraday cup and imaging detectors

We will install a a particle imaging detector composed of a MCP coupled to a phosphor screen on the AD side of the fringe field region of the magnet, outside of the cryostat. The gain of the MCP can be adjusted to detect single particles, as well as bunches with a large number of particles. This device provides a measurement of the radial size (integrating over the axial dimension) of the bunches dumped on it. A resolution of $\simeq 100$ μm can be easily achieved. Particles dumped from any of the traps located in the main magnet can be detected because the magnetic field ensures radial confinement. The additional Faraday cup signal provides a measurement of the total number of particles and it allows in-situ calibration of the MCP gain. The minimum number of particles detected by the Faraday cup is limited by the electronic noise. Without any particular care, a sensitivity of a few 10^5 electrons can be achieved.

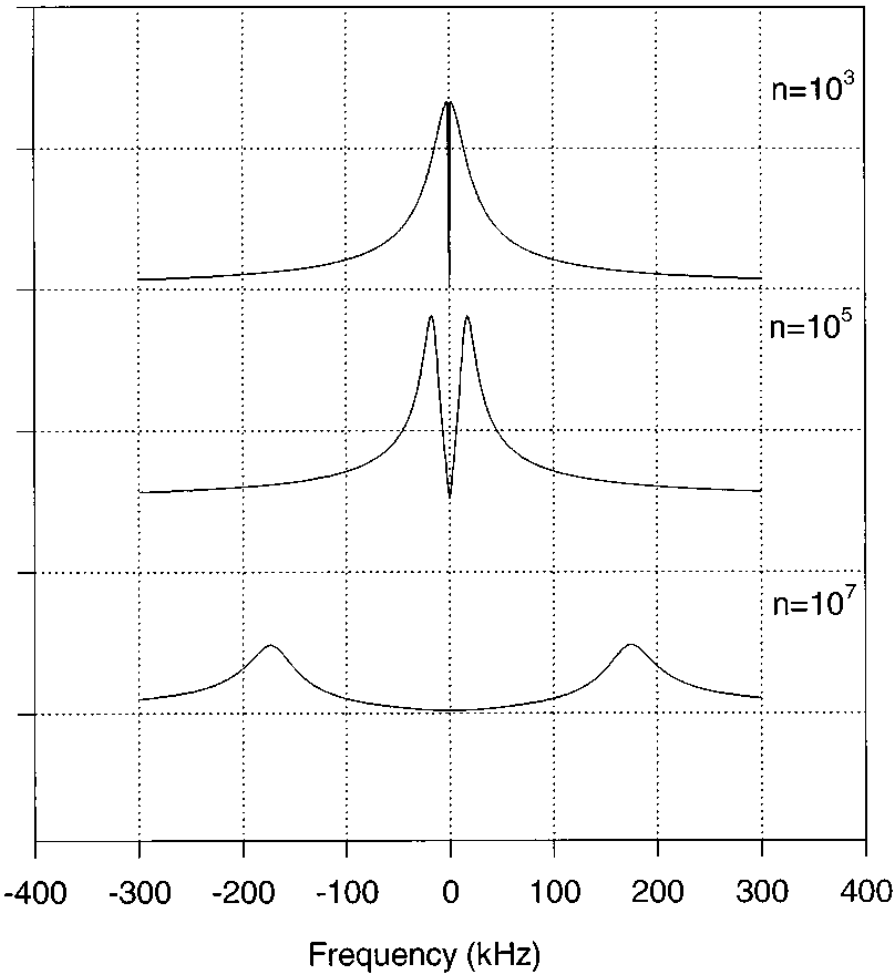

Figure 10.8: Calculation of the shape of the RLC resonance with 10^3, 10^5, 10^7 stored electrons ([177]

Chapter 11

Antiydrogen production and beam formation

11.1 Expected number of antiatoms

We assume that $N_{\bar{p}}$ antiprotons are prepared in an elliptical cloud with radius r_p and half length z_p with uniform density $n_{\bar{p}}$. As previously discussed $r_p \simeq 1$ mm and $z_p \simeq$ 1-2 cm. In the geometry of figure 7.11 the positronium is emitted from the target with a spot size given by the positron plasma radius ($\simeq 1$ mm) and it emerges isotropically from the target itself. We call d_t the distance between the mean value of positron impact point on the target and the center of the antiproton cloud. The number of produced antihydrogen atoms $N^*_{\bar{H}}$ is

$$N^*_{\bar{H}} = N_{Ps^*} * n_{\bar{p}} < \sigma v_{Ps^*} t_X > \epsilon_{Ps^*\bar{p}} \tag{11.1}$$

where $< \sigma v_{Ps^*} t_X >$ indicates the averaged value of the product between the cross section σ, the positronium velocity v_{Ps^*} and the time t_X to cross the antiproton cloud. This product can be approximated by $\sim 2\sigma r_p$; $\epsilon_{Ps^*\bar{p}}$ is a geometrical overlap factor between the antiproton and the positronium clouds. In the naive case where $\epsilon_{Ps^*\bar{p}}$ is simply due to the geometry of fig 7.11 we have

$$N^*_{\bar{H}} = N_{Ps^*} N_{\bar{p}} \frac{\sigma}{4d_t^2} \tag{11.2}$$

Considering that several AD shots can be stacked and that re-use of antiprotons that have not recombined into antihydrogen can be implemented, we will assume that once a stable regime of working conditions has been reached, we have 10^5 cold antiprotons waiting for positrons.

The cross section value for n_{Ps} in the interval 20-35, depending on the positronium velocity, can assume values from 10^{-8} to 10^{-9} cm^2.

If $5 \cdot 10^6$ positronium excited atoms are available then the expected number of antihydrogen atoms ranges from $\simeq 100$ to $\simeq 1000$ if $d_t = 1$ cm. Considering that the time necessary to produce the particles is of the order of some hundreds of seconds the expected production rate (averaged over a day) is in the range of a few Hz. This value matches the requirements on the necessary number of particles for the gravity measurement.

The choice of the best value of the positronium excitation level n will be based on the experimental results and it is a compromise among different requirements: considerations on the lifetime of the Rydberg levels and on an optimization of the Stark acceleration process suggest choosing a low Rydberg level, while maximizing the antihydrogen production rate requires a high Rydberg level.

11.1.1 Positronium focusing on the antiproton cloud

One of the limitation on the achievable antihydrogen production rate is the poor geometrical overlap between the antiproton and positron clouds. Due to this poor overlap, only a small fraction of the Rydberg positronium intersects the antiproton cloud volume. The sensitivity of the Rydberg positronium

to electric field gradients and the design of AEGIS, allows the possibility of focusing the positronium cloud emerging from the target onto the antiproton cloud. Referring to figure 7.11 and recalling that the antiproton cloud radius is of the order of 1 mm while its length is of the order of 1 cm, to focus the Rydberg positronium it is necessary to create an electric field gradient that confines the motion of the Rydberg positronium in one direction (that here we call y') within about 1-2 mm while the positronium moves by about $\simeq$ 1 cm in the other directions. This can be achieved by placing a few properly shaped electrodes between the target and the trap. A rough evaluation of the necessary electric field in the y' direction is obtained by assuming a uniform gradient of the electric field modulus. The deceleration a must be such that the distance Δytraveled in the y' direction is of the order of 1 mm during the time $t_d = d/(v_{Ps^*})_x$ in which the Ps^* freely travels for about 1 cm in the other directions.

$$\Delta y = (v_{Ps^*})_y t_d - \frac{1}{2} a t_d^2 \tag{11.3}$$

and from this relation it follows

$$a \simeq \frac{2 v_{Ps^*}^2}{d} \tag{11.4}$$

$a \simeq 1.810^9 m/s^{-2}$ if $v_{Ps^*} = 3 \cdot 10^4 m/s$ Acceleration of this order of magnitude can be obtained with electric field gradients of a few hundred $Volts/cm^2$ on Rydberg positronium excited to the maximum allowed values of k. The maximum gain factor is about 10, corresponding to focusing all the positronium on the antiproton cloud. Even a gain factor of the order 2-3 will be of great help.

11.2 Measurement of the antihydrogen velocity

Taking into account the considerations of the previous chapters we expect that the antihydrogen initial velocity is of the order of several tens of m/s and it should be approximately isotropic. The time distribution of the produced antihydrogen is determined by the time needed by the positronium to cross the antiproton cloud volume and it is of the order of several tens to a few hundred ns. While the time to prepare the antiproton and positronium clouds is of the order of some hundreds of seconds, the antihydrogen production happens in a pulsed mode. The formation time is well defined and it allows to measure the produced antihydrogen velocity by using the antihydrogen detector located around the formation region and measuring the time of flight of the antihydrogen. If no accelerating electric field is applied after antihydrogen formation, the antiatoms fly towards the trap electrodes and annihilate there. As a reference an antihydrogen atom with a velocity of 50 m/s takes 200 μsec to travel a distance of 1 cm. The start time is given by the positronium laser pulse excitation and the stop time for every detected antihydrogen is provided by the detector itself. In addition, as already exploited in ATHENA [126], the shape of the axial annihilation distribution provides information on the (an)isotropy of the velocity distribution.

11.3 Antihydrogen beam formation

As discussed in chapter 4 we expect to produce antihydrogen with a distribution of quantum number n and l or, in an equivalent way, with a wide distribution of the quantum numbers n and k. The beam is obtained by applying to the radial sectors of the trap electrodes appropriate voltages immediately after the formation of antihydrogen in order to create an electric field gradient accelerating the atoms towards the exit of the magnetic field and the gratings of the Moiré deflectometer. The choice of an electric field whose amplitude e.g. decreases when going from the trap toward the gratings, leads to antihydrogen atoms with quantum number $k > 0$ being accelerated toward the gratings, while those with $k < 0$ are pushed in the opposite direction. An appropriate design of the electric field's spatial and temporal behavior will allow recovering also the atoms with $k < 0$. The accelerating electric field should not increase the antihydrogen radial velocity; some optimization of the design of the accelerating electrodes and voltages has been performed to achieve this result. The accelerating electrodes are constituted by those of the antihydrogen formation trap, together with some neighboring electrodes. The cylindrical electrodes are radially cut into four sectors. Two of them have an angular extension of 135^0 degrees, the other two of 45^0.

Before and during the interaction between antiprotons and positronium, the voltages applied to the electrodes are those needed to generate a Malmberg or Penning trap. Immediately after the interaction (the time is defined to within some tens of ns) the voltages of the electrodes are quickly switched to transform the trap into a cylindrical Rydberg accelerator. In this configuration a voltage $+V_0$ is applied to one of the big radial sectors while a voltage $-V_0$ is applied to the one opposite to it; the intermediate electrodes are grounded. The V_0 values used for different electrodes decrease with increasing z. The electric field direction is almost perpendicular to the magnetic field and there is a strong axial gradient of the electric field modulus.

As an example, figure 11.1 shows the electric field modulus as a function of z on the trap axis; this is part of a simulation of the acceleration of Rydberg antihydrogen with mean quantum number n=30. Here $z = 0$ is the center of the Penning trap. The electric field is varied with time during the acceleration, as has been done in experiments on hydrogen atoms at ETH Zürich. The figure shows three time steps. The acceleration takes place in a short distance (few cm) in the uniform magnetic field. After an appropriate time (80 μsec with n=30) the electric field is switched off and the antihydrogen atoms continue to fly towards the end of the magnet bore.

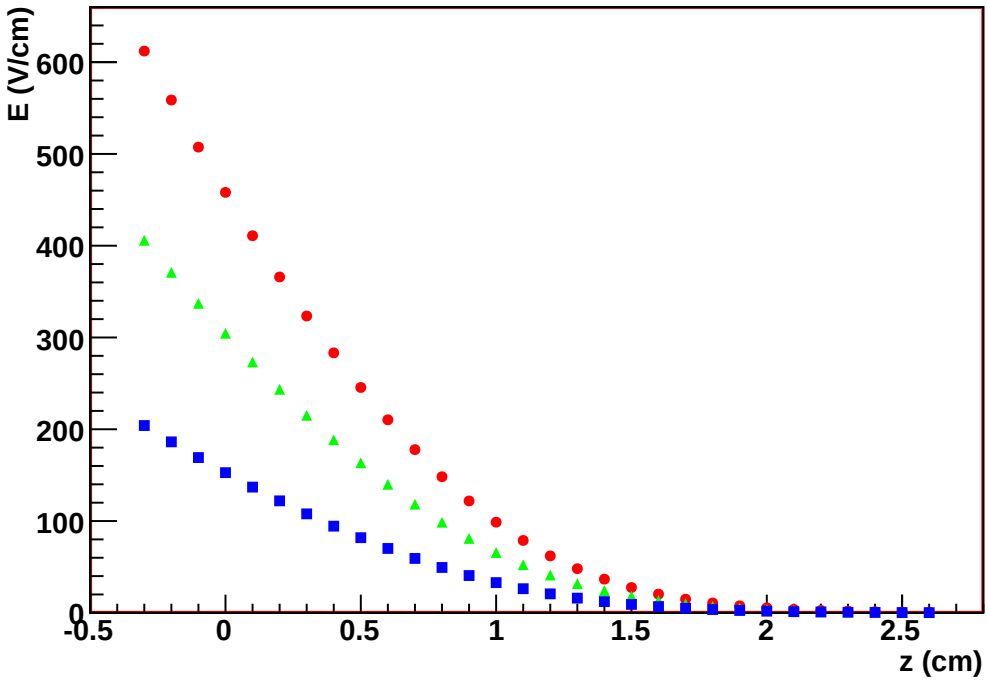

Figure 11.1: Electric field modulus (V/cm) as a function of z(cm) on the trap axis. The plots show the field at three different times. z=0 is the center of the antihydrogen cloud.

The force F_E experienced by a Rydberg atom in a given electric field is related to the gradient of the electric field modulus f by (in atomic units)

$$\vec{F_E} = \frac{3}{2} nk \nabla f \tag{11.5}$$

and the atom center of mass motion can be modeled by classical mechanics. Since the force is proportional to the quantum numbers, it follows that in a given electric field, atoms with different quantum numbers are subject to different accelerations, such that a beam with a broad distribution of the axial velocity is obtained. The possibility to de-excite the Rydberg antihydrogen and to re-excite it to a well defined level is under consideration, and tests of this technique are being carried out. Having a single quantum state is a clear advantage for the acceleration, transport and focusing of the antihydrogen beam. Nevertheless the

simulations of the gravity measurement have shown that a broad axial velocity distribution is sufficient to meet the physics goals of AEGIS. The important point is that the acceleration must be performed in such a way that the axial velocity of the antihydrogen atoms can be reconstructed from the measurement of the arrival time on the detector at the end of the Moiré deflectometer. With the acceleration scheme described here, the arrival time on the detector is measured from the time t_0 when the electric field is switched off and the true particle velocity v_h is of course

$$v_h = \frac{(2L - L_s - z_s)}{t_{det}} \tag{11.6}$$

where L and L_s are defined in chapter 3. z_s has to be kept as small as possible when compared to $2L+L_s$. and in addition, at least the mean value of z_s can be inferred with the help of simulations.

A tracking code which solves the classical motion equation of a Rydberg atom in the electric field (classical trajectory with a force $\vec{F}_E$) using a 4 step Runge-Kutta solver and interpolating at each time step the electric field map has been written. The time step size is adapted to maximize the speed of the calculation as well as the accuracy: all the data shown here refer to trajectories in which the energy is conserved with an accuracy better than 0.001. In the simulation we assume that the antihydrogen atoms are produced with a uniform spatial distribution in a cylinder with radius 1.5 mm and length 8 mm. The initial velocity in the three spatial directions is randomly sampled from a Maxwell distribution with T=100 mK. Figure 11.2 shows the typical distribution of the initial parameters of the antihydrogen atoms used in the simulation.

The motion of each antihydrogen atom with given quantum number n and k is followed until it radially hits the trap electrode, or until the electric field is switched off. Using the electric field of figure 11.1 and the described timing procedure, the motion of Rydberg antihydrogen having quantum number n distributed as a Gaussian distribution centered on n=30 and with a rms=4 and a flat distribution of the quantum number k (as suggested by the CTMC results about the charge exchange dynamics) has been simulated.

The figures 3.3 and 3.4 of chapter 3 show the resulting axial and z_s distributions. In addition we show here in figure 11.3 the radial velocity distribution at the time t_0 compared with the initial thermal distribution: the radial electric field has provided a small (welcome) cooling effect. Note that the reported simulations of the gravity measurement used the thermal radial distribution.

The radial size of the beam is shown in figure 11.4: less than 1% of the particles are radially lost during the acceleration procedure.

The simulation results discussed until now have been obtained using the relation linking the energy levels to the electric field, but ignoring the magnetic field. We have already discussed the issues related to the presence of the magnetic field in chapter 5. Assuming we are in a parameter region where the avoided crossings are negligible and that the force on the atoms can still be calculated by taking the space derivative of the energy, the presence of the magnetic field changes the energy levels and the sensitivity of the atom to the electric field gradients. We have performed an evaluation of this effect using the expression of the energy levels in crossed electric and magnetic fields to first order as reported in [89]

$$E = k'\sqrt{\gamma^2 + 9n^2 f^2} \tag{11.7}$$

k' is a quantum number different from k but ranging (for a given n) over the same interval and which becomes equal to k when B reaches zero. Figure 11.5 shows the ratio between the electric field component perpendicular to the magnetic field and the electric field modulo versus the radial position in the trap for a fixed z value corresponding to the center of the antiproton cloud. The electric field components depend on x,y,z and so the various points plotted in figure 11.5 for the same r value correspond to different x and y coordinates. This ratio is close to 1 for the radial coordinates of interest indicating that the approximation of crossed electric and magnetic fields is reasonable. By taking the derivative of 11.7 we obtain an expression similar to 11.5 but with a factor

$$\frac{9n^2 f}{\sqrt{\gamma^2 + 9n^2 f^2}} \tag{11.8}$$

instead of n. This factor is the ratio between the force with and without magnetic field in the same electric field configuration (figure 11.6).

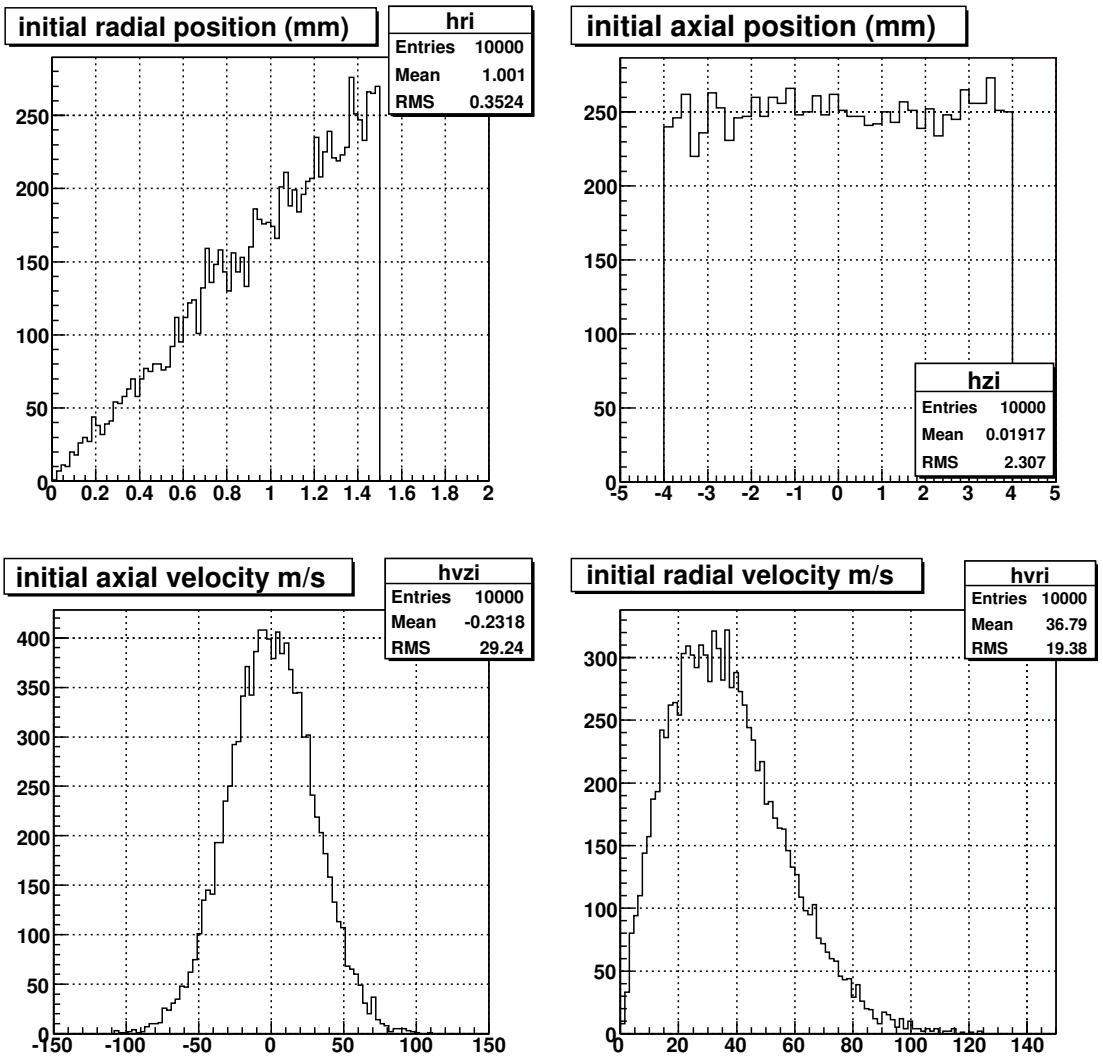

Figure 11.2: Distribution of the initial parameters of the antihydrogen atoms

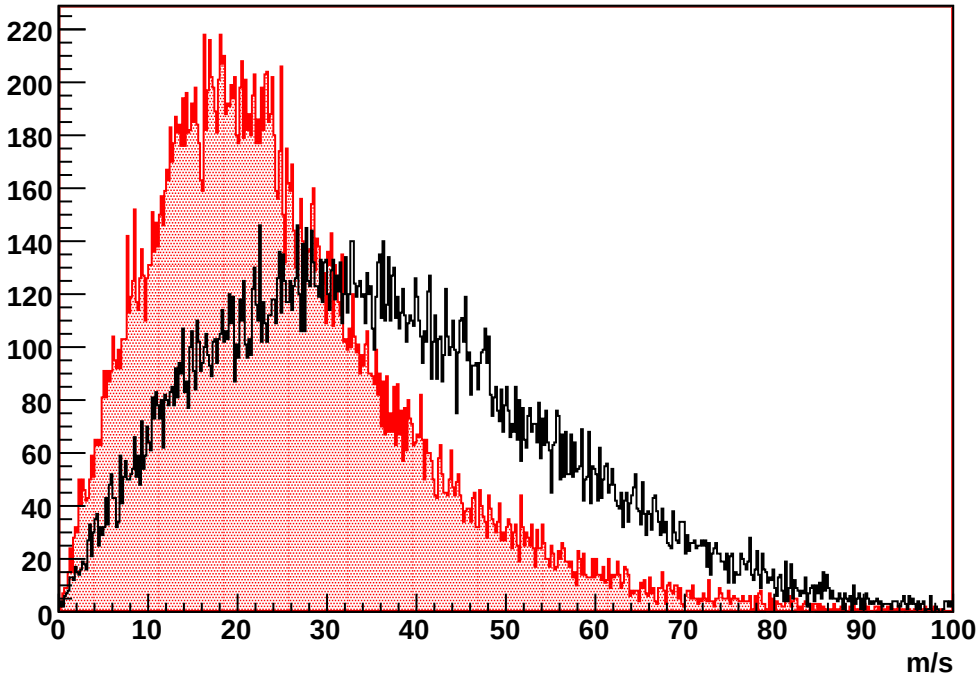

Figure 11.3: Distribution of the radial antihydrogen velocity before the acceleration (black plot) and after (red filled plot)

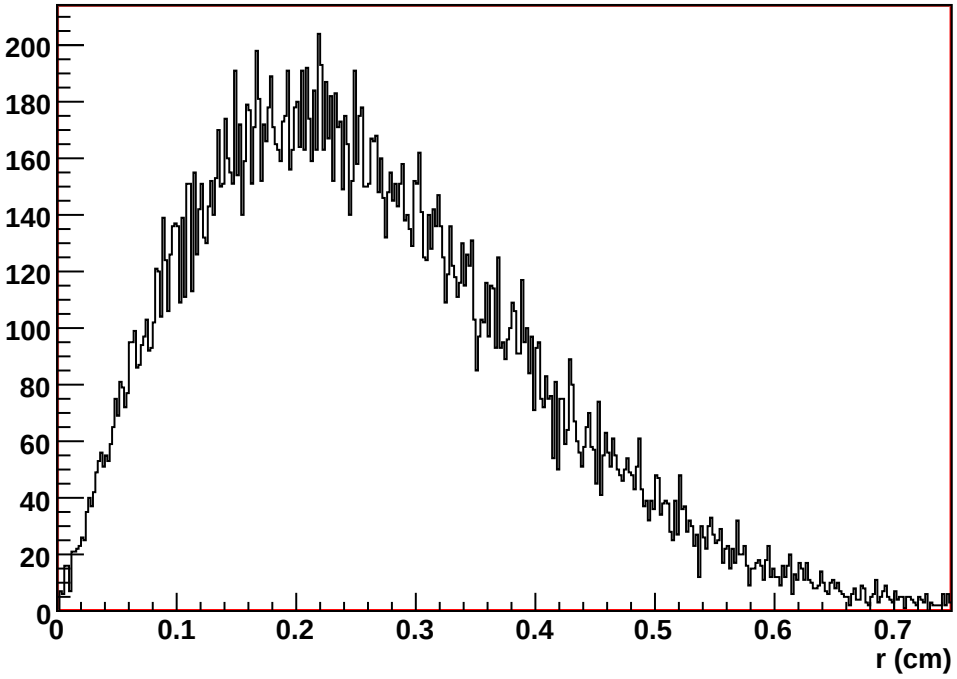

Figure 11.4: Distribution of the radial position of the antihydrogen atoms after acceleration.

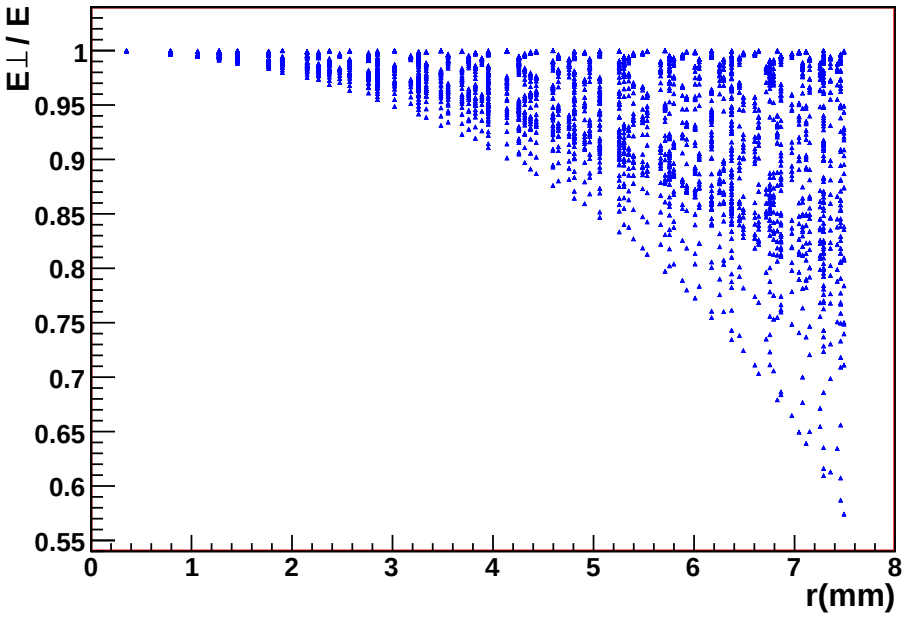

Figure 11.5: Ratio between the Rydberg accelerator electric field component perpendicular to B and the total electric field. The axial coordinate corresponds to the center of the antiproton cloud. The different points represent the ratio for different x,y coordinates.

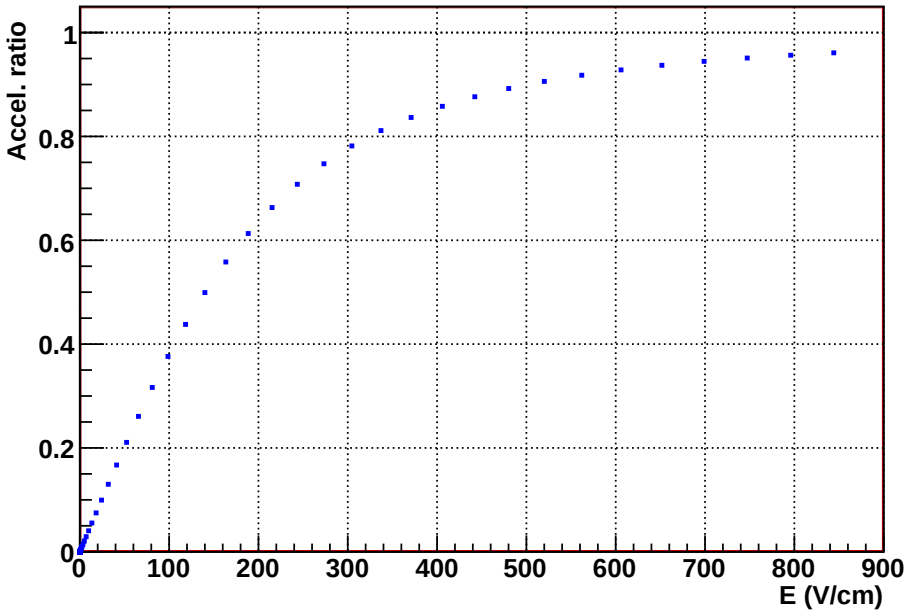

Figure 11.6: Ratio between the acceleration of Rydberg antihydrogen with n=30 with and without magnetic field

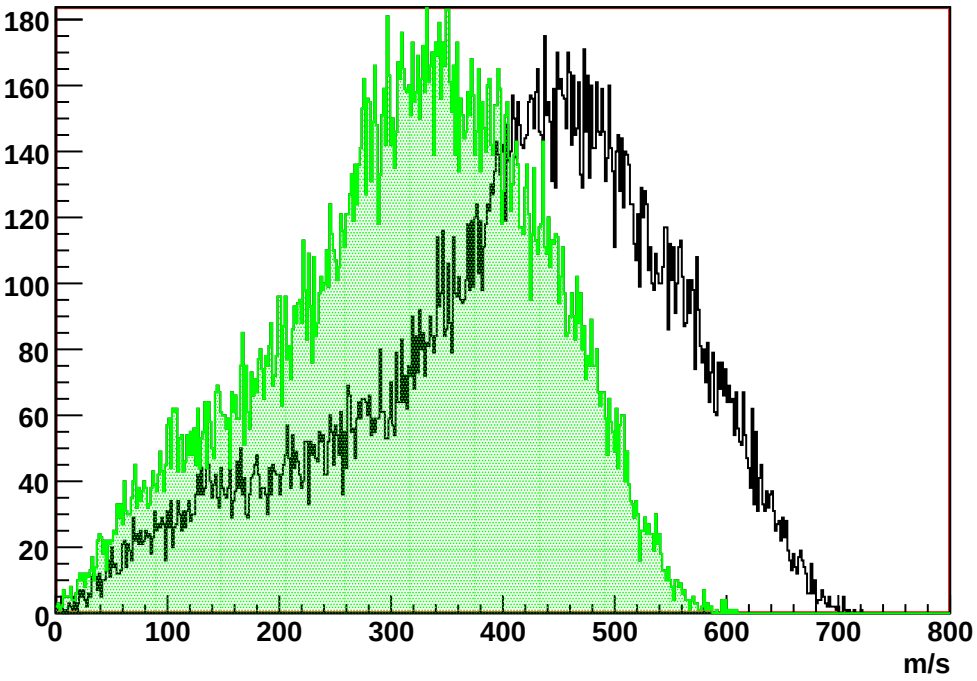

Figure 11.7: Distribution of the horizontal velocity of the antihydrogen accelerated with and without magnetic field with the same electric field. The filled green plot refers to B=1 T, the black plot is for B=0.

The force reduction is tolerable and it mainly results in a reduction of the mean value of the horizontal velocity distribution and in small changes in its shape if the initial conditions of the antihydrogen sample are the same as already used for $B = 0$.

Figure 11.7 shows the horizontal velocity of the accelerated antihydrogen with and without including the magnetic field.

Chapter 12

Decay of Rydberg atoms

After the acceleration process (which requires antihydrogen atoms in Rydberg states) the atoms should decay towards the ground state in the time they need to reach the first grating of the Moiré deflectometer. There are two reasons for this:

- as discussed in chapter 3 the gravity measurement with Rydberg atoms is much more difficult than with atoms in their ground state. This is due to the much greater sensitivity of Rydberg state atoms to magnetic field gradients, as well as to velocity changes in the case of change of principal quantum number inside the deflectometer.
- The force that the Rydberg atoms feel when exiting from the magnetic field (whose value goes from the 1 T in the antihydrogen recombination region to $\simeq 0$ outside the magnet bore) changes the axial energy (minor changes are expected in the radial energy because of the shape of the magnetic field gradient) by an amount $(m+1)\mu_B \Delta B \simeq 0.67\ (m+1)\ {}^0K$ (μ_B is the Bohr magneton). The corresponding change of the axial velocity will make it quite difficult to reconstruct its value from the time of flight measurement.

The design of the main magnet takes particular care of the shape of the fringe field: we will have a short axial region, close to the end of magnet bore, in which the magnetic field sharply goes to zero. A proper magnetic shielding design around the Moiré deflectometer will further reduce any magnetic field gradients there. We assume that the distance L_s between the center of the antihydrogen formation trap and the first grating is several ten cm. In our simulation of the gravity measurement we have assumed $L_s = 30$ cm.

12.1 Lifetime of Rydberg states

The decay rate of a Rydberg atom [181] [182] in an nlm state is independent of the m value due to the isotopic property of spontaneous emission. The decay rate is

$$A_{nl} \approx n^{-3}(l+1/2)^{-2} \times 10^{10}\mathrm{s}^{-1} \tag{12.1}$$

The decay is modified when a magnetic field is present by a factor [183] [184] [186] $(1 \pm n\mu_B B/E_n)$ where $E_n = \frac{13.6\,\mathrm{eV}}{n^2}$ is the binding energy of the Rydberg state. This factor is negligible in our case of 1 T field and $n < 40$.

More precisely [185] [186]

$$-\frac{dn}{dt} \approx 1.61 \times 10^{10}\,\mathrm{Hz}\frac{3n^2 - l^2}{3n^2 l^5} \tag{12.2}$$

$$-\frac{dl}{dt} \approx 1.61 \times 10^{10}\,\mathrm{Hz}\frac{2}{3n^3 l^2} \tag{12.3}$$

The solution is

$$n(l)^{-2} = \frac{1}{l^2}\left[1 - \left(\frac{l}{l_0}\right)^3\right] + \frac{1}{n_0^2}\frac{l}{l_0} \tag{12.4}$$

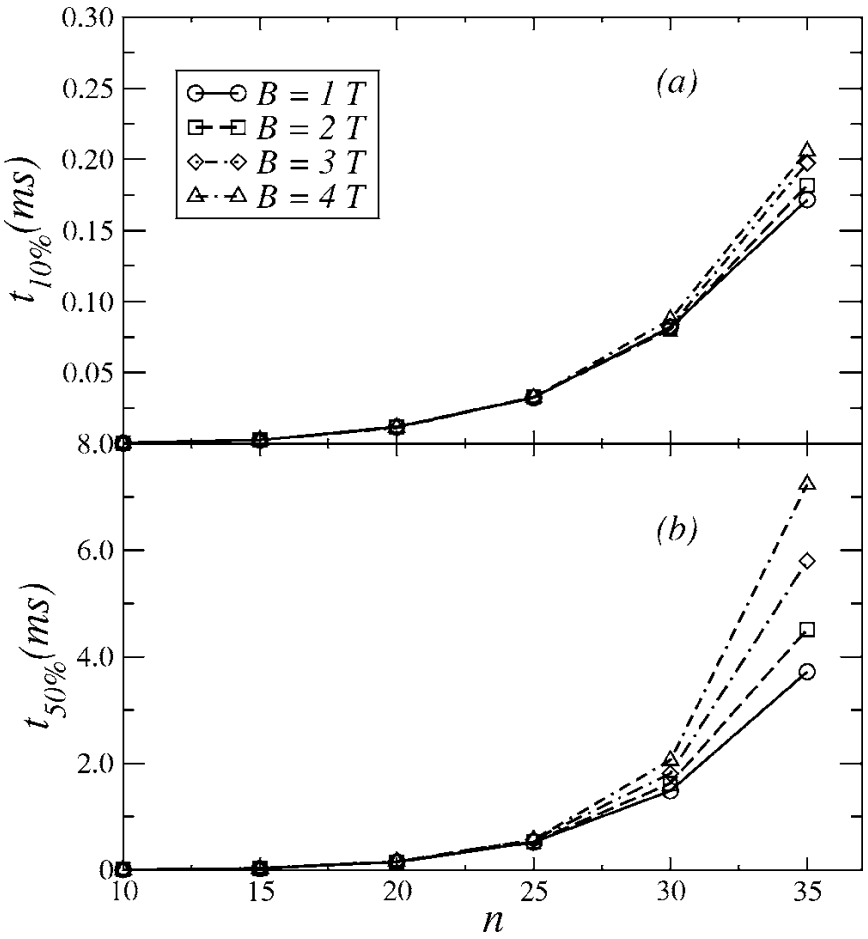

Figure 12.1: Time necessary to have 10 % and 50 % of antihydrogen atoms radiatively decayed to the ground state, starting from a distribution with n fixed and completely mixed l [186].

A typical lifetime for Rydberg states with $n \sim 30$ $l \sim 10$ is $\tau = A_{nl}^{-1} \sim 300$ μs.

Note that the n decay rate rapidly increases as l decreases and, assuming equipartition of the Rydberg states, the high l states are the most populated ones (their number is proportional to $2l + 1$ due to the m degeneracy). Figure 12.1 from [186] shows the time necessary to reach the ground state when starting from a population with given n and all l equally distributed. The values reported in this plot can be used as reference values but the time necessary to have a large fraction of the antihydrogen in the ground state in AEGIS depends on the specific state population. Note that figure 4.6 does not show a uniform l distribution. Calculations of the produced antihydrogen state distribution in a magnetic field, and the expected total decay time in AEGIS, are in progress.

If $v_h \simeq 300$ m/s than the time to travel $\simeq 20$ cm is about 650 μs and so we expect that a reasonable fraction the antihydrogen atoms will decay before reaching the region with high magnetic field gradient if they are produced in quantum states with n not very high.

12.2 Acceleration of the radiative decay

It is of great interest to select experimental procedures allowing to accelerate the radiative cascade. The previous discussion shows that this may be necessary in the present design of AEGIS but, in addition, if such technology is available other additional powerful experimental procedures can be implemented in AEGIS. For instance one could consider de-exciting, and then re-exciting the produced antihydrogen atom to a well defined state before acceleration, opening up the possibility of producing a beam with a narrow horizontal velocity distribution. Having a single quantum state allows atom focusing and transportation in a simpler way than in case of a broad state distribution.
Several methods have already been proposed or used to control, increase or decrease the lifetime of Rydberg states, mainly relying on time-dependent electric fields (see references in [187]). However they are all restricted, more or less, to well-defined nkm Rydberg states and not for a mixture of Rydberg states as created by the positronium collisional process.
Roughly speaking, in order to reduce the lifetime of a given state, we just have to reduce the l quantum number. It is well known that collisions with electrons create varying electric fields, leading to l and m mixing [188]. This is very difficult to quantify but the presence of charged particles can help accelerate the decay process. A cloud of high density cold electrons can be loaded in a trap made by the electrodes following the Stark acceleration region.
It is well known that the a blackbody radiation accelerates the decay of Rydberg states. A detailed study of the blackbody effect on Rydberg states has been done [189]. The rate of radiative decay Γ_{if} from state i to state f is the sum of natural and of Blackbody radiation induced decays: $\Gamma_{if} = \Gamma_{if}^{\rm nr} + \Gamma_{if}^{\rm BB}$. Omitting details, $\Gamma_{if}^{\rm BB}$ is given by

$$\Gamma_i^{\rm BB} = \sum_f \Gamma_{if}^{\rm BB} \approx 2 \times 10^7 \frac{T({\rm K})}{300\,{\rm K}} n^{-2}({\rm s}^{-1}) \tag{12.5}$$

The most interesting part of this formula is the fact that the effect (absorption and decay) is independent of the l value. Therefore, blackbody radiation can accelerate the cascade of high angular momentum states. The main interest of blackbody radiation compared to laser light is the broadband spectrum which could then couple to every possible transition. Accurate calculations are in progress by members of AEGIS [190] and the preliminary results clearly indicate that the high l states most strongly couple to the blackbody radiation, and that the $n, l \rightarrow n-1, l-1$ decay is the most favored one, except for low l states where the spontaneous decay already exists.
However at 0.1 K the blackbody radiation effect is negligible and so external radiation has to be inserted in the system. Using external laser or millimeter fields we should be able to stimulate the decay of nearly half of the Rydberg states toward the ground state within typically 100 μ sec. For this purpouse experiments are in progress in Orsay [190].

Chapter 13

CW and quasi-CW Lyman-α laser sources for cooling antihydrogen

Several experimental efforts are in progress within the AEGIS collaboration aiming to develop Lyman-α laser sources. These sources are a powerful tool which allow cooling of antihydrogen. In addition such a laser light is needed to perform atom interferometric gravity measurements as discussed in chapter 3 and to perform antihydrogen 1S-2S spectroscopy via the shelving method as described in [200]

Building a powerful Lyman-α source is a very challenging task. The activity in progress within AEGIS is aiming to develop CW laser sources and quasi-CW laser pulses, that is pulses with time duration of the order of 100 μs. The technology for building such quasi CW-laser pulses is already demonstrated and the first use of such a laser will be to radially cool the antihydrogen beam in the AEGIS setup described in this document.

13.1 Laser cooling

In a very simplified picture, the so-called 1D Doppler cooling is based on the recoil of the atoms induced by photon absorption. A laser with a frequency tuned slightly below an atomic transition is shone on the atomic sample. The standing wave can be thought as the sum of two counterpropagating beams. Atoms with a velocity component along the standing wave, due to Doppler effect, will preferentially absorb from only one beam.

The velocity variation is $\Delta v = \hbar k/M$ where k is the photon wavenumber and M is the atom mass. The decay of the atoms towards the initial state produces a recoil with random direction whose average effect is null.

The cooling is realized by several photon absorptions.

The final velocity is related to the Doppler temperature T_D related to the linewidth of the transition Γ by $K_B T_{Dop} = \hbar\Gamma/2$ (K_B is the Boltzmann constant). At T_D the probability to absorb from both beams is similar so the average momentum does not decrease anymore. In addition the relation $\hbar^2 k^2/(2M) < \hbar\Gamma$ has to be satisfied.

Several schemes to laser cool (anti-)hydrogen atoms have been proposed (for a recent suggestion, see [193]) using the $1s \rightarrow 2s$ [194] [195] as well as the $1s \rightarrow 3s$ transition [196] have been proposed, but they are limited by ionization processes and by the amount of power needed to realize the 2 photon transition. Consequently, the cooling on the $1s \rightarrow 2p$ transition is probably the simplest approach. Ultraviolet photons with 122.5 nm are necessary (see figure 13.1).

The probability to excite the 2-level atom, on the $1s \rightarrow 2p$ transition, is

$$P_{\mathrm{exc}} = \frac{1}{2}\frac{I/I_{\mathrm{sat}}}{1 + I/I_{\mathrm{sat}} + 4\delta^2/\Gamma^2} \tag{13.1}$$

where I is the laser intensity. $I_{\mathrm{sat}} = 7W/\mathrm{cm}^2$ is called the saturation intensity, δ is the laser detuning $\Gamma = 2\pi \times (100\mathrm{MHz})$=1/lifetime = 1/1.6 ns = $6.25 \cdot 10^8 \mathrm{s}^{-1}$ is the natural line-width of the transition.

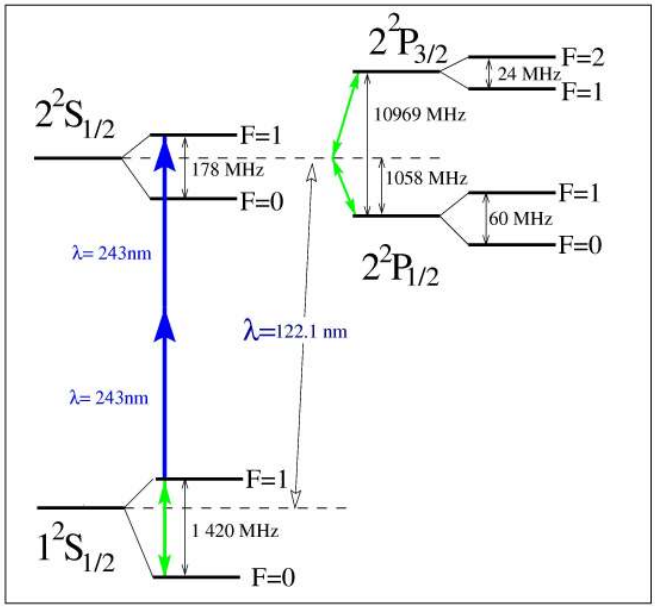

Figure 13.1: Hydrogen level scheme

This formula is valid for a laser with line-width γ_L smaller than γ. All the numerical values refer to the $1s \rightarrow 2p$ transition.

The most efficient laser cooling is then achieved when the laser just saturates the transition $I \sim I_{\rm sat}$. There is no need to have $I > I_{\rm sat}$ because stimulated emission will replace spontaneous emission, and the laser cooling would be less efficient. Assuming a typical spot size (2 times waist w) of 2 mm, the laser power P needed is (using $\frac{2P}{\pi w^2} = I$) 100 mW.

To laser cool (anti)-H from 1K down to few mK (the Doppler limit) the atoms have to absorb about 50 photons (150 m/s initial velocity / 3 m/s the recoil velocity). A better experimental value is probably 10 times this one for complete 3D laser cooling. A typical laser detuning is $\delta = 2.5 \times \Gamma$ so $P_{\rm exc} \simeq 1/50$. Therefore we need to shine the $I = I_{\rm sat}$ laser during $50 \times 10 \times$lifetime$/P_{\rm exc} \sim 40\mu$s in order to laser cool the atoms.

13.2 CW Lyman-α light generation

The standard technique to obtain the 121 nm wavelength (Lyman-α light) is through four-wave mixing. In a four–wave mixing process three photons are coherently added in a nonlinear medium so the output power P_o is given by

$$P_o = k' P_1 P_2 P_3 \tag{13.2}$$

where P_i is the power of the i–th input beam while in k' appears a sum of denominators containing terms of the form $E_a - E_b - \hbar\omega_i$ where E_a, E_b are energy levels of the nonlinear medium.

Presently only one Continuous–Wave (CW) source has been built, with a power of 20 nW [191] [192]. The source relies on four–wave mixing in Hg vapour to build a single Lyman-α photon at $\lambda = 121.5$nm from 3 photons at $\lambda = 257$, 399 and 545 nm.

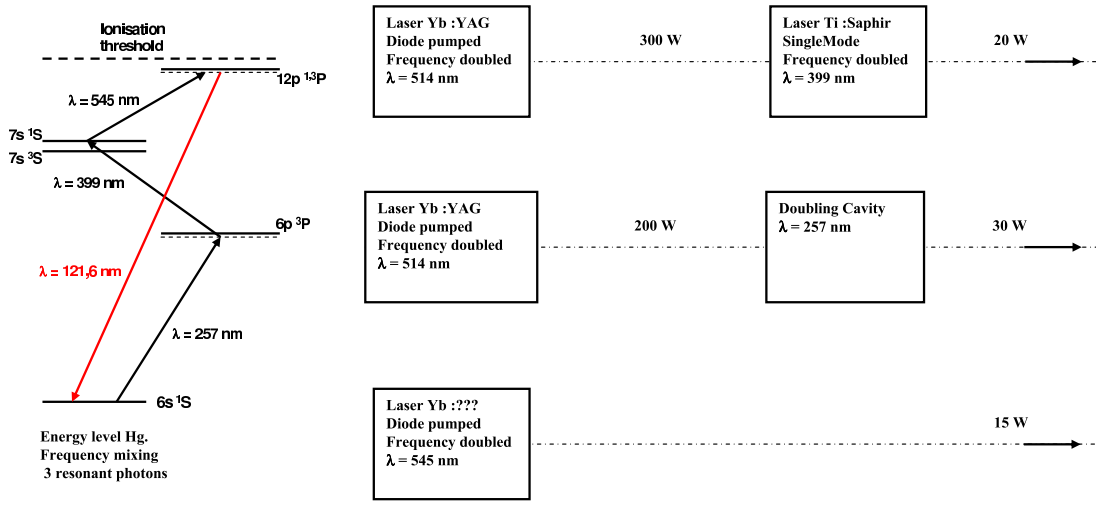

Figure 13.2: Proposed scheme to realize the Lyman-α light.

We are currently investigating the possibility to use three tunable solid state lasers as sources for four–wave mixing in order both to reduce size and cost and, at the same time, to increase P_o by increasing each of the P_i. The use of three tunable sources (in [191] [192] the 545 nm source is at fixed frequency) should allow also to optimize k'. The total gain in P_o could bring P_o into the 100 μW range according to this very simple model but various loss and saturation effects still have to be assessed.

13.3 Quasi-CW Lyman-α laser source

The use of a commercial pulsed laser (10 ns pulse duration) enhances the four-wave mixing process and the efficiency is such that the Lyman-α light allows to saturate the laser transition. However a 10 ns pulse duration is too short to realize an efficient cooling. In order to combine the advantages of the CW and of the pulsed source we propose here to use a quasi-continuous laser source [199] of $200 - 400\,\mu$s duration at $10 - 20$ Hz repetition rate. This Lyman-α source, with 100 mW peak power during $100\,\mu$s with a line-width below 100 MHz, should be able to laser cool anti-hydrogen ground state atoms.

We propose the scheme shown in figure 13.2 to realize the 100 mW Lyman-α light. This scheme is based on (three) quasi-continuous lasers. L. Cabaret in the Aimé Cotton laboratory has already realized such a tunable frequency doubled Yb:YAG laser ($510 - 520$ nm), as described in Fig. 13.3, and our proposal is based on his expertise.

The final Lyman-α intensity value (100 mW) has been calculated by linear extrapolation from the four-wave mixing experiment of [191]. This 100 mW is just an order of magnitude because saturation effects in the mercury vapor have not been taken into account. Possible improvements, such as the cavity

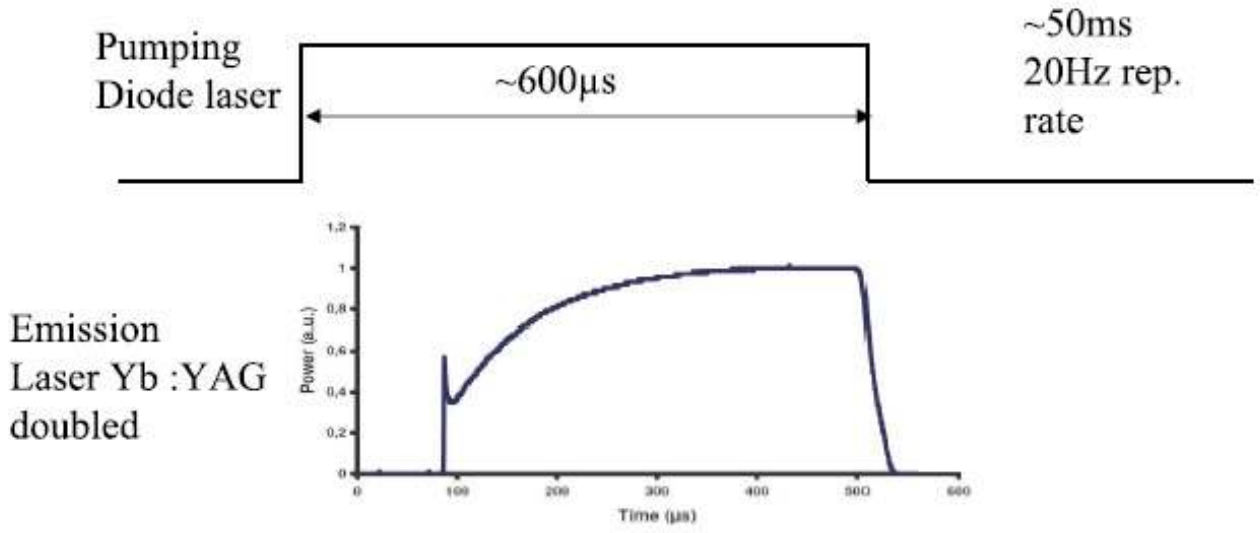

Figure 13.3: Creation of the 60 W (peak output power) quasi-continuous laser of [198].

under investigation, have yet to be studied (see also [197]).

Chapter 14

Future developments: antihydrogen trapping and cooling

The production of ultra-cold antihydrogen for a gravity measurement based on atom interferometry is the main long term scientific goal of AEGIS and the necessary experimental requirements have been discussed in chapter 3. Spectroscopic measurements are also of great interest for AEGIS. The availability of cold antihydrogen opens up the possibility of performing both types of measurements.

The design of AEGIS permits an upgrade of the experimental apparatus to perform higher precision gravity and/or accurate spectroscopic measurements in a second phase. Depending on the experimental scheme, trapped ultra-cold (mK or sub mK) antihydrogen or a well collimated cold antihydrogen beam is needed.

Since the direct production of ultra-cold antihydrogen is quite unlikely, the essential experimental goal that must be reached is cooling of antihydrogen atoms. The second phase of the AEGIS experimental program foresees trapping the antihydrogen atoms in a magnetic trap and cooling them inside the trap with a quasi-CW Lyman-α laser or with a CW Lyman-α source. Work to develop such laser sources is already in progress by members of AEGIS. The limiting temperature of the laser cooling is expected to be close to 1 mK: this value is still too high to allow a gravitational atom interferometric measurement but it is low enough to perform competitive CPT tests through a measurement of the 1S-2S transition with trapped antihydrogen.

In the absence of stray electric fields that would mix the $2S$ and the $2P$ levels, the observed linewidth $\Delta\nu$ will be limited by the residual Zeeman effect on the $1S-2S$ transition of 186 kHz/T. Due to the residual thermal motion, the magnetic field variation ΔB seen by the atoms will be of the order of $\Delta B = kT/\mu_b \sim 2$ mT so $\Delta\nu \sim 250$ Hz. A laser source at 243 nm with suitable frequency stability is a state–of–the–art device that can be built by combining a solid state source [201] and an ultrahigh stability optical cavity [202]. The excitation rate Γ_e per particle on the weak $1S-2S$ 2 photon transition will be fairly low, of the order of 1 s^{-1}, so detection via shelving spectroscopy using Lyman-α light is probably necessary. In this way, cycling among excitation, detection and cooling phases, it may be possible to detect the absorption of a number of photons over time as $N_\gamma(t) = \eta N_{\bar{H}} \Gamma_e t$ where η is an efficiency that takes into account the duty cycle of the three phases and that we estimate as $\eta \sim 0.1$. The resolution of the measurement scales as $\Delta\nu/\sqrt{N_\gamma(t)}$ as long as $1/f$ noise sources can be neglected. A final resolution in the 1-10 Hz range should be possible in our case.

Experimental results on the production of a collimated antihydrogen beam will be obtained with the basic design of AEGIS without trapping antihydrogen: our quasi-CW Lyman-α laser source should allow in fact to cool the antihydrogen beam produced with the apparatus described in this document. The possibility of performing 1S-2S spectroscopy in flight is also being evaluated.

14.1 Antihydrogen trapping

Trapping of atoms with a magneto-static trap providing a magnetic field minimum of the modulos in free space is routinely used in numerous atomic physics experiments. Atoms with a magnetic moment

can be trapped in low-field seeking states (such as $1s, F = 1, m_F = 1$ state for antihydrogen atoms) for which the energy increases with the magnetic field strength. The adiabatic trap potential is given by $U(r) = \mu \|\vec{B}(\vec{r})\|$ where μ is the magnetic moment of the state. For antihydrogen in the fundamental state $\mu = 0.67K/T$ and thus, as a reference, a trap with a gradient 1T/cm can confine antihydrogen atoms having an energy up to 0.67 K within 1 cm. The simplest trap is the spherical quadrupole trap realized

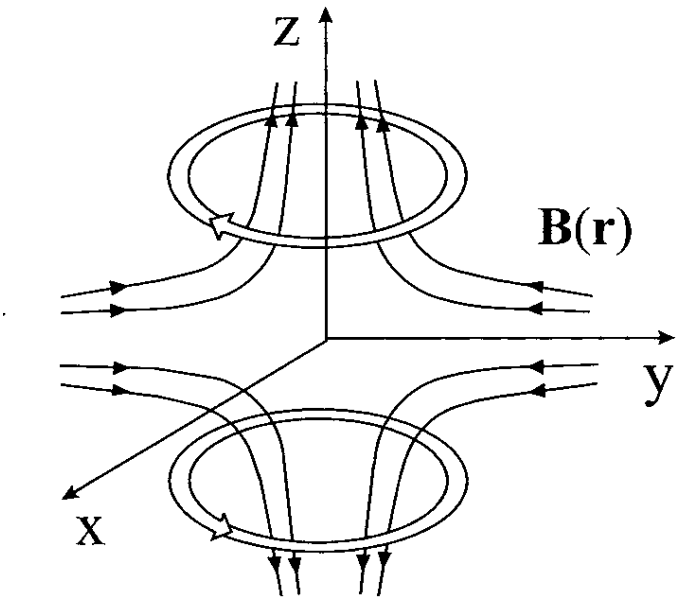

Figure 14.1: Spherical quadrupole magnetic trap

by 2 coils with opposite currents, as shown in fig 14.1, and a distance choosen to maximize the magnetic field gradient B': $B = B'\sqrt{x^2 + y^2 - 4z^2}$. The main advantage of this two coil configuration is that the trapping potential is very deep in comparison to more complex geometries. However an important feature of the magnetic trap is the presence (or absence) of points with null magnetic field. If the direction of the field vector $\vec{B}$ changes rapidly compared to the Larmor precession frequency (and this happens if B=0) the spin will not be able to adiabatically follow the field. This gives rise to non-adiabatic spin flips (also called Majorana flips) leading to losses of particles. Spin flips occur when an atom crosses the Majorana sphere of radius $r_{\mathrm{Maj}} \sim \sqrt{\frac{\hbar v_d}{\mu B'}}$ (typically of the order of one micron for mK antihydrogen) where v_d is the velocity inside the trap. This loss process can be problematic for a quadrupolar trap when the cloud temperature is small because it reduces the lifetime of the cloud to $\tau_{\mathrm{flip}} \sim mL^2/\hbar$ where $L \sim \frac{k_B T}{\mu B'}$ is the size of the cold sample and m is the atom mass [203]. For a 100 mK antihydrogen cloud in a magnetic gradient of $B' \approx 0.220\,\mathrm{T/cm}$ this time is expected to be very long (10 minutes). Only when the atoms are very cold the storage time is strongly reduced by Majorana transitions. A trap configuration that avoids regions with null magnetic field is the so called Ioffe-Pritchard trap shown in figure 14.2 In order to increase the antihydrogen storage time, we are considering the possibility to switch from a simple quadrupolar trap to a Ioffe trap once the trapped sample temperature is close to or below the mK value.

In the second phase of AEGIS, we envisage an experimental set-up for trapping antihydrogen that is very different from the one proposed by the other AD experiments. In these experiments it is planned to superimpose a Penning-Malmberg trap with a quadrupolar Ioffe-Pritchard (or higher order multipole) trap and to produce antihydrogen directly inside the superimposed traps. In AEGIS we will form a beam of antihydrogen and we will transport this beam from the production region to a spatially separated magnetic trap. The needed flight distance from the production region to the trapping region is under

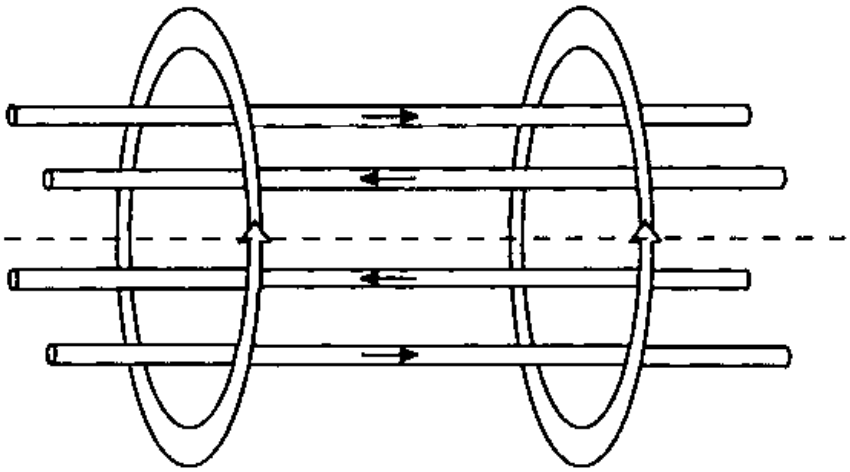

Figure 14.2: Ioffe-Pritchard magnetic trap

study but it is expected to be of the order of some tens cm.

The spatial separation of the production and trapping regions well matches with the AEGIS design and it allows to optimize the design of the magnetic trap without the constraints imposed by the need to simultaneously confine the charged and neutral particles. The combined Malmberg-Penning-Ioffe trap requires a rather strong ($\simeq$ 1T) axial bias magnetic field and this limits the resulting antihydrogen well energy depth as can be easily seen by assuming an infinite length system and neglecting the effect of the axial coils. The potential energy is

$$U = \mu \left(\sqrt{B_z^2 + B_0^2 \left(\frac{r_t}{r_0} \right)^{2n-2}} - B_z \right) \tag{14.1}$$

Here $2n$ is the multi-pole order, B_0 is the intensity of the multi-pole field at the radius r_0, r_t is the radius of the electrodes of the charged particle trap and B_z is the axial magnetic field of the charged particle trap.

The possibility of achieving confinement of the charged particles in such a combined trap over long times has been a subject of debate since several years. Some experiments on injection and storage of charged particles in Penning traps combined with a quadrupole excluded the possibility of using such a configuration in antihydrogen experiments [204] while more recent results [205] claim that quadrupolar traps can be used. The first experiment showing long term confinement of a non-neutral plasma in a combined Malmberg- Penning trap combined with a sextupole radial magnetic field has been performed by members of AEGIS during the R&D phase leading to the AEGIS design [128]. Plasma confinement times consistent with antihydrogen production schemes have been obtained but at the same time have shown the presence of a worrying plasma expansion and a resulting Joule heating. The temperature of the charged particles could be too high to allow the production of a reasonable number of antiatoms cold enough to be trapped.

The magnetic trap for antihydrogen will be installed outside the main AEGIS magnet after having removed the grating system. Radial cooling of the antihydrogen beam by the quasi-CW Lyman-α laser will be used to reduce the radial size of the beam and to limit the magnetic trap dimensions to a few cm. Of course it is not sufficient to transport antihydrogen towards the potential well of the trap because

during the travel into the trap region a simple exchange of potential and kinetic energy will happen and the antihydrogen will not remain trapped. In order to accumulate successive shots of antihydrogen in the the trap, a dissipation mechanism must act during the travel time inside the trap and this must reduce the antihydrogen energy below the top of the trap well. We are evaluating the possibility of transporting ground state antihydrogen or to re-excite the radially cooled antihydrogen beam to a well defined Rydberg state. For antihydrogen in the fundamental state the quasi-CW Lyman-α light can be used to cool the beam while, if the antihydrogen is in a Rydberg state, Stark forces will be used to reduce the antihydrogen velocity in a way very similar to the one used to accelerate the antihydrogen immediately after its production.

The efficiency of this cooling mechanism acting at the trapping time determines the mean value of the initial antihydrogen energy. Superconducting magnets have to be used if the initial energy is close to 1 Kelvin while non-superconducting coils could be sufficient to trap antihydrogen with $\simeq$ 100 mK energy. Hollow copper tubes cooled by high pressure water flowing through can sustain a maximum useful current density of about 50 A/mm^2 and the power dissipated in the coils scales as the radius to the third power. Compact coils are mandatory. The spherical quadrupolar trap can be therefore realized by 2 coils of 2 cm radius separated by 2 cm. 50 turns of 2 mm outer diameter hollow copper wire with 200 Amps (current density 50 A/mm^2) in each leads to a magnetic gradient of $B' \approx 0.220\,\mathrm{T/cm}$. The magnetic field calculations show that a a trapping potential of $\simeq$ 150mK can be obtained.

Approval and beam time for this second phase of the experiment will be requested in due time and detailed documentation will be provided at that moment. Here we wish to underline that the R&D activities for these ambitious goals are already being carried out. Procedures allowing to further reduce the energy of the trapped antihydrogen well below the mK value are also under study.

Chapter 15

AD requirements

The proposed experiment requires the use of the full DEM zone of the AD (with the exception of the upstream area in which AD-4 is positioned), implementation of a 100 MeV/c beam transport line in the DEM zone up to the trapping magnet, and space for both a laser hut and a control room in the AD building (193) or immediately outside of it. The initial bending dipole of the beam line should also allow an unperturbed beam to continue to be delivered to the AD-4 experiment, with which AEGIS would share the DEM zone.

We intend to carry out as much of the commissioning and testing as possible with protons, electrons and positrons, but will require regular access to an antiproton beam from 2010 onwards, at the level of the currently installed major experiments and with the option of some beam time in 2009.

In discussions with responsibles in the CERN/AB department, we have identified some of the necessary beam transport elements (dipole, quadrupoles), although beam transport calculations will still need to be carried out. As such, the precise layout of the experiment in the DEM zone can not be finalized as long as the position of the final focus is not known. Power supplies and auxiliary equipment for the beam transport elements will need to be identified or procured. We have also identified two areas suitable for the laser and control huts, which would not interfere with any possible future dismantling of the concrete protection structure of the accelerator. Discussions are under way to identify a pathway for the laser pulses and experimental control cables which would meet the same criterion.

The feasibility of the measurement of this proposal is based on the currently achieved performances of the AD machine. Neverthless we support the ELENA project and any effort to increase the number of available antiprotons. Both the second phase of AEGIS, as well as the first phase being proposed here, would definitely benefit from the possibility of using large numbers of antiprotons. This would also ease any potential scheduling problems between the currently installed three major users of antiprotons and AEGIS, should this proposal be approved.

Chapter 16

Appendix 1: Precision measurements and search for new physics with an intense positron beam

We wish to underline here that the experimental activity and the developments on the formation of positronium needed for AEGIS could furnish, as a by-product, important results on the positronium decay time and the branching ratio into different channels or at least important developments for such types of experiments. We briefly review here the physics case. Positronium (Ps), the positron-electron bound state, is the lightest known atom, which is bound by, and self-annihilates through, the same, electromagnetic interaction. At the current level of experimental and theoretical precision this is the only interaction present in this system. This feature has made positronium an ideal system for testing the accuracy of QED calculations for bound states, in particular for the triplet (1^3S_1) state of Ps, orthopositronium ($o-Ps$). Due to the odd-parity under C-transformation, $o-Ps$ decays predominantly into three photons. As compared with the singlet (1^1S_0) state (parapositronium), the "slowness" of $o-Ps$ decays, due to the phase-space and additional α suppression factors, gives an enhancement factor $\simeq 10^3$, making it more sensitive to an admixture of new interactions which are not accommodated in the Standard Model.

Many interesting experiments performed or planned with $o-Ps$ are motivated by tests of higher order QED corrections to the $o-Ps$ decay rate [207], by studies of the negative ion of positronium [208], by searches for a violation of fundamental symmetries in positronium annihilation [209], , by the possibility of observing positronium Bose-Einstein condensation [210] and other areas of research.

In this Addendum we briefly review some aspects concerning both the theoretical and the experimental study of positronium, focusing on precision measurements and searching for new physics beyond the Standard Model with this simplest atom. More detailed discussions can be found elsewhere, see e.g Ref.'s [211]-[214]. Note that tests of antimatter gravity in the free gravitational fall of positronium have been recently discussed in Ref. [215]

16.1 Orthopositronium decay rate in vacuum

The experimental study of the o-Ps decay rate has a colorful history of more than 15 years of inconsistent results and poor agreement with theoretical predictions (see Ref. [207] for a review).

Recently Adkins et al. [207] have obtained results on precise calculations of the $p-Ps$ and $o-Ps$ total decay rates in vacuum:

$$\Gamma_o^{\rm th} = 7.039979(11)\ \mu{\rm s}^{-1}\,, \tag{16.1}$$

$$\Gamma_p^{\rm th} = 7989.6178(2)\ \mu{\rm s}^{-1}\,, \tag{16.2}$$

where the given errors stem only from the uncertainty in the numerical values of the perturbative coefficients.

These results have triggered new experiments aimed at solving long-standing disagreement between theory and experiment. The most recent independent measurements in SiO_2 powder [216] and vacuum [217] experiments

$$\Gamma_o^{\rm exp} = 7.0396(12)^{\rm stat.}(11)^{\rm syst.}\ \mu{\rm s}^{-1}\ \ ({\rm SiO_2\ powder})\,, \tag{16.3}$$
$$\Gamma_o^{\rm exp} = 7.0404(10)^{\rm stat.}(8)^{\rm syst.}\ \mu{\rm s}^{-1}\ \ ({\rm vacuum})\,, \tag{16.4}$$

are consistent with each other and are in a very good agreement with Eq. (16.1). However, the experimental precision is a factor 100 worse than that achieved by theorists. Further improvement of the experimental accuracy would allow for the first time to test corrections of the order α^6.

16.2 Positronium hyperfine splitting

Positronium hyperfine splitting (HFS), $\Delta\nu = E\left(1^3S_1\right) - E\left(1^1S_0\right)$, where $E\left(1^1S_0\right)$ and $E\left(1^3S_1\right)$ are the energy levels of the $p-Ps$ and $o-Ps$ ground states, is the most precisely measured quantity in positronium spectroscopy as far as the absolute precision is concerned. The most recent measurements of HFS yielded [218, 219]

$$\Delta\nu^{\rm exp} = 203.387\,5(16)\,{\rm GHz}\,, \tag{16.5}$$
$$\Delta\nu^{\rm exp} = 203.389\,10(74)\,{\rm GHz}\,. \tag{16.6}$$

On the theoretical side we have

$$\Delta\nu^{\rm th} = 203.391\,69\,{\rm GHz}\,, \tag{16.7}$$

which exceeds Eqs. (16.5) and (16.6) by approximately 2.6 and 3.5 experimental standard deviations, respectively. The experimental error for HFS is compatible with a naive estimate of the theoretical uncertainty due to as-yet unknown higher order corrections. Should this discrepancy persist after the dominant terms of the latter have been calculated and the experimental accuracy has been increased, this would provide a signal for new physics. This makes the HFS one of the most interesting topics in positronium spectroscopy, both from the experimental and theoretical points of view.

16.3 Decays of positronium beyond the Standard Model

Decays of $o-Ps$ that could manifest themselves through the presence of new physics beyond the Standard Model, can be classified into the four following categories: i) $o-Ps \to \gamma X$ ii) $o-Ps \to \gamma\gamma X$ iii) $o-Ps \to N\gamma$, and iv) invisible decays, where X is a new light particle(s) and $N = 2, 4, ..$ (for a review, see e.g. [212]).

The $o-Ps \to invisible$ decay is probably one of the most interesting. It is motivated by the possible existence of

- extra dimensions [229],
- hidden sectors and dark matter [230]
- PVLAS anomaly and string theory [231]
- new light bosons

In table 16.1, bounds on exotic orthopositronium decay modes are summarized.

Table 16.1: Upper limits on the branching ratios of several exotic o-Ps decays.

Decay Mode	90% upper limit, ppm	Motivation	Group
$\gamma\gamma$	233	Space Isotropy	Michigan[222]
	350	BE statistics Violation	Tokyo [223]
$\gamma\gamma\gamma$	2.6	C–parity Violation	Tokyo [221],
	3.7		Berkeley [232]
		New long-lived X-boson	
	5-1	m_X ∼100-900 keV	CERN [220]
$\gamma + X$	1.1	m_X <800 keV	Tokyo [224]
	340	m_X <30 keV	INR(Moscow) [227]
		New short-lived X-boson	
$\gamma + X \rightarrow \gamma + 2\gamma$	28	m_X <30 keV	INR(Moscow)[226]
	300	m_X <500 keV	Tokyo [225]
$\gamma + X_1 + X_2$	44	m_{X_1}+m_{X_2} <900 keV	ETHZ-INR(Moscow) [228]
	2.8	Extra dimensions	Tokyo [234]
Invisible	540	PVLAS, Millicharged particles,	INR(Moscow) [233]
	0.42	and String Theory	ETHZ-INR(Moscow) [235]
		Mirror Dark Matter	

Chapter 17

Appendix 2 : Intense positron beams: Material research and industrial applications

Although the layout of the AEGIS experiment has been optimized for the targeted physics, subsidiary measurements, among them a set of measurements of potential interest to industry, can be carried out with the same apparatus. Such ancilliary measurements make use of the installed equipment and infrastructure, will be carried out outside of the AD beam delivery periods, and will primarily be used to optimize the physics output.

Technology developed for nuclear and particle physics research has made and continues to make a lasting impact on society in areas such as material sciences, biology, medicine, etc. Today's society pushes science to strengthen applications of its scientific achievements. Technology transfer projects are one of the key elements of CERN's strategy for particle physics [206]. Positron physics with mono-energetic beams of positrons is an excellent example permitting developments responding to such objectives.

Nowadays, there is a fundamental interest in studies of polymer surface interfaces and, in particular, of nanoporous materials which have attracted tremendous interest due to their many potential applications, including but not limited to low-dielectric constant (low-k) thin films in the microelectronic industry, membranes and selective permeation filters in biotechnology, and catalysts in chemical engineering [99].

For example, porous silica films, which are planned to be used in AEGIS as the target for cold positronium formation, have been recently developed as low-k interlayer insulators for use in future high-speed microelectronic devices. Voids are fabricated in these films in order to obtain a high degree of porosity and hence to make the dielectric constant lower. Important pore characteristics of the films, such as average size and size distributions are difficult to measure with standard techniques.

Positron Annihilation Lifetime Spectroscopy (PALS), is well known as an increasingly important tool that can be efficiently used to characterize the free-volume structure of thin films. The technique uses either positrons emitted from a radioactive isotope (so-called classic PALS) or positrons delivered by an intense pulsed positron beam with a variable energy typically in the range 1 - 50 keV. Beam based PALS techniques have recently been reported as holding great promise for probing pore sizes in the range between 0.3 nm to 100 nm for porous films with a thickness inferior to 0.1μm.

In classic PALS set-ups, the timing start signal t_0 is provided by a $\gamma-$ray that is released coincidentally from a radioactive source (typically ^{22}Na) with the positron. The stop signal is provided by one of the annihilation γ-rays. The *advantages* of this type of PALS technique are a high counting rate and a relatively simple experimental apparatus. The *disadvantage* is that the positrons are implanted relatively deeply and in an uncontrolled fashion, so that only *average* properties of a sample can be studied with such a technique. Thus, this scheme is well suited for the investigation of bulk materials, but not for thin-film samples.

In contrast, the *major advantage* of the PALS beam technique is the ability to control positron implantation into the sample. The sample can be depth-profiled by varying the incident beam energy. The timing start signal is provided either by the pulsing system of the positron beam, or by secondary

electrons produced when the positron beam strikes the sample surface. In the first case, the achieved high performance is balanced by high cost and system complexity. The later case is a relatively simple and low cost system. It is based on the use of an appropriate detector (e.g. microchannel plate) to detect secondary electrons and to generate the start signal t_0. The stop signal is again provided by one of the annihilation γ-rays. Both techniques are relatively new, and hold great promise, particularly in the study of void formation in thin films. These techniques have been used to determine the free-volume hole size distribution in various thin-film materials (e.g. polymers, porous SiO_2, ..) as a function of growing conditions, temperature, pressure, etc....

It is well known that in PALS studies of thin films, information on a sample structure is extracted from the results of the lifetime measurement of triplet Ps (orthopositronium, o-Ps) formed inside the sample. The vacuum value of the $o-Ps$ lifetime is shortened by collisional pick-off annihilation and ranges typically from a fraction of a ns to tens of ns. For high quality PALS spectra measurements the important characteristics of the positron bunch at the sample are: i) the bunch width, typically < 1 ns, ii) peak to background ratio, typically $\geq 10^2$; this is an important factor for accurate measurements of low-intensity $o-Ps$ components, and iii) shape of the time profile (resolution function), typically one or two Gaussians with small tails. This is important for measurements of short $o-Ps$ lifetimes.

The AEGIS setup is designed in such a fashion that all the above PALS techniques can be used for studying porous films, as a part of the optimization of the positronium production target, and thus provides a unique tool for the characterization and metrology of samples provided e.g. by the microelectronic industry.

Bibliography

[1] http://athena.web.cern.ch/athena/

[2] http://hussle.harvard.edu/ atrap/

[3] http://alpha.web.cern.ch/alpha/

[4] E. Fischbach, C. L. Talmadge "The search for non Newtonian Gravity" Springer (1999)

[5] J. Scherk, Phys. Lett. **88** B, 265 (1979)

[6] T. Goldman et al.,, Phys. Lett. B **171**, 217 (1986)

[7] M. Nieto and T. Goldman, Phys. Rep. **205**, 5 221-281,(1992)

[8] J. Barrow and R. Scherrer, Phys. Rev. D **70**, 103515 (2004)

[9] C. Alvarez and R. Mann, Phys. Rev. D **55**, 1732 (1997)

[10] J. D. Bekenstein, Phys. Rev. D **70** 083509 (2004); erratum Phys. Rev. D**71** 069901 (2005)

[11] J. W. Moffat, JCAP 0603 (2006) 004, gr-qc/0506021.

[12] D. Mota and D. Shaw, Phys. Rev. D **75**, 063501 (2007)

[13] P. Candelas and D. Sciama, Phys. Rev. D **27**, 1715 (1983)

[14] J. Ellis et al., Phys. Rev. D **53**, 3846 (1996)

[15] T. Ericson and A. Richter, Europhys. Lett. **11**, (4) 295 (1990)

[16] E. Adelberger et al.,B. Phys. Rev. Lett. **66**, 7 (1990) 850

[17] S. Bellucci and V. Faraoni, Phys. Rev. D **49**, 2922 (1994)

[18] F. Witteborn and W. Fairbank, Phys. Rev. Lett. **19** 1049 (1967)

[19] PS200 Proposal Los Alamos Report LA-UR 86-260

[20] T. Darling et al., Rev. Mod. Phys. **64** 9 237 (1992)

[21] A. Apostoloakis et al., Phys. Lett. B 452 (1999) 425

[22] L. I. Schiff Phys. Rev. Lett. **1** 254 (1958)

[23] M. Charlton et al Phys. Rep **241**, 65 (1994)

[24] R. Hughes Hyp. Int. **76**, 3 (1996)

[25] G. Gabrielse et al., Phys. Rev. Lett. **82**, 3198 1999.

[26] F. Huber et al., Class. Quantum Grav. **18**, 2457 (2001)

[27] K. Kirch, Phys. Lett. B (2007) (in press); Arxiv preprint physics/0702143, 2007

[28] T. Haensch and J. Walz, General Realtivity and Gravitation, **36** 561 (2004)

[29] A. Voronin and P. Froelich, J. Phys. B: At. Mol. Opt. Phys. **38** 9, 301 (2005)

[30] P. Perez and A. Rosowsky, NIM A **545**, 20 (2005)

[31] G. Luders, Ann. Phys. (NY) **2**, (1957) 1

[32] R. S. Van Dyck et al., Phys. Rev. Lett. **59**, 26 1987

[33] http://pdg.lbl.gov

[34] M. Niering et al., Phys. Rev. Lett. **84**, 5496 (2000)

[35] http://www.physics.indiana.edu/ kostelec/ and reference therein

[36] A. Peters et al., Metrologia **38**, 25 (2001)

[37] January-2005 CERN-SPSC 2005-002 SPSC P-307 Add.1 ASACUSA collaboration

[38] D. W. Keith et al., Phys. Rev. Lett. **61**, 1580 (1988)

[39] P. E. Moskowitz et al., Phys. Rev. Lett. **51**, 370 (1983)

[40] C. J. Bordé, Atom interferometry, edited by P. R. Berman, (Academic Press, 1997) p. 257

[41] R. Colella et al., Phys. Rev. Lett. **34**, 1472 (1975)

[42] J. Anandan, Phys. Rev. D **15**, 1448 (1977)

[43] D. M. Greenberger and A. W. Overhauser, Rev. Mod. Phys. **51**, 43 (1979)

[44] J. F. Clauser, Physica B **151**, 262 (1988)

[45] J. M. McGuirk et al., Optics Letters **26**, 364 (2001)

[46] J. Schmiedmayer, et al., in Atom interferometry edited by P. R. Berman (Academic Press 1997), p 1

[47] M. Kasevich and S. Chu, Phys. Rev. Lett. **67**, 181 (1991)

[48] M. Kasevich and S. Chu, Appl. Phys. B **54**, 321 (1992)

[49] A. Peters et al., Nature **400**, 849 (1999)

[50] T. Heupel et al., Europhys. Lett. **57**, 158 (2002)

[51] M. J. Snadden et al., Phys. Rev. Lett. **81**, 971 (1998)

[52] J. M. McGuirk et al., Phys. Rev. A **65**, 033608 (2002)

[53] A. Bertoldi et al., Eur. Phys. J. D **40**, 271 (2006)

[54] J. B. Fixler et al., Science **315**, 74 (2007)

[55] S. B. Cahn et al., Phys. Rev. Lett. **79**, 784 (1997)

[56] S. Fray et al., Phys. Rev. Lett. **93**, 240404 (2004)

[57] G. Roati et al., Phys. Rev. Lett. **92**, 230402 (2004)

[58] P. Cladé et al., Europhys. Lett. **71**, 730 (2005)

[59] G. Ferrari et al.,Phys. Rev. Lett. **97**, 060402 (2006)

[60] W. Schöllkopf et al., Eur. Phys. J. D **28**, 125 (2004)

[61] C. R. Ekstrom et al., Appl. Phys. B **54**, 369 (1992)

[62] T. A. Savas et al., J. Vac. Sci. Technol. B **13**, 2732 (1995)

[63] C. Champenois et al., Eur. Phys. J. D **13**, 271 (2001)

[64] M. K. Oberthaler et al., Phys. Rev. A **54** 3165 (1996)

[65] http://indico.cern.ch/conferenceDisplay.py?confId=a043551#12

[66] J. D. Perreault and A. D. Cronin, Phys. Rev. Lett. **95**, 133201 (2005)

[67] R. E. Grisenti et al., Phys. Rev. Lett. **83**, 1755 (1999)

[68] J. F. Clauser and Shifang Li, Atom interferometry edited by P. R. Berman (Academic Press) p 121 (1997)

[69] B. Dubetsky and P. R. Berman, Atom interferometry edited by P. R. Berman (Academic Press), p 407 (1997)

[70] G.V. Shlyapnikov et al., Hyper. Interactions **76** 31 (1993)

[71] J. Mitroy and G. Ryzhikh J.Phys. B: At. Mol. Opt. Phys. **30** L371 (1997)

[72] J.Lu. Doctor Degree Bielefeld Univ. - May 2003

[73] J. Lu et al., Phys. Rev. A 68, 024702 2003

[74] M. L. Wall et al., Phys. Rev. A **72**, 052702 (2005)

[75] R. Abrines C. Percival, Proc. Phys. Soc. 1966 vol 88 - 861

[76] R.E.Olson *Classical Trajectory and Monte Carlo Techniques* Atomic, Molecular Optical Physics Handbook 56 Drake, AIP Press (1996)

[77] E.A.Hessel et al., Phys Rev A **57**, (1998)

[78] T.F. Gallagher, Rep. Prog. Phys **51**, 143 (1988)

[79] T. F. Gallagher, '*Rydberg Atoms*', Cambridge University Press (1994)

[80] F. Merkt and A. Osterwalder, Int. Rev. Phys. Chem. **21**, 385 (2002)

[81] A. Osterwalder and F Merkt, Phys. Rev. Lett. **82**, 1831 (1999)

[82] S. R. Procter et al., Chem. Phys. Lett. **374**, 667 (2003)

[83] E. Vliegen and F. Merkt, J. Phys. B: At. Mol. Opt. Phys. **38**, 1623 (2005)

[84] E. Vliegen and F. Merkt, J. Phys. B: At. Mol. Opt. Phys. **39**, L241 (2006)

[85] E. Vliegen et al., Eur. Phys. J. D **40**, 73 (2006)

[86] E. Vliegen and F. Merkt, Phys. Rev. Lett. **97**, 033002 (2006)

[87] E. Vliegen et al., 'Stark deceleration and trapping of hydrogen Rydberg atoms', *submitted for publication*

[88] T. P. Softley, Int. Rev. Phys. Chem. **23** 1 (2004)

[89] J. Main et al., Phys. Rev. A **57**, 1149 (1998)

[90] F. Merkt, S. Hogan private communications

[91] C.H. Storry et al., Phys. Rev. Lett. 93, 263401 (2004).

[92] O. Halpern, Phys. Rev. 94,904 (1954)

[93] A.P. Mills Jr, Solid State Commun. **31**, 623 (1979)

[94] A.P. Mills Jr, Phys. Rev. Lett., **41**, 1828 (1978)

[95] K.G. Lynn and D.O.Welch, Phys. Rev. B, **22**, 99 (1980)

[96] Nagashima et al., Phys. Rev. B **52**, 258 (1995)

[97] A.P. Mills Jr et al., Phys. Rev. B **40**, 2045 (1989)

[98] Howell et al., Phys. Rev. B **35**, 5303 (1987)

[99] D.W. Gidley et al., Annu. Rev. Mater. Res. **36**, 49 (2006).

[100] Y.C. Jean, Material Sci. Forum **175-178** (1995) 59;
Positron Spectroscopy of Solids, edited by A. Dupasquier and A.P. Mills Jr (IOS, Amsterdam, 1995) p.503.

[101] D. W. Gidley et al., Phys. Rev. **B 60**, R5157 (1999).

[102] P. Schultz and K. G. Lynn, Rev. Mod. Phys. **60**, 701 (1988).

[103] A. Rich, Rev. Mod. Phys. **53**, 127 (1981).

[104] R.S. Vallery et al., Phys. Rev. Lett. **90** 203402 (2003).

[105] H. K. M. Tanaka et al., Phys. Rev. B **72**, 193408 (2005)
J. Phys. Condens. Matt. **18**, 8581 (2006)

[106] R.S. Yu et al., Appl. Phys. Lett. **83**, 4966 (2003)

[107] C. G. Fischer et al., Phys. Rev. **B 71**, 180102 (2005)

[108] http : //neutrino.ethz.ch/Positron/documentation/Thesis$_c$rivelli.pdf
P. Crivelli, phd thesis ETH, Zurich (2006)

[109] S.N. Gninenko "Detector for PALS measurements of porous and polymer films with the continuous magnetically guided slow positron beam.". Report to Project Avenir, May 10, 2004. Preprint LAPP-Exp-2004.07.

[110] N. Alberola et al., Nucl. Instr. Meth. **A 560**, 224 (2006).

[111] S. Gninenko private communications

[112] A. Dupasquier private communications

[113] R. Brusa, private coomunications

[114] S. Haidar et al., Appl. Opt. **41** (2002) 5656.

[115] R. W. Boyd, "Nonlinear Optics", Academic Press (1992)

[116] B. W. Shore, "The theory of coherent atomic excitation", John Wiley & Sons (1990)

[117] http://www.firstpsi.com/

[118] D.B. Cassidy et al. Rev. Sci. Instrum. **77**, 073106 (2006)

[119] R.C. Davidson "Physics of non neutral plasma" Addison-Wesley Publishing Company, Redwood City 1990

[120] D.B. Cassidy et al.,Phys. Rev. Lett. **95** 195006 (2005)

[121] M.H. Douglas and T.M. O'Neil, Phys. Fluids **22**, 266 (1979)

[122] S.E.Peil (phd Thesis), Harvard University, 1999
http : //hussle.harvard.edu/ gabrielse/gabrielse/papers/1999/1999$_{\mathrm{p}}$eil.pdf

[123] T.'ONeil, Phys. Fluids **24**, 1447 (1981)
M. Amoretti et al, Phys. Plasmas **13**, 012308 (2006)

[124] T.M. O'Neil, Physics Scripta **T59**, 341 (1995)

[125] B. Odom et al., Phys. Rev. Lett. 97 030801 (2006)

[126] N. Madsen et al, Phys. Rev. Lett. **94**, 033403 (2005)

[127] M. Amoretti et al, Phys. Lett. B **578**, 23 (2004)

[128] M. Amoretti et al, Phys. Lett. A **360**, 141 (2006)

[129] C. F. Driscoll "Low energy antimatter" (David Cline ed.) Singapore: World Scientific **184**, 15 (1986)

[130] L. Spitzer, *Physics of fully ionized gases* (Interscience Publisher, New York, 1962).

[131] A. Kellerbauer and J. Walz, New J. Phys. **8**, 45 (2006).

[132] T. Andersen, Phys. Reports **394**, 157 (2004).

[133] R. C. Bilodeau and H. K. Haugen, Phys. Rev. Lett. **85**, 534 (2000).

[134] R. Middleton, Nucl. Instrum. Methods **214**, 139 (1983).

[135] R. Middleton, `http://tvdg10.phy.bnl.gov/cookbook` (unpublished, 1989).

[136] A. Crubellier, J. Phys. B: At. Mol. Opt. Phys. **23**, 3585 (1990).

[137] T. W. Hänsch and A. L. Schawlow, Opt. Commun. **13**, 68 (1975).

[138] A. Miffre et al., European Journal of Physics, **23**, 623 (2002)

[139] A. Miffre et al., Eur. Phys. J. D **33**, 99 (2005)

[140] C. M. Surko et al., in *Non-Neutral Plasma Physics III*, edited by J. J. Bollinger, R. L. Spencer and R. C. Davidson, AIP Conf. Pro. **498**, 3 (1999)

[141] T. J. Murphy and C. M. Surko, Phys. Rev. **A 46**, 5696 (1992)

[142] R. G. Greaves et al., Phys. Plasmas **1**, 1439 (1994)

[143] X. Huang et al., Phys. Rev. Lett. **78**, 875 (1997)

[144] C.F. Driscoll and J.H. Malmberg, Phys. Rev. Lett **50**, 167 (1983)

[145] E.M. Hollmann et al., Phys. Plasma **7**, 2776 (2000)

[146] A.P. Mills Jr and E.M. Gullikson, Appl. Phys. Lett. **49**, 1121 (1986)

[147] R. Khatri et al., Appl. Phys. Lett. **57**, 2374 (1990)

[148] J.P. Merrison et al., J. Phys. Condens. Matter **4**, L207 (1992)

[149] R. G. Greaves and C. M. Surko, Phys. Rev. Lett. **85**, 1883 (2000)

[150] M. Charlton and J.W. Humberston, Positron Physics, Cambridge University Press, chapter 6 (2000)

[151] L. Turner, Phys. Fluids. **30**, 3196 (1987)

[152] D. H. E. Dubin, Phys. Rev. Lett. **66**, 2076 (1991)

[153] M. D. Tinkle et al., Phys. Rev. Lett. **72**, 352 (1994)

[154] D. H. E. Dubin, Phys. Fluids B **5**, 295 (1993)

[155] M. Amoretti *et al.*, Phys. Rev. Lett. **91**, 055001 (2003)

[156] M. Amoretti *et al.*, Phys. Plasmas **10**, 3056 (2003)

[157] L. S. Brown et al., Rev. Mod. Phys. **58**, 233 (1986)

[158] G. Savard et al., Phys. Lett. A **158** 247 (1991)

[159] Kellerbauer et al., Phys. Rev. A **73**, 062508 (2006)

[160] H. Higaki et al., Phys. Rev. E **70**, 026501 (2004)

[161] P. Riedler et al., Nucl. Instr. and Meth. A **478**, 316 (2002)

[162] M. Fujiwara and M. Marchesotti, Nucl. Instr. and Meth. A **484**, 162 (2002)

[163] R. Medenwaldt et al., Nucl. Instr. and Meth. B **58**, 1 (1991)

[164] M. Amoretti et al., Nucl. Instr. and Meth. A **518**, 679 (2004)

[165] M.C Fujiwara et al., Phys. Rev. Lett. **92**, 065005 (2004)

[166] C. Amsler et al., Nucl. Instr. and Meth. A **480**, 494 (2002)

[167] C. Regenfus, Nucl. Instr. and Meth. A **501**, 65 (2003)

[168] O. Toker et al., Nucl. Instr. and Meth. A **340**, 572 (1994)

[169] P.L. McGaughey et al., Nucl. Instr. and Meth, A **249**, 361 (1986)

[170] R. Brenner et al., Nucl. Instr. and Meth. A **326**, 189 (1993)

[171] J. Straver et al., Nucl. Instr. and Meth. A **348**, 485 (1994)

[172] P. Morettini et al., Nucl. Instr. and Meth. A **395**, 372 (1997)

[173] C. Amsler et al., Nucl. Instr. and Meth. A **480**, 501 (2002)

[174] S. Straulino et al., Nucl. Instr. and Meth. A **556**, 100 (2006)

[175] R. Lauhakangas et al., Nucl. Instr. and Meth. A **364**, 74 (1995)

[176] E. Belau et al., Nucl. Instr. and Meth. **214**,253 (1983)

[177] X. Feng et al., J. Appl. Phys. **79**, 1 (1996)

[178] G. B. McMillian et al., J. Phys. B: At. Mol. Opt. Phys. **15**, (1982) 2131

[179] W. Pauli, Z. Phys. **36**, (1926) 336

[180] D.B. Cassidy et al., Phys. Rev. Lett. **95**, 195006 (2005)

[181] H. Marxer et al., Phys Rev A **43** 1268 (1991)

[182] M. H. Horbatsch et al., Journal of Physics B **38**, 1765 (2005)

[183] M. H. Horbatsch Phys. Rev. A **72**, 3 (2005)

[184] T. Pohl et al., Phys. Rev. Lett. **21**, 213001 (2006)

[185] M. R. Flannery et al., Phys. Rev. A **68**, 030502 (2003)

[186] C. L. Taylor et al., Journal of Physics B **39**, 4945 (2006)

[187] N. Vanhaecke et al., Journal of Physics B **38**, 409 (2005)

[188] S. K. Dutta et al., Phys. Rev. Lett. **86** 3993 (2001)

[189] J. W. Farley et al., Phys. Rev. A **23** 2397 (1981)

[190] D. Comparat, private communications

[191] K.S. Eikema et al., Phys. Rev. Lett. **86**, 5679 (2001)

[192] J. Walz et al., Journal of Physics B **36**, 649 (2003)

[193] D. Kielpinski, Phys. Rev. A **73**, 063407 (2006)

[194] V. Zehnle' et al., Phys.Rev. A **63**, 021402 (2001)

[195] P.O. Schmidt et al., Journal of the Optical Society of America B **20**, 960 (2003)

[196] M. Allegrini et al., Physics Letters A **172**, 271 (1993)

[197] M. Oberst et al., Optics Communications **264**, 463 (2006)

[198] Louis Cabaret, to be published

[199] L. Cabaret et al., IEEE J. of Quantum Electronics **36**, 323 (2000)

[200] J. Walz et al., Hyperfine Interactions **127**, 167 (2004)

[201] N. Kolachevsky et al.,Phys. Rev. A **73**, 021801R (2006)

[202] M. Notcutt et al.,Optics Lett. **30**, 1815 (2005)

[203] D. Comparat et al., Phys. Rev. A **73**, 0434102006

[204] J. Fajans et al., Phys. Rev. Lett. **95**, 155001 (2005)

[205] G. Gabrielse et al., Phys. Rev. Lett. , 98 113002 (2007)

[206] CERN Council, The European Strategy for Particle Physics, p.36 (2006)

[207] G. S. Adkins, R. N. Fell, J. Sapirstein, Ann. Phys. (N.Y.) **295**,136 (2002)

[208] D. Schwalm et al., Nucl. Instr. and Meth. B **221**, 185 (2004) F. Fleischer et al., Can. J. Phys. 83(4) (2005) 413.

[209] P. A. Vetter, Int. J. Mod. Phys. A **19**, 3865 (2004)
Mod. Phys. Lett. A **19**, 871 (2004)

[210] A.P. Mills Jr, Nucl. Instr. and Meth. B **192**, 107 (2002)

[211] Positronium physics. Proceedings, 1st International Workshop, Zuerich, Switzerland, May 30-31, 2003. M. Felcini, (ed.), S.N. Gninenko, (ed.), A. Nyffeler, (ed.), A. Rubbia, (ed.) (Zurich, ETH & Moscow, INR) . 2004. 217pp. Published in Int. J. Mod. Phys. A19 (2004) 3769-3985

[212] S.N. Gninenko et al., Phys. Rev. D **67**, 075012 (2003) hep-ph/0302205
Mod. Phys. Lett. A **17**, 1713 (2002)
A. Rubbia, Int. J. Mod. Phys. A **19**, 3961 (2004) hep-ph/0402151
S.N. Gninenko et al., Phys. Part. and Nucl. **37**, 321 (2006)

[213] S.G. Karshenboim, Phys. Rept. **422**, 1 (2005) hep-ph/0509010

[214] V.V. Dvoeglazov et al., Mod. Phys. Lett. **A8**, 3263 (1993).

[215] A.P. Mills Jr., M. Leventhal, Nucl. Instr. and Meth. B **192**, 102 (2002)

[216] S. Asai et al., Phys. Lett. B **357**, 475 (1995)
S. Asai et al., hep-ex/0308030

[217] R.S. Vallery et al., Phys. Rev. Lett. **90**, 203402 (2003)

[218] A.P. Mills Jr and G.H. Bearman, Phys. Rev. Lett. **34**, 246 (1975)
A. P. Mills Jr, Phys. Rev. A **27**, 262 (1983)

[219] M.W. Ritter et al., Phys. Rev. A **30**, 1331 (1984)

[220] U. Amaldi et al., Phys. Lett. B **153**, 444 (1985)

[221] J. Yang et al., Phys. Rev. A **54**, 1952 (1996)

[222] D.W. Gidley et al., Phys. Rev. Lett. **66**, 1302 (1991)

[223] S. Asai et al., Phys. Rev. Lett. **66**, 1298 (1991)

[224] S. Asai et al., Phys. Rev. Lett. **66**, 2240 (1991)

[225] S. Asai et al., Phys. Lett. B **323**, 90 (1994)

[226] M.V. Akopyan et al., Phys. Lett. B **272**, 443 (1991)

[227] S. N. Gninenko et al., Phys. Lett. B **237**, 287 (1990)

[228] A. Badertscher et al., Phys. Lett. B **452**, 29 (2002)
P. Crivelli, Can. J. Phys. **80**, 1281 (2002)

[229] S.N. Gninenko et al., Phys. Rev. D **67**, 075012 (2003)

[230] R. Foot and S.N. Gninenko, Phys. Lett. B **480**, 171 (2000) R. Barbieri et al., Preprint CERN-PH-TH-2005-162, Sep 2005. 15pp., hep-ph/0509242;
Z. Chacko et al., hep-ph/0506256;
Z. Berezhiani and L. Bento, Phys. Lett. B **635**, 253 (2006) hep-ph/0602227
Z. Berezhiani and L. Bento, Phys. Rev. Lett. **96**, 081801 (2006) hep-ph/0005238
A.Yu. Ignatiev and R.R. Volkas, Phys. Lett. B **487**, 294 (2000) hep-ph/0005238.

[231] H. Gies et al., Phys. Rev. Lett. **97**, 140402 (2006) hep-ph/0607118
S.A. Abel et al., hep-ph/0608248

[232] P.A. Vetter and S.J. Freedman, Phys. Rev. A **66**, 052505 (2002)

[233] G.S. Atojan et al., Phys. Lett. B **220**, 317 (1989)

[234] T. Mitsui et al., Phys. Rev. Lett. **70**, 2265 (1993)

[235] A. Badertscher et al., Phys. Rev. D **75**, 032004 (2007)

[236] R. Foot, Phys. Rev. D **69** 036001, (2004) hep-ph/0308254.

[237] R. Bernabei et al. (DAMA Collaboration), Riv. Nuovo Cimento. **26**, 1 (2003) astro-ph/0307403, and references there-in.

[238] S.L. Glashow, Phys. Lett. B **167**, 35 (1986)

[239] S.N. Gninenko, Phys. Lett. B **326**, 317 (1994)

[240] R. Foot and S.N. Gninenko, Phys. Lett. B **480**, 171 (2000)

[241] E. D. Carlson and S.L. Glashow, Phys. Lett. B **193**, 168 (1987)

[242] N.V. Krasnikov, Int. J. Mod. Phys. A **19**, 3849 (2004) Proceedings of the Workshop on Positronium Physics, ETH Zürich, Switzerland, 30-31 May 2003.

[243] P.A. Vetter, Mod. Phys. Lett. A **19**, 871 (2004)

[244] L.B. Okun, hep-ph/0210052

[245] W. Bernreuther and O. Nachttmann, Z. Phys. C **11**, 235 (1981)

[246] B.K. Arbic et al., Phys. Rev. A **37**, 3189 (1988)

[247] M. Scalsey and J. Van House, Phys. Rev. Lett. **67**, 1993 (1991)

[248] M. Felcini, Int. J. Mod. Phys. A **19**, 3853 (2004) Proceedings of the Workshop on Positronium Physics, ETH Zürich, Switzerland, 30-31 May 2003 hep-ex/0404041.